PROTON AND NEUTRON CONTRIBUTIONS FOR CROSS-SHELL EXCITATIONS NEAR DOUBLY MAGIC ^{40}CA STUDIED BY LIFETIME MEASUREMENTS OF MIRROR TRANSITIONS

By

Andrew Sanchez

A DISSERTATION

Submitted to
Michigan State University
in partial fulfillment of the requirements
for the degree of

Physics—Doctor of Philosophy

2024

ABSTRACT

Under the assumption of isospin conservation in the strong interaction, mirror nuclei should have similar level schemes and excitation properties; however, when deviations from expected trends are observed in transition strengths of mirror nuclei, the opportunity may arise to learn about physics mechanisms to account for the isospin symmetry breaking phenomena. It is known that the isospin non-conserving force and Coulomb force can induce mirror energy differences. Nuclear shape changes among mirror nuclei may also change the balance of the transition strengths among mirror partners. The reduced transition strength B(E2) is proportional to the square of the proton matrix element M_p and, therefore, measurements of the transition strength provide valuable data for comparison to shell-model calculations which utilize various effective interactions. Because the proton matrix element M_p for a transition in one nucleus is equivalent to the neutron matrix element M_n for the same transition in the mirror nucleus, measurements of mirror transitions provide a fuller picture of neutron and proton configurations for excited states, especially since the neutron matrix element is difficult to measure directly. Further, when measurements of mirror transitions are conducted within the same experiment, and the data are analyzed with the same methods, the resulting values of M_n and M_p may be compared more effectively due to reduction of systematic uncertainty associated with comparing results from different experiments or by different analysis methods.

In this work, we have utilized the recoil-distance method (RDM) to measure the lifetimes of the $11/2^-$ states in mirror nuclei ^{39}Ca and ^{39}K by examining the analog $11/2^- \rightarrow 7/2^-$ transitions in both nuclei. The RDM lifetime measurements provide a model independent method of determining the B(E2) and, hence, the matrix elements M_p and M_n for the analog transitions. The measurements were performed utilizing the Coupled-Cyclotron Facility and A1900 fragment separator to produce a ^{42}Sc secondary beam which was directed to the TRIPLEX device where reactions on a ^{9}Be target produced ^{39}Ca and ^{39}K in excited states. The excited nuclei were identified in the S800 spectrograph and gamma rays were collected with the GRETINA array. The analysis methods employed for the lifetime measurement of the $11/2^-$ state in ^{39}Ca were validated by comparing the ^{39}K results to

adopted values. Additionally, the data provide an improved lifetime measurement of the $9/2^-$ state in ^{39}Ca.

From the lifetime measurements, the reduced transition strengths B(E2) are determined for the $11/2^- \rightarrow 7/2^-$ mirror transitions. Using the matrix element decomposition, the M_p and M_n are determined and the results are compared to shell-model calculations which utilize three effective interactions common to this region of the nuclear chart. The comparison of the matrix elements to shell-model calculations suggests an enhanced transition strength in ^{39}Ca, suggesting both proton and neutron contributions to core excitations across the $Z = N = 20$ shell gaps.

ACKNOWLEDGEMENTS

Its been a long strange trip to get to this point and its required the support of many people, so where do I start? Of course, at the beginning. Without my mother, Kathryn Gontarz, none of this would have been possible and I must begin with acknowledgment of her unwavering support throughout my life (good times, bad times, you know I've had my share).

I absolutely must thank Prof. Alan Wuosmaa from University of Connecticut for noticing the potential in me and supporting each of my goals through undergrad and into grad school. Profs. Artemis Spyrou and Jaideep Singh for providing the summer research opportunities that sparked my interest in experimental nuclear physics. Of course my advisor and committee chair, Prof. Hiro Iwasaki, who knew just how much to push me to attain my goals. I'd also like to thank my other committee members Profs. Sean Liddick, Dean Lee, Stuart Tessmer, and Katharina Domnanich. I must also thank MSU for gambling on me and giving me the opportunity to be a part of this wonderful program.

There are a few more people that deserve extra acknowledgments for providing academic and personal support above and beyond my expectations. First I must acknowledge my officemate Peter Farris, who always found time to work through a problem with me and who I have had the pleasure to watch grow into a great person and scientist. Roy Salinas, my other officemate, who has been instrumental in my analysis by always taking time to work through issues in my code and being a wonderful, generous person with a great sense of humor. I also must thank Cavan Maher for being a good friend and for his emotional support through tough times.

Finally, my girlfriend Danielle Kohl. As the demands on my time became larger and larger, Danielle was always there to take care of the things that needed to be done but that I just couldn't find the time or energy to do. She has been my biggest cheerleader throughout my final and most demanding years in this program. I'm so thankful that, by chance, our vessels passed, and we finally met at last.

TABLE OF CONTENTS

LIST OF TABLES

LIST OF FIGURES

CHAPTER 1

INTRODUCTION

The field of nuclear structure studies endeavors to explain how the nucleons within an atomic nucleus arrange themselves under different conditions and how these configurations are expressed in various measurable quantities such as reaction cross sections, transition strengths, and state lifetimes. The nucleus offers a rich environment for physics research as it lies at the intersection of three of the four fundamental forces: the strong nuclear force, the Coulomb force, the weak nuclear force, and the gravitational force, which is commonly ignored in this field due to its weak interaction at small mass scales relative to the other three forces. While the interactions of these forces provide many avenues for examination, even if one ignores the weak and gravitational interactions, determining how nucleons arrange themselves quickly becomes a complex problem even for some of the lightest nuclei.

In Fig. 1.1 , the problem of modeling the atomic nucleus is presented in terms of different scales and degrees of freedom. Quantum chromodynamics attempts to build nuclei from fundamental quark-gluon interactions [2], but the amount of computational power necessary to describe even a helium nucleus can be daunting due to the number of degrees of freedom involved [3]. Some ab-initio nuclear calculations such as Green's function Monte Carlo (GFMC) [4, 5, 6], no-core shell mode (NCSM) [7, 8, 9], variational Monte Carlo (VCM) [10], and coupled cluster (CC) [11, 12] attempt to simplify the problem by restricting the degrees of freedom to the properties of protons and neutrons; but even these simplified models of 2 and 3 body nucleon-nucleon interactions can challenge technical capabilities for calculations involving light nuclei of $A < 20$. Nuclear mean field models which utilize effective interactions, such as Hartree-Fock based calculations [13], can further reduce the degrees of freedom by modeling nuclei as a system of A nucleons which each move in an external field generated by the remaining $A - 1$ nucleons [14] . Effective field theories (EFTs) [15] utilize nucleon motion and density to reduce light systems down to manageable problems while collective models can be used to describe large mass systems in terms of vibrational and rotational modes, similar to the liquid-drop model.

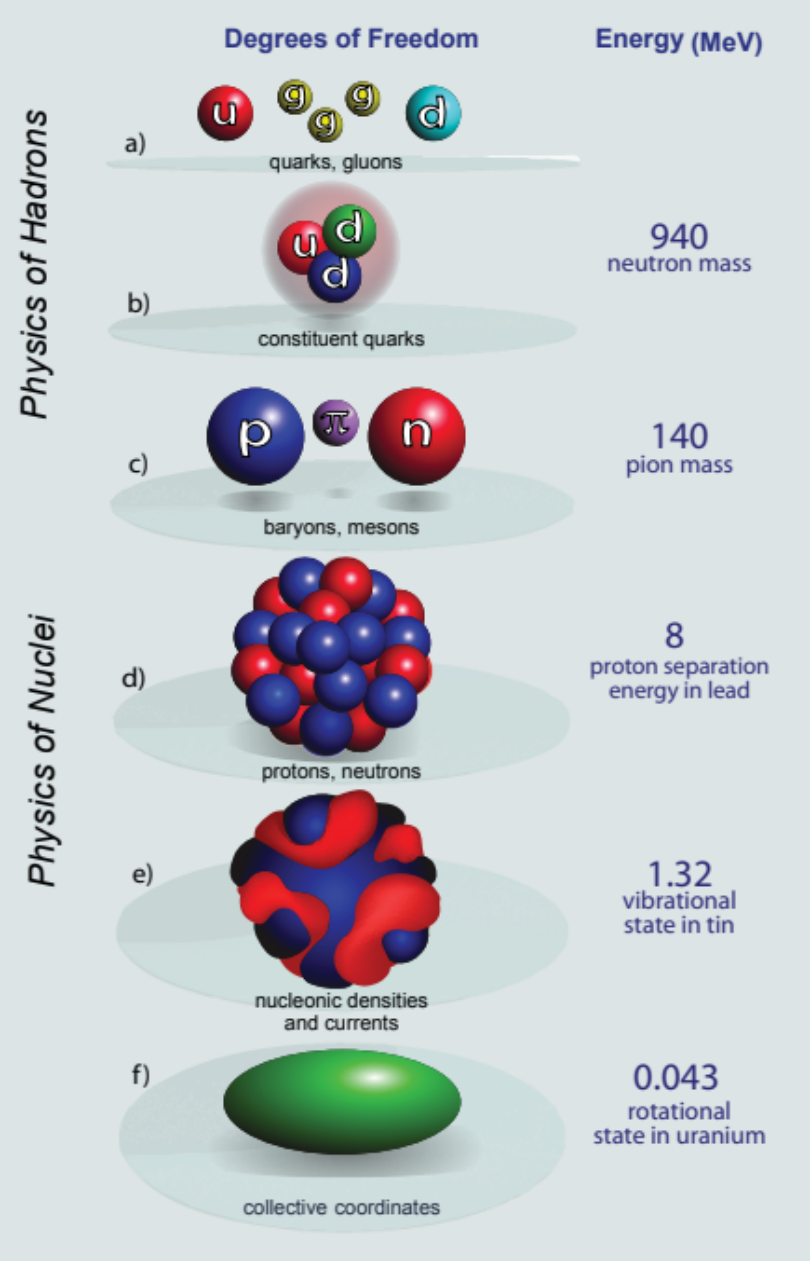

Figure 1.1 (a) At the highest energies and shortest scales, nucleons are built from quark-gluon interactions with many degrees of freedom at high computational costs. (b) By using an effective model of quarks, hadrons can be modeled with less degrees of freedom by integrating out the gluons. (c) A further reduction in degrees of freedom can be implemented by building nuclei from up from inter-nucleon interactions utilizing a potential or pion-exchange. (d) A nucleon in a mean-field potential allows for single-particle excitations up to the nucleon separation energy. (e) Effective fields reduce the many-body problem to critical building blocks such as proton and neutron densities and currents. (f) Collective models can be implemented for large A systems which are characterized by vibrational and rotational modes. The figure has been adopted from Ref. [1].

Many of the challenges in structure study are a result of the complexity of the strong interaction, which is strongly repulsive at nucleon separations of $r < 0.7$ fm, attractive at $r \approx 1$ fm, and diminishes rapidly as r approaches 2 fm [16]. When one includes the electromagnetic effects of protons, the dynamics of nucleon motion, and the effects of the angular momentum and intrinsic spin of each nucleon, simplified models become increasingly necessary to describe heavier nuclei.

The problem of nuclear structure can be simplified when the concept of isospin is introduced. In the isospin model, protons and neutrons are viewed as two states of the same particle, the nucleon, with different isospin projections [17]. The study of mirror energy differences (MEDs); that is, the difference in the energies of mirror states, is one common method of probing how well the isospin model holds in mirror nuclei. Of course, the isospin model is an approximation as it ignores the charge of the proton; but this approximation works remarkably well when one compares the spin assignments and energies of level diagrams for mirror nuclei, with MEDs typically on the order of $10 - 100$ keV [18]. Once isospin has been invoked, differences in mirror energy levels can then be attributed to isospin non-conserving forces such as the Coulomb interaction.

Transition strengths between states is another common method of investigating nuclear structure. When significant discrepancies are observed in the transition strengths of mirror nuclei, opportunities may arise to investigate the underlying mechanisms involved in isospin symmetry breaking [19, 20]. The measurements of reduced transition strengths B(E2) between the first 2^+ and 0^+ ground state has led to the observation of unexpected behaviors such as collectivity [21], shape coexistence [22, 23], intruder configurations [24], and shell evolution [25, 26] in exotic regions of the nuclear chart such as the neutron-rich island of inversion [27].

This work endeavors to exploit isospin symmetry and reduced transition strengths through the method of isospin decomposition and precision measurements to shed new light on cross-shell excitations, even in close proximity to doubly magic ^{40}Ca. From the reduced transition strengths of mirror transitions, we can determine the neutron and proton matrix elements of a transition and infer from the experimental data and theory calculations that significant contributions from both proton and neutron cross-shell excitations must be invoked to describe low-lying excited states near

stability. The aim of the following discussion is to provide the background required for a qualitative and quantitative understanding of the reduced transition strength B(E2) and the matrix elements $M_{p/n}$, which serve as benchmarks for the testing of modern effective-interaction models and their relevancy to modern nuclear structure studies.

1.1 Nuclear Structure

The mass of a nucleus can approximated as Au where $A = N + Z$ is the sum of neutrons N and protons Z and u is the atomic mass unit, defined as one-twelfth of the mass of a carbon-12 atom. If we neglect the relatively small amount of binding energy which contributes to the mass of the nucleus, it allows for the reasonable approximation that the proton and neutron have equal masses; indeed, the number A is commonly referred to as the "mass number" of a nucleus. Given these definitions, a common notation for describing a nucleus is ${}^{A}_{Z}\mathrm{X}_{N}$, where X is the chemical symbol of the element. A more concise and common notation, which we will employ in this work, is given as ${}^{A}\mathrm{X}$ since X implies the number of protons Z and the number of neutrons N can be deduced via $N = A - Z$. A nucleus of Z protons may form a bound state with many different numbers of neutrons N and to these nuclei we assign the title "isotopes"; relevant to this work are the calcium isotopes ^{38}Ca and ^{39}Ca which both have $Z = 20$ protons but contain $N = 18$ and $N = 19$ neutrons, respectively. Particularly relevant to this study are the subset of isobars (nuclei of the same mass number A) which we call "mirror nuclei", these are sets of nuclei whose proton and neutron numbers are exchanged such as ^{39}Ca with $Z = 20$ and $N = 19$, and ^{39}K with $Z = 19$ and $N = 20$.

Protons carry a charge of +1 and tend to strongly repel one another via Coulomb repulsion when protons are within a few femtometers of each other. Neutrons carry no charge but tend to bind the nucleus together via the strong force, which attracts nucleons on the same distance scale that the Coulomb force repels. Relevant to the following conversation is the concept of isospin symmetry [17], which proposes that neutrons and protons be considered two states of the same particle with different isospin projections T_z. Since both protons and neutrons have an intrinsic spin of $1/2$ and nearly equal masses, it is useful to model nucleons as an isospin doublet of isospin

$T = 1/2$ and projections $T_z = -1/2$ for protons and $T_z = +1/2$ for neutrons. When speaking of an entire nucleus with many bound nucleons, we consider the total isospin projection of the nucleus $T_z = (N - Z)/2$ with $2T + 1$ eigenvalues ranging from $T_z = -T$ up to $T_z = +T$ in integer steps. A consequence of conservation of isospin is that one expects mirror symmetry from mirror nuclei; that is, the energy level diagrams of mirror nuclei should appear very similar with differences attributed to isospin non-conserving forces such as the Coulomb force.

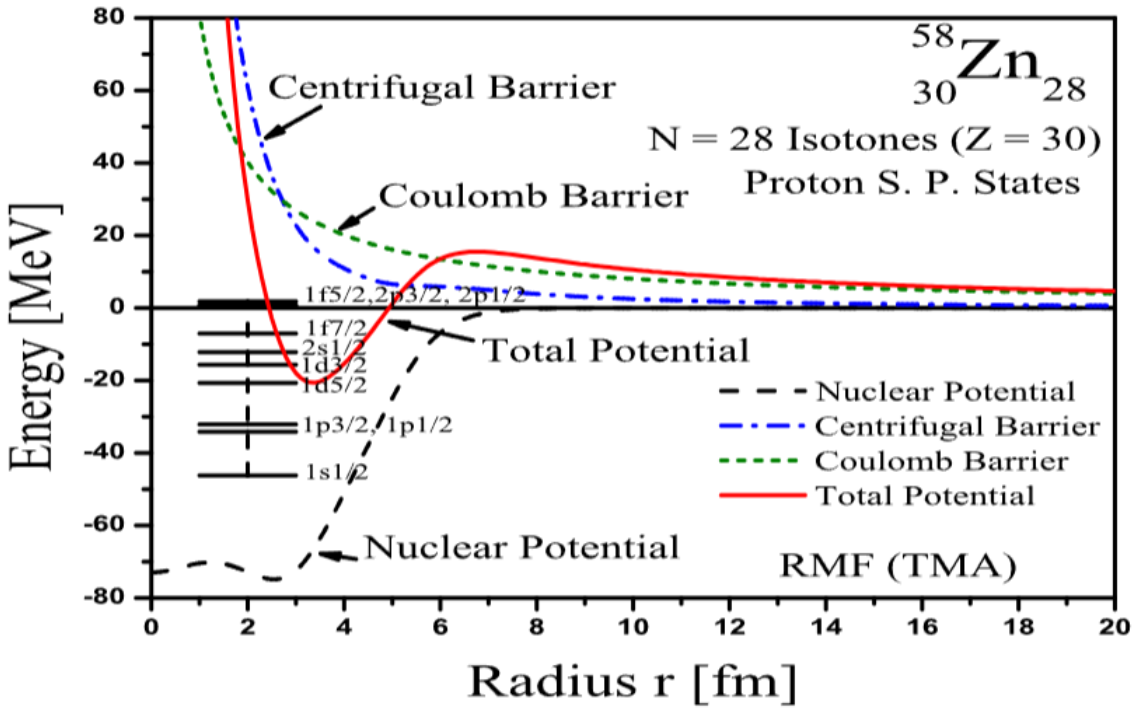

Figure 1.2 The potential energy for single particle proton states is presented as a function of radius r for the ^{58}Zn nucleus. The total potential (red) is displayed as the sum of the relativistic mean-field (RMF) nuclear potential (black dash), the Coulomb potential (green dash), and centrifugal potential (blue dash). Also displayed are the single particle proton states below 0 MeV and continuum states just above 0 MeV [28]. Used with permission of World Scientific Publishing Co., Inc., from ''Study of neutron magic drip-line nuclei within relativistic mean-field plus BCS approach", G. Saxena *et al.*, 22, 05 (2013); permission conveyed through Copyright Clearance Center, Inc.

Both protons and neutrons carry an angular momentum l which, when large, provides additional binding due to the centrifugal barrier. Fig. 1.2 provides a nuclear potential (in this case, for ^{58}Zn) in red which is the sum of the nuclear, Coulomb, and centrifugal components [28]. The figure displays the energy as a function of distance r and conveys the concepts of attraction and repulsion

at the nucleon scale via the various components that comprise the total potential. At distances less than approximately 2.5 fm, where the total potential is positive, protons repel each other primarily due to the Coulomb and centrifugal potentials. Between 2.5 and 5 fm, protons are bound within the negative potential well and will occupy single particle states such as the $1s_{1/2}$ through $1f_{7/2}$ states depicted in the negative energy region. One notes on Fig. 1.2, though the term "centrifugal barrier" is used to describe the blue dashed line, the same term is also used to describe the humped region of the total potential between 6 and 10 fm, though this hump arises from the sum of the Coulomb and centrifugal components and acts as a barrier in that a nucleon within the potential well requires a large kinetic energy to escape the well, and a nucleon outside the hump requires the same energy to penetrate the potential well from outside. Of course, the above explanation relies on a classical understanding of potential and kinetic energies, but an explanation more relevant to this work requires a quantum mechanical understanding.

Once the potential of a nuclear system is modeled, such as in Fig. 1.2, the Schrödinger equation $H\Psi = E\Psi$ can be solved for the energies E of the states of the system where H is the Hamiltonian which contains information about the nucleon momentum (linear and angular), spin, and various potential energy approximations, and Ψ is the wave function which contains information about the orbital occupations of the nucleons. Generally, the Hamiltonian will tend to be a sum $H = V_0 + V_1 + V_2 + ...$ of the various nuclear, and/or electromagnetic potentials V_n that comprise the total potential and is typically represented as a matrix with eigenvalue and eigenstate solutions calculated from the Schrödinger equation for various wave function combinations. When the Hamiltonian has been diagonalized with Ψ_n wavefunctions (with $n = 1, 2, 3, ...$ distinguishing various single-particle configurations), the diagonal matrix elements provide the level energies; therefore, level energies are important, providing experimentally-measured values to which effective interactions can be fit to and which model calculations are tested against.

In one of its simplest forms, a Hamiltonian can be modeled with a harmonic oscillator potential which, when solved for, provides single-particle state energies in multiples of $\hbar\omega$. Historically, the variations of the 3-dimensional harmonic oscillator model, whose solutions are functions of

the principle quantum number n and orbital angular momentum l, were the blocks upon which the modern nuclear shell model was built. Experimental data accumulated in the mid 20th century had shown that when nuclei contain certain numbers of neutrons or protons the binding energy of the nucleus is greatly increased and the nucleus appears to exist in a more stable configuration, these numbers would come to be described as "magic numbers" and found to be linked to the closed shell orbitals; that is, orbitals whose shells are maximally occupied by nucleons.

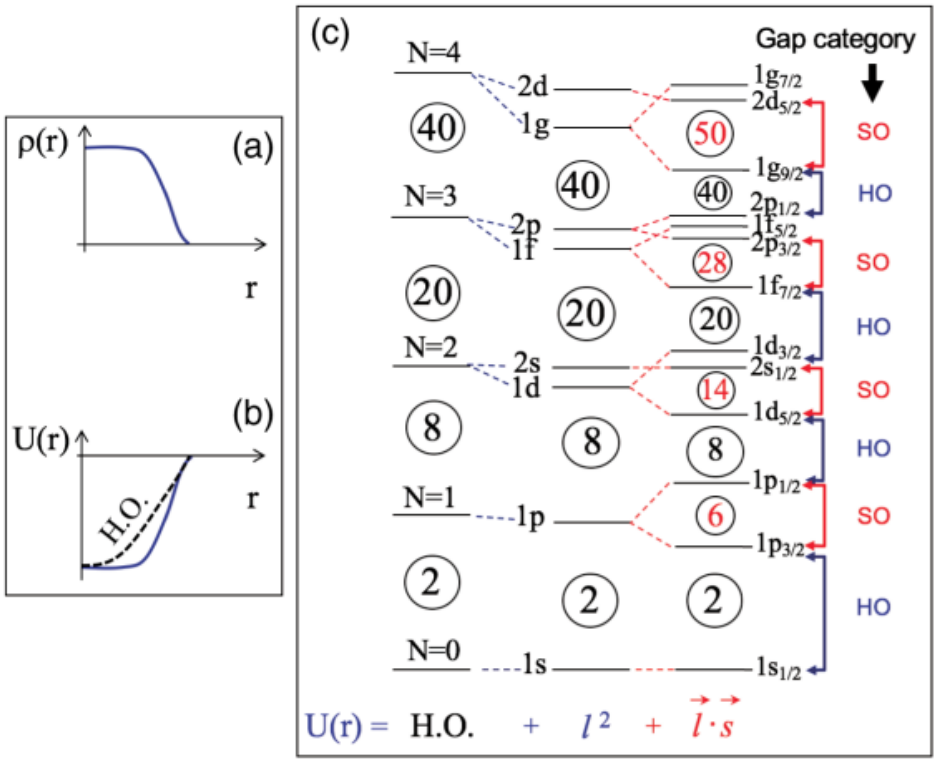

Figure 1.3 (a) The nuclear density $\rho(r)$ is understood to be relatively constant within the the interior of the nucleus as the nucleon-nucleon forces tend to average out, but decreases toward the nuclear skin. (b) The nuclear potential $U(r)$ is flat within the nuclear interior while tapering toward the nuclear skin. The harmonic oscillator potential "H.O." is used as a first order estimation for the nuclear potential. (c) The nuclear shell model single-particle energy solutions for various potentials. Harmonic oscillator solutions (left) could not explain the experimentally observed magic numbers above 20. The development of the Woods-Saxon potential (middle) split the degeneracy of the harmonic oscillator levels according to their orbital angular momentum l^2. The inclusion of the spin-orbit coupling term $\vec{l} \cdot \vec{s}$ (right) was necessary to replicate the observed magic numbers above 20 [26]. Reprinted figure with permission from T. Otsuka, A. Gade *et al.*, Rev. Mod. Phys., vol. 92, p. 015002 (2020). Copyright (2024) by the American Physical Society.

Figure 1.3 shows that the harmonic oscillator model was able to reproduce the first few magic

numbers: 2, 8, and 20; but it predicted numbers above 20 that were not supported by the experimental evidence. The development of the Woods-Saxon potential added a potential term that contained information about the nuclear radius, surface diffuseness, and the potential well depth, which broke the degeneracy of the harmonic oscillator solutions into levels of different l. A major breakthrough in nuclear structure was the addition of the spin-orbit coupling term to the Woods-Saxon potential, whose solutions are given on the right of Fig. 1.3. It was the work of Mayer and Jensen which demonstrated that the addition of a spin-orbit term to the nuclear potential could replicate the magic numbers above 20 [29, 30, 31]. By coupling the intrinsic spin s and orbital angular momentum l, the degeneracy of the $l > 0$ orbits is split into two levels of $j = l \pm \frac{1}{2}$. Today, energy states are defined by the principle quantum number n, the angular momentum $l = 0, 1, 2, 3, .. = s, p, d, f, ...$, and the total angular momentum $J = L + S$ such that every state in a shell structure can be described with the nl_J notation and the state parity given by $\pi = (-1)^l$. The introduction of spin-orbit coupling led to a shared Nobel prize in 1963 [32] and served as a guidepost for nuclear research for decades to follow.

Figure 1.4 depicts the currently observed and predicted nuclides with proton number on the vertical axis and neutron number on the horizontal axis. The nuclei with traditional magic numbers of closed shells are outlined with rectangular boxes and the intersections of vertical and horizontal boxes correspond to the doubly magic nuclei such as ^{16}O, ^{40,48}Ca, ^{48,78}Ni, etc... The chart has been colored accordingly with the ground-state half-lives; unbound nuclei lie along the dripline and are colored in grey, stable nuclei are colored black and form the valley of stability along the central diagonal of the chart, the remaining nuclei have half-lives ranging from milliseconds (light green) to years (dark blue). One should note that the chart does not follow a trend set by $N = Z$; the chart favors neutron-rich nuclei as Coulomb repulsion between many protons tends to prevent binding of nuclei with small N/Z ratios. Also depicted in Fig. 1.4 is an inset depicting the region near doubly magic ^{40}Ca. The $A = 38$ isobaric triplet of Ca, K, and Ar is shown, as is the $A = 39$ doublet of Ca and K, both of which constitute the focus of this work.

While the magic numbers from 8 through 126 guided structure studies in the era following

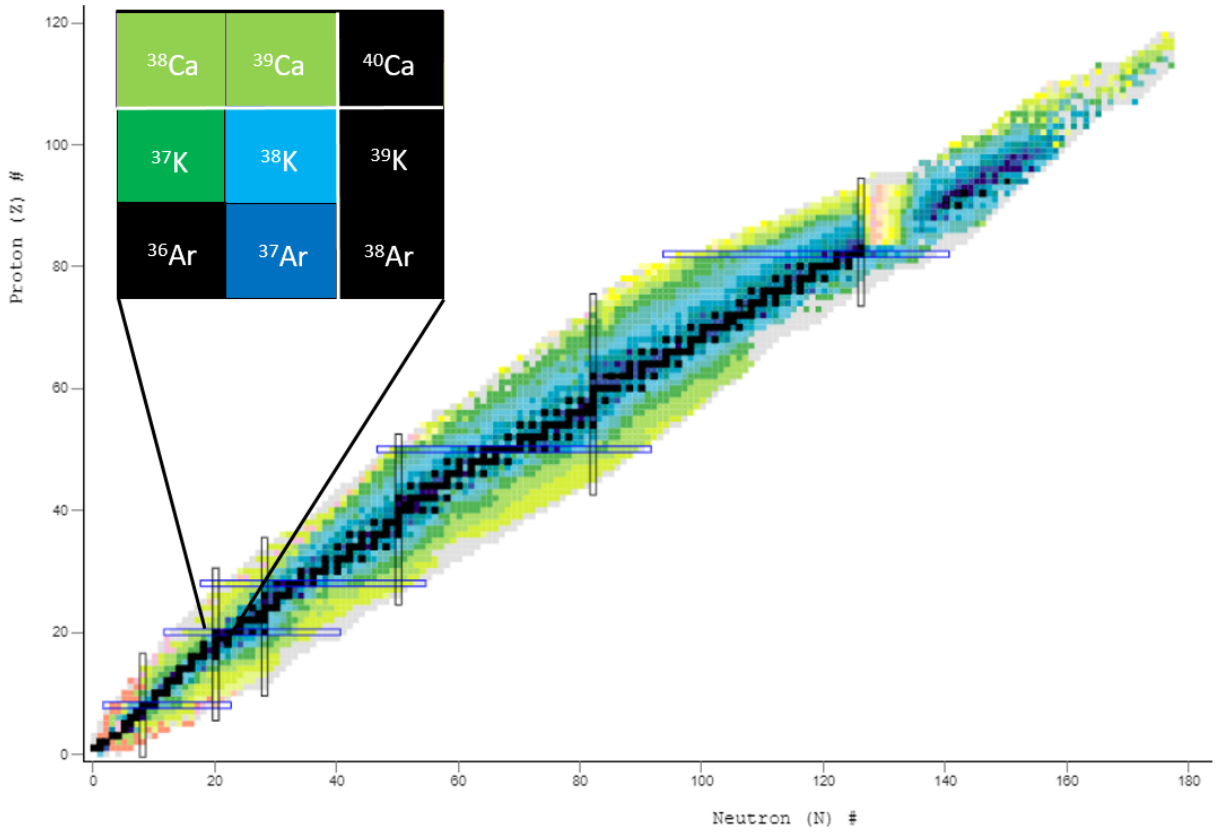

Figure 1.4 The nuclear chart. Nuclei are arranged by atomic number Z and neutron number N. The color scheme is representative of the ground-state half-life with the valley of stability depicted in black, grey areas representing the unbound nuclei, and nuclei with lifetimes ranging from single milliseconds (light green) to years (dark blue). Vertical and horizontal rectangles outline the traditional magic numbers. The inset depicts the area near doubly magic ^{40}Ca with mirror nuclei ^{39}Ca and ^{39}K and the $T = 1$ isobaric triplet of ^{38}Ca, ^{38}K, and ^{38}Ar. The figure has been adapted from Ref. [33].

their description by Mayer and Jensen, as research pushed further away from stability the idea of immutable closed shells and permanent magic numbers was supplanted by the concept of shell evolution. Traditionally, nuclei have been modeled as single particles bound by a mean field potential, such as the one presented in Fig. 1.2. While this model simplifies the problem of n-bodies each interacting with the other through the strong and Coulomb interactions, a problem which quickly becomes unwieldy at even low A, it may struggle to describe sudden changes in binding energy, nuclear radii, and transition strengths with respect to neighboring nuclei.

Some of the first indications of shell evolution were observed in what is now known as the "island of inversion", where the $N = 20$ shell closure appears to decrease, resulting in first excited

states with unusually low energy [34]. One such famous example is the case of ^{32}Mg, which lies at the heart of the island of inversion and is characterized by a first 2^+ state at 885 keV; one can compare this to the doubly magic ^{40}Ca with a first 2^+ state residing at 3.9 MeV, or many non-magic nuclei with first 2^+ states typically near 2 MeV in this mass region. In the traditional spherical shell-model picture, the ground state of ^{32}Mg should be characterized by a fully occupied $1d_{3/2}$ orbital; but due to a reduction in the $N = 20$ shell gap the ground state is, in fact, described by a 2-particle 2-hole ($2p - 2h$) configuration with two neutrons occupying the $1f_{7/2}$ or $2p_{3/2}$ orbitals, leaving the $1d_{3/2}$ orbital unfilled. Similarly, the ground-state band 4^+ state has been shown to exhibit high collectivity with B(E2) strengths indicating significant contributions from $2p - 2h$ and $4p - 4h$ configurations [35].

The intruder configurations in the island of inversion may be difficult to explain with a traditional spherical shell-model, but when one introduces nuclear deformation, which is closely tied to the collective motion of nucleons, the evolution of shell gaps may be explained by the reduction or even inversion of level energies and intruder configurations which become energetically favorable. In fact, as the $1d_{3/2}$ single-particle energy moves closer to the $1f_{7/2}$ orbital, one expects an increase in contributions from $2p - 2h$ and $4p - 4h$ configurations as single-particle cross-shell excitations into the $1f_{7/2}$ would result in negative parity states which are not observed [25]. Also, with the reduction of the $N = 20$ shell gap one would expect a shell gap to appear at $N = 16$ arising from an increased gap between the $1d_{3/2}$ and $1s_{1/2}$ orbitals. Indeed, such behavior has been observed near the neutron drip line [36].

While it is now common to expect shell evolution in exotic nuclei with large N/Z asymmetries, there are still opportunities to uncover cross-shell excitations and loss of magicity near stability, making the nuclei in close proximity to doubly magic ^{40}Ca a region suitable for close examination with highly sensitive experimental probes. This work is aims to reveal possible cross-shell excitations in less exotic nuclei by examination of the electromagnetic transition which is governed by the multipole operator $\mathscr{O}(\pi\lambda)$, where π is either electric E or magnetic M and λ is rank of the operator as defined by the change in angular momentum l from the initial and final states of the

electromagnetic transition.

When a photon is released by the transition of a nucleus from an initial state J_i to a final state J_f, the photon of spin $S = 1$ will carry an amount of angular momentum l such that $\vec{l} = \vec{J}_i - \vec{J}_f$. The amount of angular momentum carried by the photon is given by the triangle relation $|J_i - J_f| \leq l \leq J_i + J_f$, where l is an integer. If the transition results in a change of parity, the allowed l are odd for electric transitions and even for magnetic transitions; e.g., transitions such as E1, M2, E3, etc... If there is no change in parity between the initial and final states of the transition, the allowed l are odd for magnetic transitions and even for electric transitions; e.g., M1, E2, M3, etc... The multipolarity of the gamma radiation is defined by the angular momentum carried by the photon where $l = 1$ defines a dipole transition, $l = 2$ a quadrupole transition, and $l = 3$ is an octupole transition with higher-order transitions occurring in nuclei of large mass A.

This work is focused on the electric quadrupole (E2) transition and particularly the reduced transition strength

$$B(\mathrm{E2}) = \frac{|\langle J_f| \, |\mathscr{O}(\mathrm{E2})| \, |J_i\rangle \, |^2}{(2J_i + 1)} \tag{1.1}$$

and the proton ($k = p$) and neutron ($k = n$) matrix elements

$$M_k = \langle J_f| \, |\mathscr{O}(\mathrm{E2})| \, |J_i\rangle \tag{1.2}$$

where the one-body electric transition operator is given by

$$\mathscr{O}(E\lambda) = r_k^\lambda Y^\lambda(\hat{r}_k) e_k e \tag{1.3}$$

with $\lambda = 2$ for quadrupole transitions, r_k giving the radial component of proton or neutron, Y representing the angular components as spherical harmonics , e_k representing the charge of the proton or neutron, and e the fundamental charge [37]. The one-body operator acts on a single particle (proton or neutron) and the overlap between the final and initial states represents the transition of that particle between the states. Similarly, two-body operators may be introduced to connect states with multiple particles.

Once the Hamiltonian has been solved for the eigen wave functions, the matrix element is calculated from the overlap of final and initial states with $\mathscr{O}(E2)$ according to Eqn. 1.2. The

matrix elements calculated for ($J_i \rightarrow J_i$) provide the quadrupole moment of state J_i, while those calculated for ($J_i \rightarrow J_f$) provide the reduced transition strength B(E2) (also known as the reduced transition probability) between states J_i and J_f, with "reduced" referring to the matrix element being independent of the total angular momentum projection M_J. Experimentally, the B(E2) can be calculated from measurements of the gamma-ray energy E_γ, the half-life $T_{1/2}$ of the initial state, and branching ratio b such that

$$B(\mathrm{E2}) = \frac{564 \cdot b}{E_\gamma^5 T_{1/2}} e^2 fm^4 \tag{1.4}$$

where the constant contains units of MeV^5ps, making the reduced transition strength a valuable measurement for testing nuclear structure models and fitting effective interactions.

For an effective interaction which can be used to predict B(E2) values in the framework of shell models, the effective charges e_n and e_p (for the neutron and proton, respectively) are employed as a type of free parameter to account for properties of the model which may not be included or accurately represented in the interaction such as core polarization, nucleon configurations within the core, and orbitals that have been truncated from the model space but affect the accuracy of the calculated B(E2) when compared to experimentally obtained values. If the free-nucleon charges $e_p = 1.0$ and $e_n = 0$ are naively used for an effective interaction, the calculated results for the proton matrix element M_p tend to predict values less than the experimentally determined values, as shown in the top-left panel of Fig. 1.5. To correct for these deficiencies, the bare proton A_p and bare neutron A_n matrix elements are calculated from the effective interaction and then scaled by the effective charges to determine the transition matrix element M_p according to

$$M_p = e_p A_p + e_n A_n \tag{1.5}$$

These bare matrix elements allow M_p to be described in terms of proton and neutron components calculated with the free-nucleon charges and, as in the lower two panels of Fig. 1.5, may be used to compare the results of effective interactions against each other. Similarly, under the assumption of isospin symmetry, the neutron matrix element M_n, which may be difficult to precisely determine

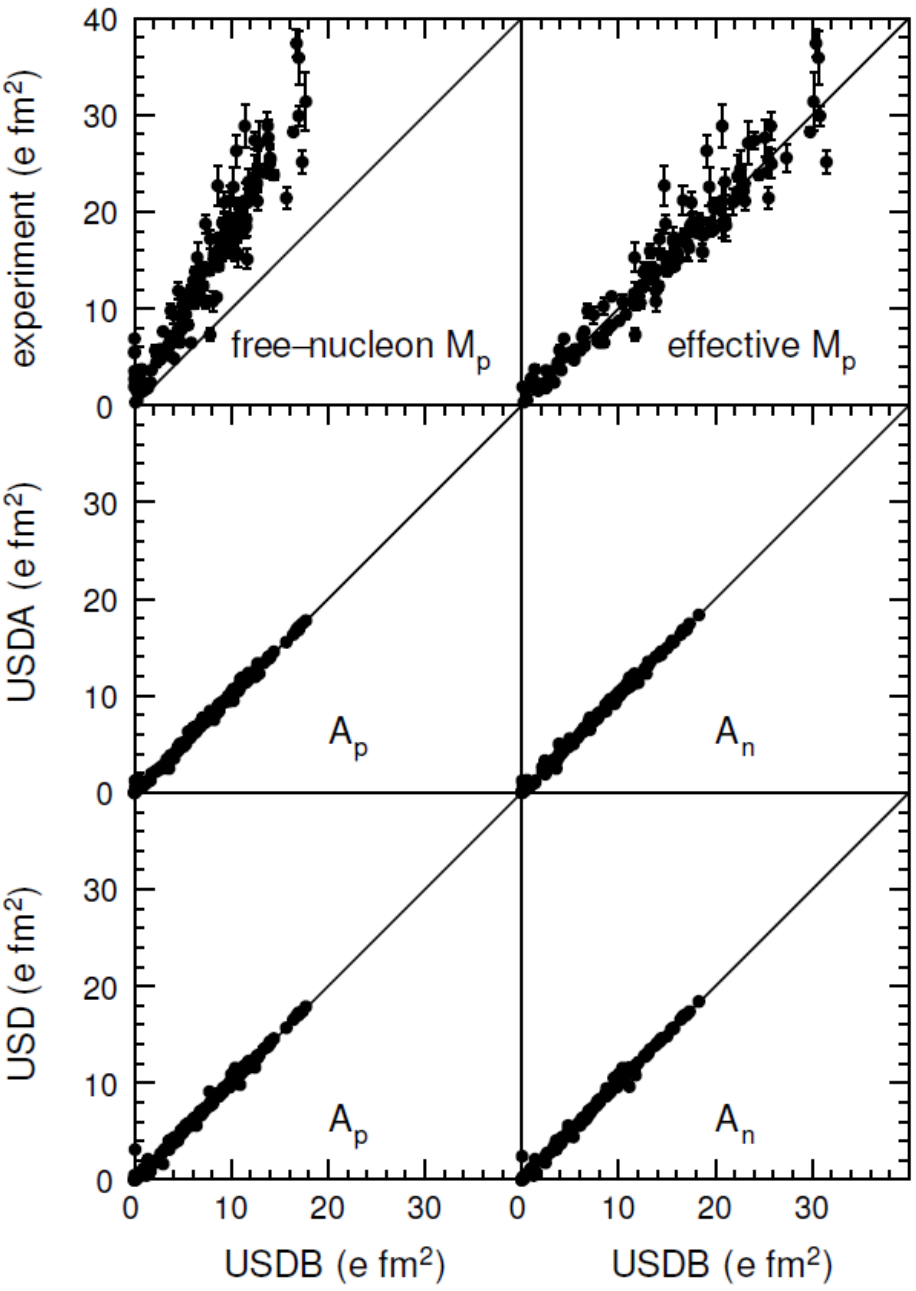

Figure 1.5 E2 transition matrix elements calculated with the USD, USDA, and USDB Hamiltonians which utilize two-body matrix elements and single-particle energies to fit 608 states over 77 *sd*-shell nuclei ranging from $A = 16$ through $A = 40$ [38]. Top: Experimental values of M_p(E2) compared to calculation with the USDB effective interaction using free-nucleon charges $e_p = 1.0$ and $e_n = 0$ (left) and effective charges $e_p = 1.36$ and $e_n = 0.45$ (right). Middle: Comparison of the bare matrix elements A_p and A_n calculated with the USDA and USDB effective interactions. Bottom: Comparison of A_p and A_n calculated with the USD and USDB effective interactions [39]. Reprinted figure with permission from W.A. Ritcher, B.A. Brown *et al.*, Phys. Rev. C, vol. 78, p. 064302 (2008). Copyright (2024) by the American Physical Society.

by experiment, can be calculated with effective charges and bare matrix elements [40] with

$$M_n = e_p A_n + e_n A_p. \tag{1.6}$$

The values of these effective charges may depend on the model space; where common values for the fp space may be $e_p = 1.5$ and $e_n = 0.5$ [41], or $e_p = 1.36$ and $e_n = 0.45$ for the sd space [42]. When effective charges are used, the M_p calculated from the effective interactions are increased and tend to agree with the experimental values, as can be seen in the top-right panel of Fig. 1.5.

The neutron matrix element M_n for a transition may be experimentally obtained, though, from the same transition in a mirror nucleus via the relation

$$M_n(-T_z) = M_p(+T_z) \tag{1.7}$$

where the neutron matrix element from the nucleus with isospin projection $-T_z$ is equivalent to the proton matrix element from the nucleus with $+T_z$ [40]. For this work, the proton matrix element $M_p(^{38}\mathrm{K})$ of the mirror $11/2^- \rightarrow 7/2^-$ transition provides the neutron matrix element $M_n(^{38}\mathrm{Ca})$. Using this isospin decomposition method for mirror transitions leads to a fuller picture of the transition and provides the method employed in this work to compare matrix element trends between isobars of different isospin projection T_z by comparing the ratio of matrix elements M_n/M_p.

1.2 Systematic Trends in Matrix Element Values

Previous work has formulated that the proton matrix elements M_p for the $2^+ \rightarrow 0^+$ E2 transitions (M_p(E2)) of $T = 1$ isobaric triplets should follow a linear trend as a function of isospin projection T_z according to

$$M_p(T_z) = \frac{1}{2}(M_0 - M_1 T_z) \tag{1.8}$$

with M_0 and M_1 representing the isoscalar and isovector components, respectively [40]. Generally, the isovector component M_1 is positive in light nuclei and smaller than the isoscalar component M_0. This leads to many $T = 1$ isobars having $2^+ \rightarrow 0^+$ transition matrix elements of ratios $M_n/M_p < 1$ for proton-rich $T = 1$ nuclei, as observed in Fig. 1.6. While this trend holds over a wide mass range, a notable deviation has been observed in the $A = 38$ triplet of Ca, K, and Ar [43, 44], as observed

in the bottom-middle panel of Fig. 1.6. Cottle *et al*. [43] observed a significant enhancement in the ^{38}Ca matrix element, deviating from the trend set by the ^{38}Ar and ^{38}K matrix elements and therefore hinting at symmetry breaking. Indeed, assuming perfect isospin symmetry and a single closed-shell model, one would expect M_p for the $2^+ \rightarrow 0^+$ transition in ^{38}Ca to be near zero and therefore expect a large ratio $M_n/M_p >> 1$.

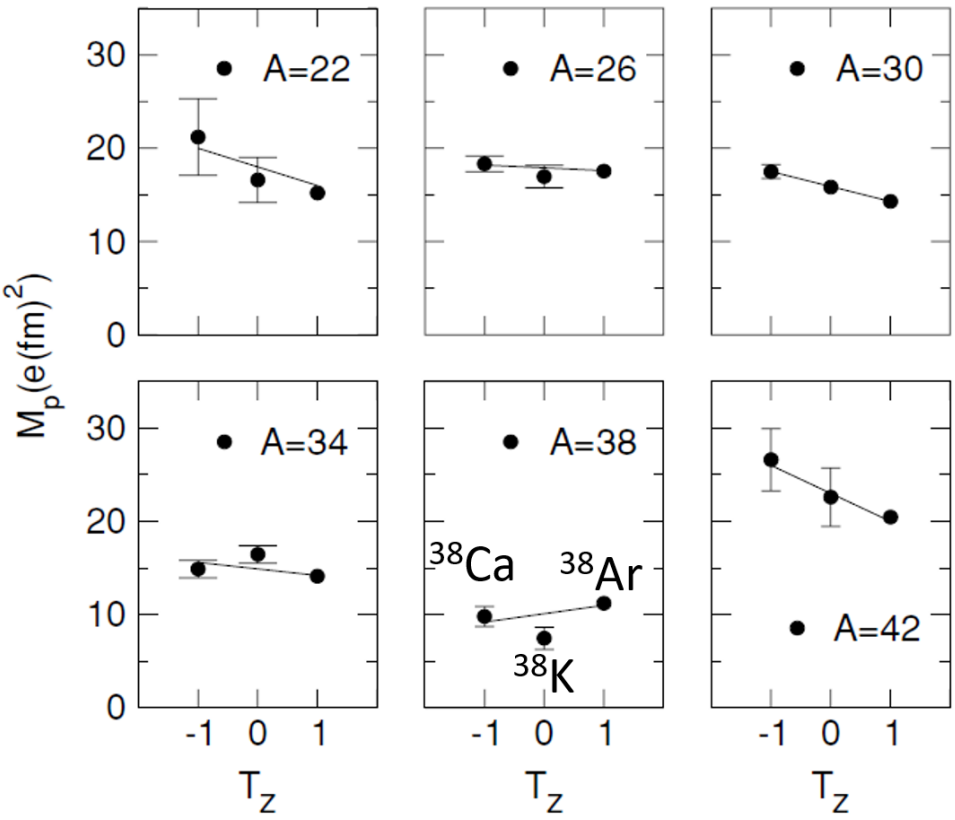

Figure 1.6 Proton matrix element values M_p plotted as a function of isospin projection T_z for the $2^+ \rightarrow 0^+$ E2 transition in six $T = 1$ isobaric triplets [44]. Reprinted figure with permission from F.M. Padros Estévez, A.M. Bruce *et al*., Phys. Rev. C, vol. 75, p. 014309 (2007). Copyright (2024) by the American Physical Society.

The expectation of a large M_n/M_p ratio for single closed-shell nuclei can be derived from some naive shell-model assumptions starting with Eqn. 1.5. If we assume a single-closed proton shell for calcium isotopes, then the matrix element will be comprised exclusively of neutron components $M_{p,38Ca} = e_n A_n$. Similarly, assuming a single-closed neutron shell for argon implies that its matrix element will contain only proton terms $M_{p,38Ar} = e_p A_p$. Making no assumptions about the sign of

the matrix elements, we square of the ratio and find that

$$\left(\frac{M_{n,38Ca}}{M_{p,38Ca}}\right)^2 = \left(\frac{M_{p,38Ar}}{M_{p,38Ca}}\right)^2 = \left(\frac{e_p A_{p,38Ar}}{e_n A_{n,38Ca}}\right)^2 = \left(\frac{e_p}{e_n}\right)^2 \tag{1.9}$$

where, due to mirror symmetry, we expect $A_{p,38Ar} = A_{n,38Ca}$, which cancels the bare matrix element terms in the ratio and leaves a ratio of matrix elements equal to the ratio of effective charges $\frac{e_p}{e_n}$. Using commonly accepted effective charge values from the USD, USDA, and USDB Hamiltonians $e_p = 1.36(5)$ and $e_n = 0.45(5)$ [38] and the isospin decomposition equivalency in Eqn. 1.7, we find an expected ratio of

$$\frac{M_{n,38Ca}}{M_{p,38Ca}} = \frac{e_p}{e_n} = 3.0(4) \tag{1.10}$$

which is much larger than the experimentally determined ratio of $M_{n,38Ca}/M_{p,38Ca} = 1.1(1)$ for the $2^+ \rightarrow 0^+$ transition. This discrepancy reinforces the importance of the choice of effective charges in nuclear shell-model calculations as well as the unrealistic nature of the closed-shell assumption. The idea of a single-closed shell is naive as nuclear excited states are comprised of many different configurations existing in a superposition of states with some configurations more probable than others. And when effects from collective motion, deformation, and shell evolution are considered, expectations may change drastically.

For the $A = 38$ isobars, Cottle *et al.* called for a more precise measurement of the $T_z = 0$ matrix element in ^{38}K, suggesting that such a measurement would strengthen their argument for an enhanced ^{38}Ca proton matrix element. The call for a better measurement of the $T = 1$, $2^+ \rightarrow 0^+$ transition in ^{38}K would be answered by Estèvez *et al.* [44] who concluded that the ^{38}Ca matrix element was larger than predicted based on their measurement of ^{38}K and shell-model calculations, furthering interest in the $A = 38$ anomaly. Since the publication of this finding, the error of the adopted value of $M_p(E2)$ for ^{38}K has be increased, again introducing ambiguity to the $T_z = 0$ data point [45]. But for the purpose of this work, we will focus on the ratio of the $T_z = +1$ and $T_z = -1$ matrix elements M_n/M_p, which is independent of the $T_z = 0$ data point.

For a larger overview of M_n/M_p systematics, Fig. 1.7 has been adopted from Figure 2 of Ref. [46] and plots M_n/M_p as a function of the mass number A for single closed shell (SCS)

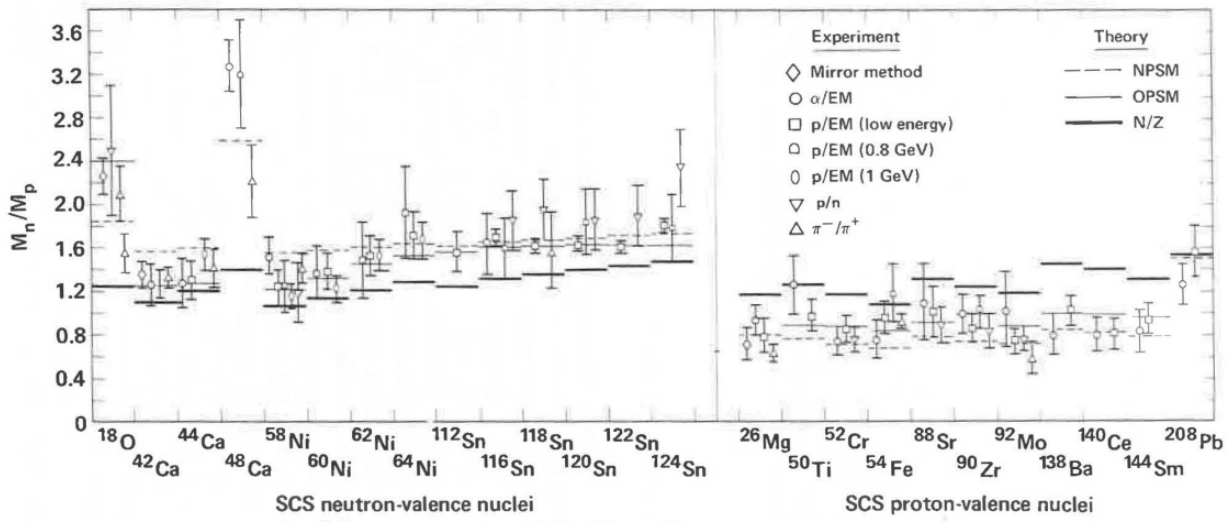

Figure 1.7 The ratios M_n/M_p for the lowest $2^+ \rightarrow 0^+$ transitions in various single closed shell (SCS) nuclei and doulby magic ^{48}Ca and ^{208}Pb. The data was obtained from hardon scattering experiments and the mirror method described by Eqn. 1.7. Measurements are compared to the homogeneous collective model expectation (N/Z), the no-free parameter schematic model (NPSM), and the one-free parameter schematic model (OPSM) [46]. Reprinted from Physics Letters B, Vol. 4, A.M. Bernstein *et al*. Neutron and proton transition matrix elements and inelastic hadron scattering, Pages No. 255-258, Copyright (1981), with permission from Elsevier.

nuclei. The data represent the most recent measurements of lowest lying 2^+ states at the time of publication and consist mainly of data obtained from hadron scattering experiments along with the mirror method described by Eqn. 1.7 for lighter nuclei. The data are compared to the homogeneous collective model in which the ratio of neutron (n) and proton (p) transition densities $\rho^n/\rho^p = M_n/M_p = N/Z$ [46], the no-free parameter schematic model (NPSM), and the one-free parameter schematic model (OPSM). One will notice that $M_n/M_p > N/Z$ for neutron-valence nuclei (closed proton shells) while, for proton-valence nuclei (closed neutron shells), the collective model over predicts the experimental data with $M_n/M_p < N/Z$. Both of these trends can be attributed to core-polarization effects which tend to push the M_n/M_p ratios back toward the collective model predictions. Subtantial deviations from the general trends in each panel are observed near doubly magic ^{48}Ca and ^{208}Pb; these deviations are attributed to $0\hbar\omega$ transitions in ^{48}Ca on the neutron side only while ^{208}Pb is characterized by both neutron and proton $0\hbar\omega$ transitions [47].

Over the past few years, there has been a surge of interest in proton excitation in the 0^+ ground

and 2^+ excited states of even-even, neutron-deficient calcium isotopes. In fact, given isospin conservation, another island of inversion should be located near unbound ^{32}Ca, being the neutron deficient island mirroring the neutron rich island near ^{32}Mg [48]. Due to the $Z = 20$ shell closure, the low-lying 2^+ states are usually considered to be comprised of a large fraction of closed proton-shell configurations, a reasonable assumption for a proton magic nucleus. But, recent examination has demonstrated that the ground states of ^{36}Ca and ^{38}Ca require proton excitations into the fp shells to explain the observed $B(\mathrm{E2}; 0^+ \rightarrow 2^+)$ transition strengths [49] and the cross-section ratio $\sigma(2^+_1)/\sigma(0^+)$ of ^{36}Ca measured in the $2n$ removal reaction from ^{38}Ca [50]. Dronchi *et al*. [49] concluded that a fraction of proton closed-shell configurations as low as 50% best replicates the $B(\mathrm{E2}; 2^+ \rightarrow 0^+)$ for both ^{36,38}Ca, which is reinforced by the results of Beck *et al*. [50]. Naturally, the enhancement of the proton matrix elements of ^{36,38}Ca motivates the study of neighboring Ca isotopes to determine if this enhancement persists. Furthermore, since mirror transitions can be effectively used to study the isospin decomposition of transition strengths [40], this work will examine ^{39}Ca and ^{39}K mirror nuclei to understand the relative importance of proton and neutron contributions to core excitations in the vicinity of doubly magic ^{40}Ca.

More recent systematic studies have been conducted [51] for the isoscalar M_0 and isovector M_1 components for $2^+ \rightarrow 0^+$ transitions in odd-odd nuclei in the lower mass region as shown in Fig. 1.8. Most apparent are the flat trend of isovector values at approximately 0 efm^2, suggesting that nuclei on $N = Z$ up to $A = 74$ are most significantly characterized by their isoscalar components, and the sharp increase of isoscalar values starting near the closing of the sd shell near $A = 40$, suggesting increased collectivity in this region. Interestingly, the isoscalar components of the odd-odd $T = 1$ isobars trends simultaneously with the isoscalar components of the even-even $T = 0$ nuclei, as shown by the solid line and uncertainty band. This similarity implies that the collectivity observed in the $T = 0$ and $T = 1$ states may have a common origin and this implication is supported by work which examines the pairing correlations in $T = 0$ states and puts them on par with pairing in the $T = 1$ states [52].

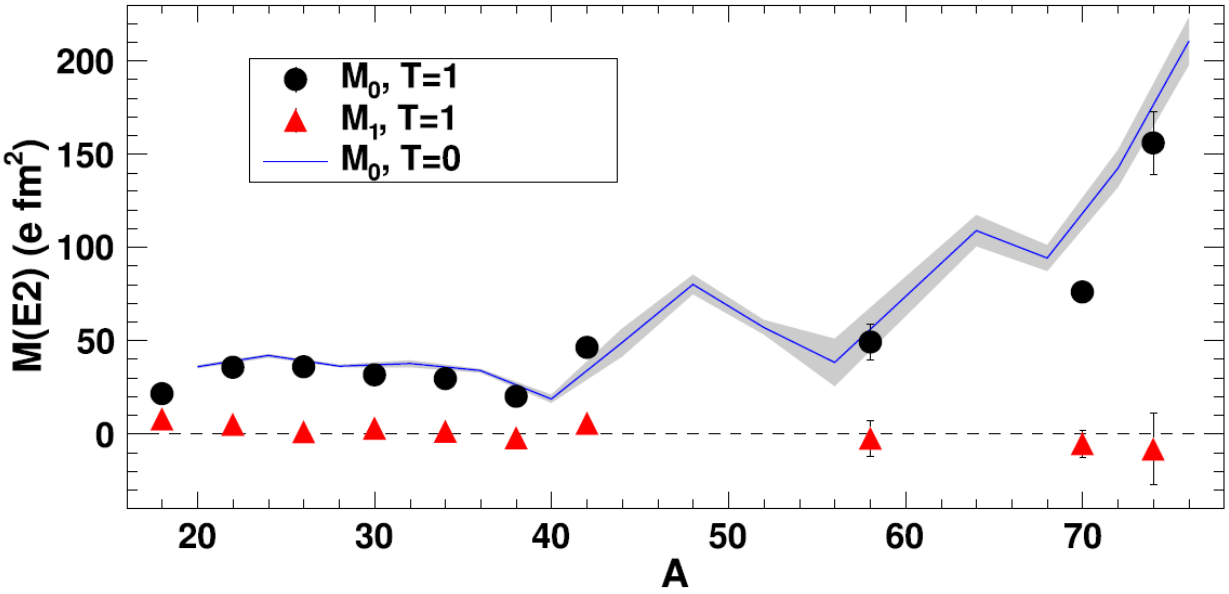

Figure 1.8 The isoscalar M_0 (black circles) and isovector M_1 (red triangles) components the of the $2^+ \rightarrow 0^+$ transitions for odd-odd $T = 1$ nuclei across a wide, low-mass region of the nuclear chart. The figure shows relatively no change in the isovector components while isoscalar components begin a sharp increase near $A = 40$, where the *sd* shell becomes maximally occupied. Additionally, the matrix elements derived from even-even $T = 0$ nuclei along $N = Z$ are provided by the solid line. The isoscalar components of the $T = 1$ nuclei appear to trend accordingly with the isoscalar values from the $T = 0$ nuclei. The figure has been adopted from Figure 4 of Ref. [51].

1.3 Analog Transitions in Mirror Nuclei ^{39}Ca and ^{39}K

As observed in Fig. 1.6, it has been suggested that the $2^+ \rightarrow 0^+$ transition matrix element M_p in ^{38}Ca is enhanced with respect to the linear trend set by ^{38}Ar and ^{38}K [43, 44]. In an effort to add systematic context to this suggestion, we have examined an analog transition in ^{39}Ca to determine if this enhancement persists in neighboring nuclei. The $(11/2^-) \rightarrow 7/2^-$ transition in ^{39}Ca is expected to be structurally related to the $2^+ \rightarrow 0^+$ transition in ^{38}Ca if we naively assume the $Z = 20$ shell closure and that the $(11/2^-)$ and $7/2^-$ states in ^{39}Ca can be modeled as an $f_{7/2}$ neutron coupled to a ^{38}Ca 2^+ or 0^+ core, respectively. In a similar fashion, the $11/2^- \rightarrow 7/2^-$ transition in ^{39}K can be related to the $2^+ \rightarrow 0^+$ transition in ^{38}Ar if we assume that the $11/2^-$ and $7/2^-$ states in ^{39}K can be formed by an $f_{7/2}$ proton coupled to an ^{38}Ar core. However, the situation is complicated by the fact that there can also be wave function components coming from the coupling of a proton (^{39}Ca) or neutron (^{39}K) to states of a $N = Z = 19$ ^{38}K core. Therefore, the present study of the quadrupole transitions in ^{39}Ca and its mirror ^{39}K aims to examine the M_p trend as a

function of the isospin projection. The data are also compared to shell-model calculations which employ effective interactions available to date in this mass region to understand the role of proton and neutron excitations near $Z = N = 20$.

In the following sections we will discuss the experimental design, procedure, and the analysis methods used to determine the reduced transition strengths B(E2) from the lifetime of the analog $11/2^-$ states in ^{39}Ca and ^{39}K. We will also provide an improved lifetime measurement for the mixed M1+E2 $9/2^-$ transition in ^{39}Ca with a significantly decreased error from the previously obtained measurement.

CHAPTER 2

EXPERIMENT

The measurements discussed in this dissertation are the results of an experiment performed in 2019 at the National Superconducting Cyclotron Laboratory (NSCL). An overview of the NSCL beam line is provided in Fig. 2.1. The aim of this study was to determine the lifetime of the $11/2^-$ state in ^{39}Ca via the Recoil Distance Method (RDM). From the lifetime of the state of interest, the reduced transition strength B(E2) and proton matrix element M_p would be determined, which would enhance our understanding of matrix element trends along the calcium isotopic chain in the neutron deficient region of the nuclear chart. Data were also available for the $11/2^-$ state in the mirror nucleus ^{39}K; therefore, the opportunity was taken to utilize the matrix element decomposition, where $M_n(^{39}\text{Ca})=M_p(^{39}\text{K})$, to provide a more detailed picture of the E2 transition [40]. Thus, the lifetime of the analog $11/2^-$ state in ^{39}K was determined for two purposes: to validate the analysis method used for ^{39}Ca, and to determine the neutron matrix element M_n for the state of interest. Additionally, a measurement of the $9/2^-$ state of ^{39}Ca was obtained, being that the plunger distance settings were sensitive to the lifetime of this state, which provided a more precise measurement than was obtained from the only previous measurement [53].

In this chapter the relevant devices used to perform the experiment will be described in detail. We will begin with the production of the stable ^{58}Ni primary beam by the Superconducting Source for Ions (SuSI) [54] and acceleration of the beam up to 160 MeV/u via the Coupled Cyclotrons [55]. Then we will move down the beam line to the A1900 Fragment Separator [56] where the ^{42}Sc secondary beam was selected and discuss the process of isotope separation via magnetic rigidity. Finally we follow the secondary beam to the S3 vault where inverse-kinematics reactions on the TRIPLEX [57] target produced ^{39}Ca and ^{39}K recoil nuclei in excited states. Gamma rays emitted from the excited nuclei were detected by GRETINA [58, 59] and the recoil nuclei were identified by the S800 Spectrograph [60]; both of these devices and their use in tandem will be described in this chapter. From this powerful combination of devices we are able to measure lifetimes of excited states which exist for only 10s of picoseconds and perform model independent determination

of reduced transition strengths where other techniques such as Coulomb excitation may not be applicable.

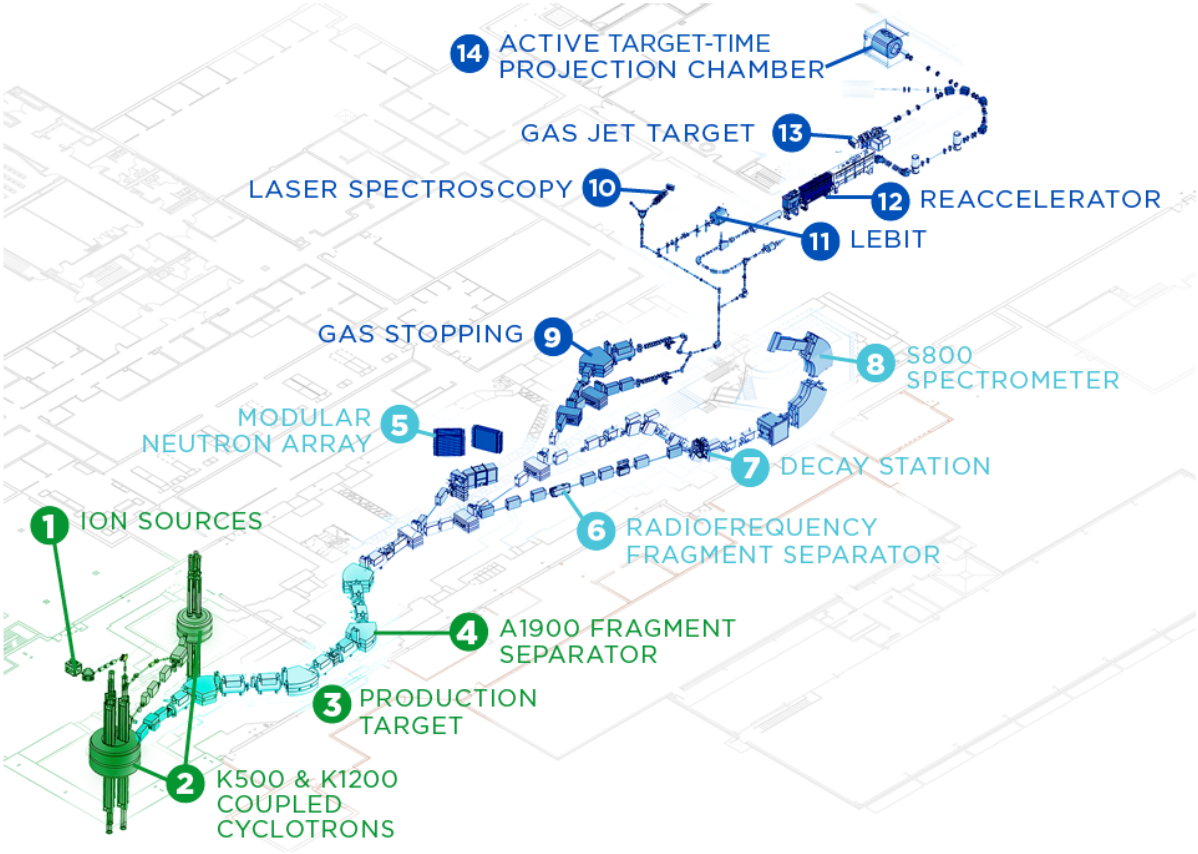

Figure 2.1 Beam line of the National Superconducting Cyclotron Laboratory (NSCL) [61]. The Superconducting Source for Ions (1) feeds ions to the Coupled Cyclotrons (2) which accelerates the primary beam particles to their maximum energy. The primary beam impinges on a production target (3) in which fragmentation reactions create a beam of various species of nuclei. These species are separated by the A1900 Fragment Separator (4) to produce the desired secondary beam(s). The secondary beam is sent to the S3 vault where TRIPLEX and GRETINA (sections 2.5.1 and 2.4.1, respectively) are located at the base of the S800 Spectrometer (8). Nuclei in excited states are produced in reactions on the TRIPLEX target, gamma rays are detected by GRETINA, and the recoil nuclei are identified by the S800. The beam may also be directed to other vaults where detectors such as the MONA (5) and the decay station (7) may be utilized. The beam can also be stopped and reaccelerated by the ReA facility (12) which directs a lower energy beam (single MeV/u) to a variety of other detectors such as the ATTPC (14) and SOLARIS (not depicted). The figure has been adopted from Ref. [61].

2.1 Primary Beam Production

For this experiment, a primary beam of ^{58}Ni was created by the combination of SuSI and the CCF. This primary beam was accelerated up to an energy of 160 MeV/u and then impinged on a

^{9}Be production target to produce fragments which could be separated by their magnetic rigidity and selected for secondary beam development in the A1900 fragment separator.

In the following sections we will describe the design principles and operation of the Superconducting Source for Ions (SuSI) and the Coupled Cyclotron Facility (CCF) which were used to create the ^{58}Ni primary beam.

2.1.1 Superconducting Source for Ions (SuSI)

The first step of the rare isotope production begins with the Superconducting Source for Ions (SuSI) [54]. A metallic source foil of ^{58}Ni is heated within an oven until a phase change produces ^{58}Ni in a gaseous state which is injected into the 100-mm diameter plasma chamber. Inside the chamber, magnetic fields on the order of 10^{0} T are created by tunable superconducting magnets and free electrons are injected into the chamber. The nickel atoms are then ionized by microwave radiation of approximately 18 GHz using the Electron Cyclotron Resonance (ECR) method. The ECR method is achieved by using magnetic fields B (created by multiple superconducting solenoids of various strengths) which are tuned to induce oscillation of both the ^{58}Ni ions and the free electrons to their respective cyclotron frequencies ω_c which are characterized by their unique charge-mass ratios q/m and described by the relation

$$\omega_c = \frac{q}{m}B \tag{2.1}$$

By applying a resonance frequency (RF) field to the oscillating particles, the kinetic energy of the free electrons is increased disproportionately compared to the more massive nickel ions. Collisions between the highly-energetic free-electrons and the heavier nickel atoms induces ionization, unbinding electrons from the nickel atoms and leaving the ^{58}Ni ions in a positively charged state. The nickel ions, existing in a variety of charge states, are then guided by electric fields to the coupled cyclotrons where the ions are accelerated up to the desired energy and their charge states are increased for more efficient acceleration, transmission, and separation by the A1900 Fragment Separator.

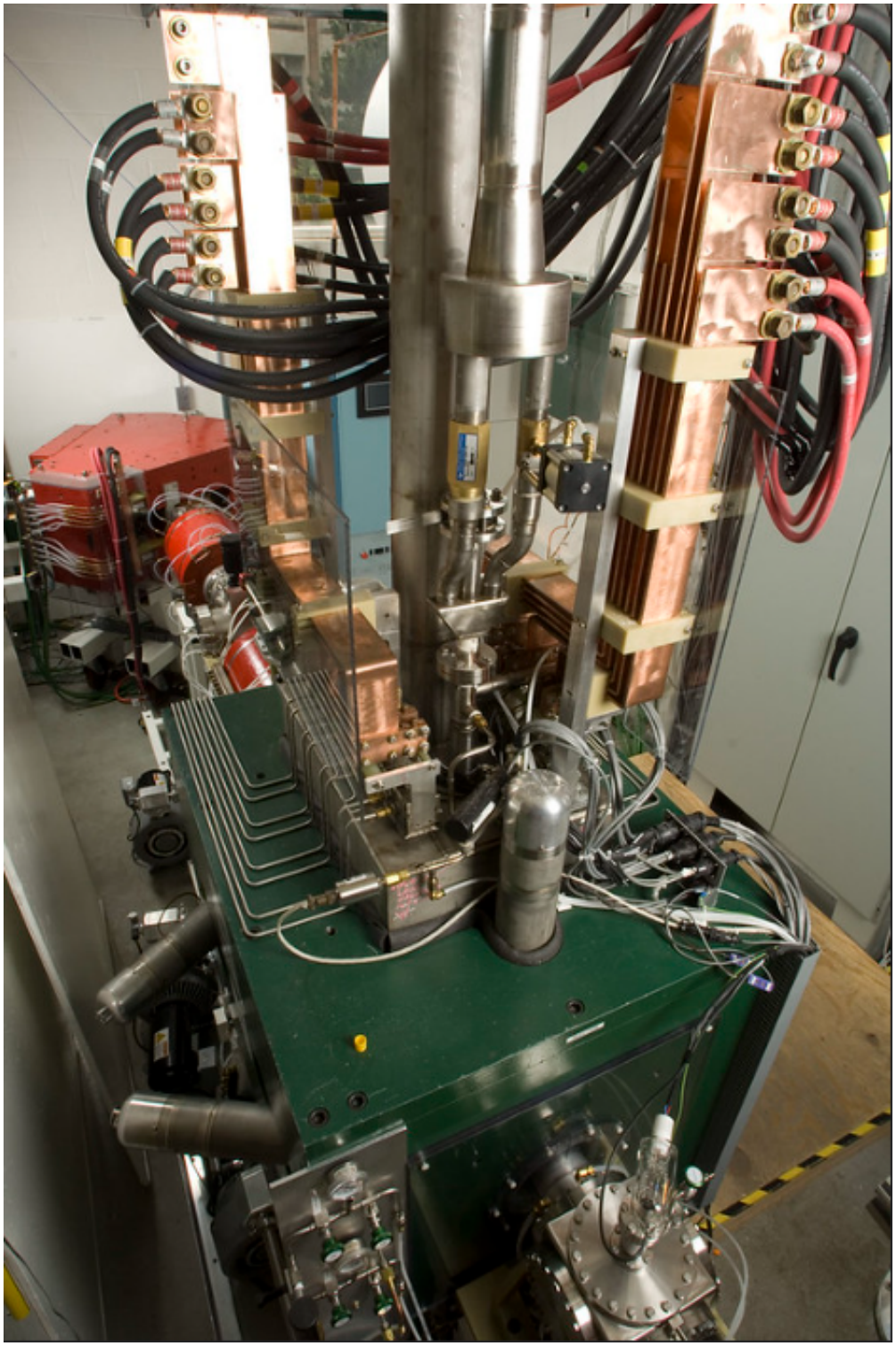

Figure 2.2 SUperconducting Source for Ions (SuSI) [54] at the NSCL. Inside the ion source, a gaseous ^{58}Ni is stripped of electrons with the Electron Cyclotron Resonance (ECR) method. Ions in a variety of charge states are ejected from the ion source and the beam is bent toward the Coupled Cyclotron Facility by the red dipole magnet. Photograph adopted from Ref. [62].

2.1.2 Coupled Cyclotron Facility (CCF)

The ^{58}Ni ions are transmitted to the Coupled Cyclotron Facility (CCF) [55, 63, 64] which is composed of a pair of coupled-superconducting cyclotrons, the K500 and K1200, where the suffix number represents the maximum kinetic energy (in MeV) that the cyclotron can accelerate a single proton to; i.e., the K500 can accelerate a proton to a maximum energy of 500 MeV and K1200 to and energy of 1200 MeV. The K500 cyclotron accelerates ^{58}Ni ions to an energy of approximately 10 – 20 MeV/u. At this energy, the ions are suitable for injection into the coupled K1200 cyclotron where the nickel ions are stripped of electrons to the desired charge state and accelerated to an energy of approximately 160 MeV/u. The nickel ions can then be guided to the ^{9}Be production target upon which reactions occur to create a "cocktail" beam of radioactive nuclei, from which the secondary beam can be isolated by the A1900 Fragment Separator.

Upon injection into the center of the K500 cyclotron (entering the cyclotron upward from the bottom), the nickel ions are subject to a magnetic field created by a superconducting magnet. The ions are bent by a Lorentz force acting perpendicular to the ion's velocity, sending the ions into a spiral trajectory emanating outward from the center of the cyclotron and ending at the ejection port in the outer radius. The positively charged nickel ions are accelerated by oscillating electric fields created by three "dee" electrodes, each separated by a gap as shown in Fig. 2.3. As the ions travel along the spiral trajectory they experience an electric potential, created by a pair of neighboring dees of opposite polarity, which accelerates the ions across the gap between each dee. The polarities of pairs of neighboring dees are switched at a frequency in accordance with the particular ion's cyclotron frequency. This alternating change in polarity between neighboring dees is timed such that the ions experience an acceleration as they cross the gaps between each of the dees. With each crossing of a gap between dees, the ions are accelerated to higher energies. Since the period of oscillation is independent of the ion velocity, the ion will traverse an increasingly longer path with each period of oscillation as its tangential velocity increases with each oscillation. When the ions reach their final period they are guided out of the K500 with a velocity of approximately 0.2c and directed toward the K1200 cyclotron.

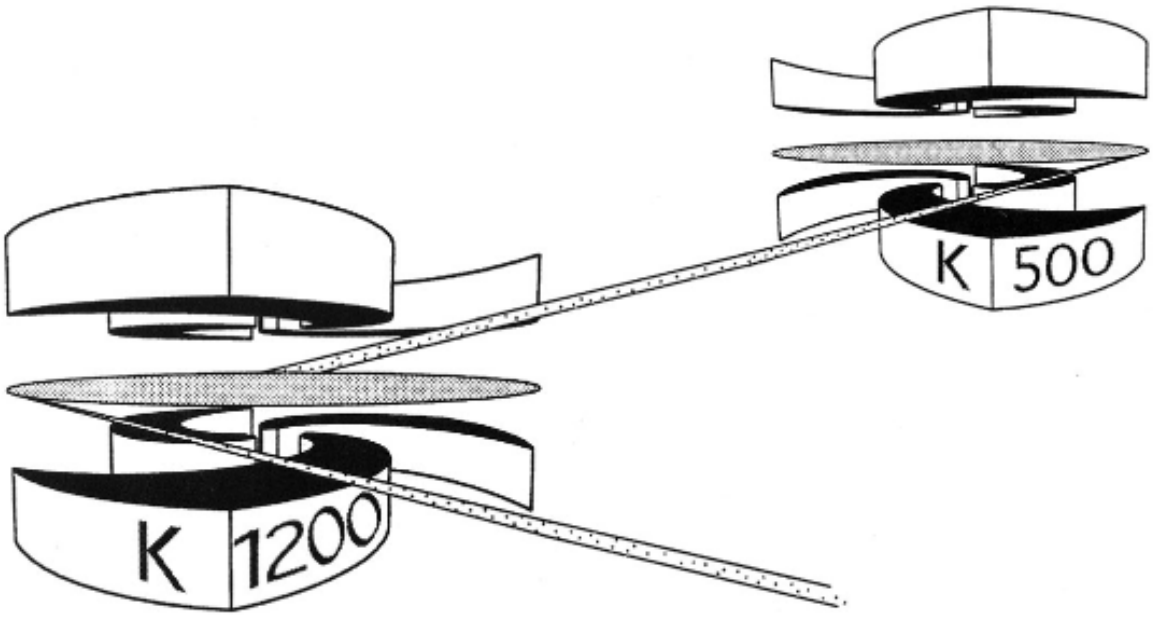

Figure 2.3 Coupled Cyclotron Facility design concept logo. [65]. The figure depicts the K500 and K1200 coupled cyclotrons and particles accelerated by the "dee" electrodes of the K500 which are then injected into the K1200 where they are accelerated to a higher energy, stripped of excess electrons, and then ejected toward the production target. The figure has been adopted from Ref. [65]. Reproduced with permission from Springer Nature.

Along the coupling line between the K500 and K1200 cyclotrons a combination of magnets is used to shape the beam profile to the specific matching conditions required for injection into the K1200. If we consider the z-axis to be parallel to the beam trajectory we then can build a coordinate system which includes the dispersive (x) and non-dispersive (y) axis. Upon ejection from the K500 the beam trajectory is bent 16° in the dispersive plane by a single dipole magnet. The beam then passes through a series of quadrupole magnet sets that alternately focus the beam along the x and y planes. Each quadrupole will focus the beam in one plane while dispersing it the other; thus, by using sets of alternately aligned quadrupoles a beam can be focused into a profile which is suitable for acceptance by the K1200. The coupling line utilizes a quadrupole singlet and four quadrupole doublets to achieve the proper beam profile before injection into the K1200.

The K1200 cyclotron works on the same principle as the K500 but ejects a beam of higher energy, higher intensity, and greater charge state. The placement of a carbon stripping foil in the ion's outward-spiraling path, approximately 30 cm from the center of the K1200, strips the

remaining electrons from the nickel ions. This stripper foil enables the K1200 to more efficiently accelerate ions as the higher charge state is more susceptible to the Lorentz bending force and the electric potential between the dees. Upon ejection from the K1200, the ^{58}Ni ions exist in their highest charge state and achieve a maximum energy of approximately 160 MeV/u. At this point the primary beam of ^{58}Ni has been produced and can be directed through another transmission line toward a production target.

The primary beam is impinged upon a ^{9}Be production target where a multitude of reactions occur to create a radioactive "cocktail" beam of nuclei of various charges, masses, and charge-mass ratios. To isolate a specific secondary beam or set of secondary beams the cocktail beam is transmitted to the A1900 fragment separator where the secondary beam(s) can be selected by their charge and charge-mass ratio.

2.2 Secondary Beam Development

The primary beam of ^{58}Ni impinges upon a ^{9}Be production target where interactions with the target material produce a variety of reaction products which can then be isolated with the A1900 Fragment Separator [56] by means of their magnetic rigidities and charge. After the secondary beam is separated by each species' unique radial dependence within the magnetic field of the last dipole, a set of slits at the focal plane of the A1900 rejects the undesired species, allowing only the desired secondary beam to pass to the transmission line leading to the experimental vault. In this experiment, the resultant secondary beam of rare isotopes was mainly composed of $N = 21$ isotones ranging from potassium ($Z = 19$) to vanadium ($Z = 23$) which were identified by their time-of-flight (TOF) as determined by two plastic scintillators along the beam line (section 2.3.1).

In this section we will discuss the principles of projectile fragment separation as they relate to the A1900 Fragment Separator shown in Fig. 2.4. We begin the discussion at the production target then move through the first two dipoles of the A1900 fragment separator which separates the reaction products by their magnetic rigidities. We will then move through the aluminum wedge-shaped velocity degrader, which further separates nuclei of similar A/Z by differential energy loss and charge squared (Z^2) dependence. A second pair of dipoles further separates the beam

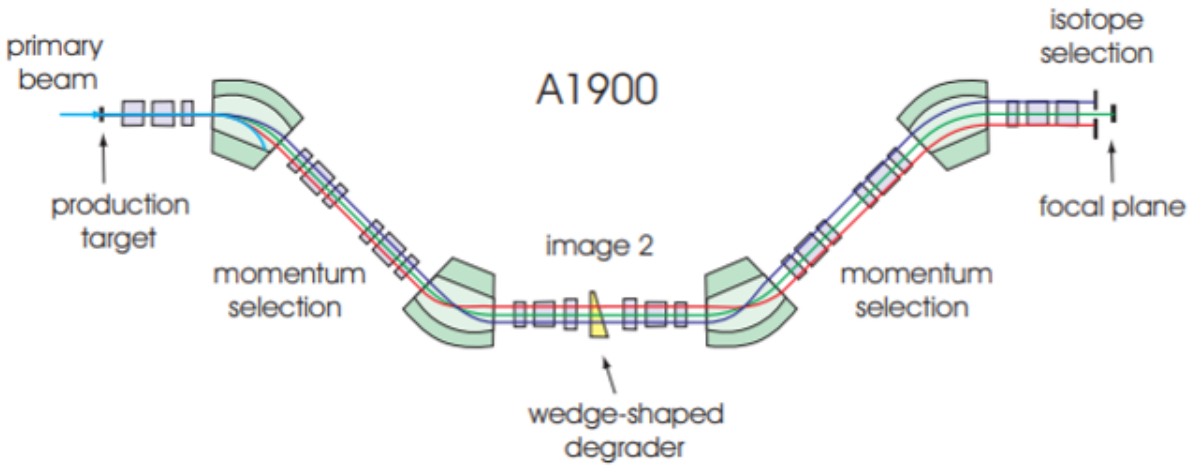

Figure 2.4 The A1900 Fragment Separator. The primary beam is directed from the CCF to the production target (left) where reactions produce various species of nuclei. Dipole magnets (green) bend the ions' trajectories (red, blue, and green lines) within the dispersive plane according to their magnetic rigidities. Sets of quadrupole magnets (small rectangles and squares) focus the beam after the production target, between dipoles, and before the focal plane slits (right). The dipoles are tuned to allow species of the desired mass-charge ratio A/Z to follow a central trajectory in the dispersive plane while the undesired ions are bent with larger or smaller radii ρ. An aluminum wedge separates ions of similar A/Z via differential energy loss thru the wedge-shaped degrader according the square of the ions' charge Z^2. A second set of two dipoles further separates the desired ions based on a different A/Z ratio. Finally, slits at the focal plane cut out ions moving outside the central trajectory, leaving the secondary beam to be transmitted to the experimental vault. The figure has been adopted from Ref. [66].

by a different rigidity dependence and sends the beam through the focal plane slits, which rejects undesired species and isolates the desired secondary beam before transmission to the experimental vault.

2.2.1 A1900 Fragment Separator

Upon ejection from the K1200 cyclotron the primary beam is directed toward a thick ^{9}Be production target. Stable beryllium-9 is a commonly preferred material for Rare Isotope Beam (RIB) production due to its high ratio of nucleons to areal density (high target number), its stability in atmosphere (unlike highly reactive lithium), and the tendency of the reaction products to remain in a forward-focused beam with a narrow angular distribution and momentum spread due to the minimal effect of Coulomb forces from the target, allowing easier transmission to the A1900 fragment separator.

Many models can be used to describe the reaction mechanism of projectile fragmentation but the common and intuitive abrasion-ablation model will suffice for this description. In the abrasion process, the projectile (beam) particles experience a shearing-off of nucleons by interaction with the stationary target nuclei. The resultant RIB, consisting mostly of ions with mass numbers less than the mass number of the incoming primary beam nuclei, tends to carry the forward momentum of each reaction product with little angular dispersion and a narrow momentum distribution due to minimal energy loss in the recoil fragments. Of course, there is some loss of kinetic energy in this interaction, but generally the fragmented projectiles continue along their initial trajectory with a velocity only slightly lower than the incoming projectile velocity. In the ablation process, the projectile fragments are in excited states and radiate excess energy as they continue along the beamline trajectory. The resultant RIB consists of a cocktail of dozens to hundreds of species of nuclei, all traveling within a narrow momentum and angular distribution, making transmission to the A1900 fragment separator by sets of focusing quadrupole magnets a process very similar to the coupling line described in section 2.1.2.

Upon entering the A1900 the RIB encounters a magnetic field created by the first dipole magnet. The dipole magnet bends each ion's trajectory by approximately 45° according to its magnetic rigidity. The magnetic rigidity $B\rho$, commonly cited in units of Tesla-meters (Tm), for a projectile fragment moving at relativistic velocity is given by the relationship

$$B\rho = \frac{m\nu}{q}\gamma \tag{2.2}$$

where B is the strength of the magnetic field, ρ is the fragment's radius of curvature, m and q are the mass and charge of the fragment, ν is the velocity, and Lorentz factor is given by $\gamma = \frac{1}{\sqrt{1-\beta^2}}$ where $\beta = \frac{\nu}{c}$. Although fragment separation is dependent on the momentum-charge ratio $m\nu\gamma/q$, in a suitable approximation we can assume that the various projectile fragments move with a common velocity $\nu\gamma$. Under this assumption, we find that the magnetic rigidity is associated with a fragment's mass-charge ratio

$$B\rho \propto \frac{m}{q} \propto \frac{A}{Z} \tag{2.3}$$

where A is total number of nucleons and Z is the number protons. With this approximation, it is clear that within a uniform magnetic field B, ions of identical mass-charge ratio $\frac{A}{Z}$ will have trajectories which are bent in the dispersive plane with a common radius ρ, while ions with different $\frac{A}{Z}$ ratios will follow trajectories of different radii. In this manner, the dipole magnets can be tuned to allow ions of the desired A/Z to follow a central trajectory through the A1900 while the undesirable fragments follow trajectories of larger or smaller radii and can be bent away from the central trajectory and separated from the desired secondary beam.

After exiting the field of the first dipole, ions which entered the dipole with nearly identical initial positions have been dispersed by the magnetic field into separate trajectories according to their rigidities. The dispersed fragments are refocused by two sets of quadrupole magnets and transmitted to the second dipole where they are bent again by 45° in the opposite direction. This second bending further separates fragments by their rigidity, placing them on parallel but spatially-separated paths in the dispersive plane.

After passing through a third set of focusing quadrupoles, the spatial separation of the fragmented beam is then exploited by the wedge-shaped aluminum velocity degrader pictured in yellow at image 2 in Fig. 2.4. Here, spatially separated fragments of similar A/Z will interact with the aluminum degrader and lose energy proportional to the square of their charge Z^2. Aluminum is a commonly preferred degrader material due to its high heat conductivity and the smaller mass number. As charged particles pass through the degrader material, differential energy loss in the degrader can be described in full by the Bethe-Bloch formula [67, 68] or approximated as $\frac{dE}{dx} \propto -Z^2$. Due to the differential energy loss and variable thickness of the wedge-shaped degrader, the beam exits the degrader with fragments of variable momentum which can then be further separated according to a different mass-charge dependence $\frac{A^{2.5}}{Z^{1.5}}$ [69]. The second pair of dipoles bends the beam ions according to this second mass-charge dependence and upon exiting the last dipole the beam fragments have maximal spatial separation in the dispersive plane.

The final secondary beam selection is accomplished by a set of slits placed at the focal plane of the A1900. The focal plane slits are orientated so as to reject ions of undesirable rigidity by

narrowing the aperture of the ejection port. The slits are adjusted to an aperture which allows the maximum number of ions aligned with the central trajectory to be transmitted while minimizing transmission of ions whose trajectories have diverged from the central trajectory.

Upon ejection from the A1900 the maximally purified secondary beam is transmitted through the A1900 focal plane scintillator (XFP), along the transmission line to the S800 object plane scintillator (OBJ), and then to the experimental vault where the S800 spectrograph is utilized to identify each particle on an event-by-event basis. The purpose of the XFP, OBJ, and E1 scintillators will be discussed in the next section along with the other components of the S800 spectrograph which are used to identify the secondary beam(s) and recoil nuclei resulting from reactions on the TRIPLEX plunger target.

In this experiment, the secondary beam was primarily composed of $N = 21$ isotones ranging from potassium to vanadium. Suffice it to say, of these isotones, the ^{42}Sc beam with an energy of 85.2 MeV/u and purity of 44% was selected for the present study as the ^{9}Be(^{42}Sc, ^{39}Ca)X reaction on the TRIPLEX target populated excited states of ^{39}Ca in greater yields than reactions from the other available secondary beams.

2.3 Particle Identification with the S800 Spectrograph

Though most of the primary beam will pass through the targets and degraders unreacted, the multitude of reactions that do occur can produce dozens of secondary beam fragments. Subsequent reactions between the secondary beam and the TRIPLEX target then produce dozens more species which must be identified. Thus, it is essential that the wide range of reaction products be identified on an event-by-event basis so that gamma rays detected by GRETINA may be associated with the particular nuclei from which they were emitted. The process of particle identification is accomplished by the S800 Spectrograph [60], a powerful machine capable of high resolution and broad acceptance achieved by the combined use of scintillators, cathode readout drift chambers (CRDCs), an ion chamber, and a hodoscope. The primary functions of the hodoscope are to identify an ion's kinetic energy and charge state as well as isomeric states which may only be detected by radioactive emission after implantation at the end of the focal plane; but this device was not utilized

for this work and shall not be discussed further.

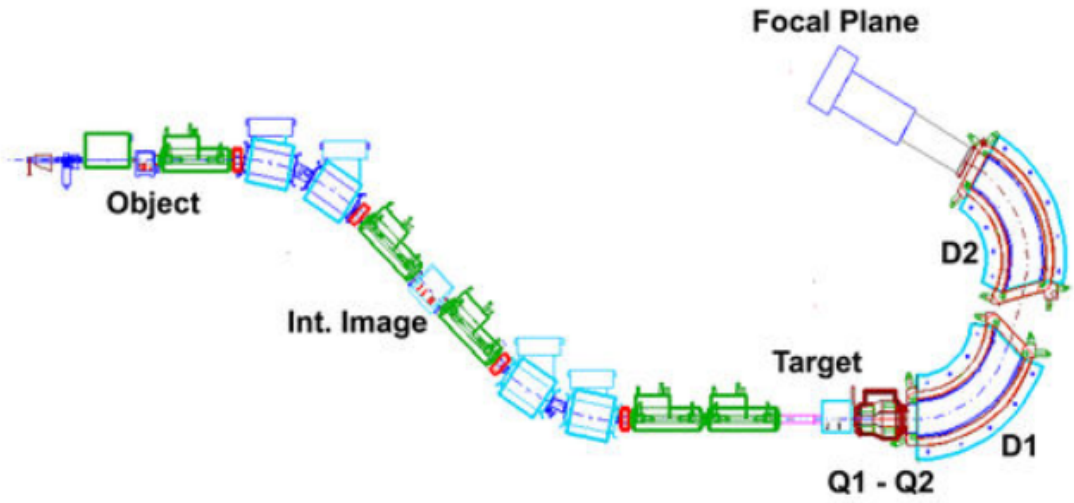

Figure 2.5 The S800 Spectrograph. After exiting A1900 focal plane scintillator XFP (left of diagram), the secondary beam components interact with the S800 object plane scintillator (OBJ). The time-of-flight (TOF) method is used to determine the secondary beam components with the E1 scintillator at the end of the focal plane acting as a reference and trigger. The focal plane and the detector components that comprise it are presented in Fig. 2.6. The figure has been adopted from Ref. [70].

In this section we will describe the process of particle identification by the various components which comprise the S800 spectrograph and discuss the basic working principles of each component. Beginning with XFP scintillator at the end of the A1900 we will discuss how the time-of-flight (TOF) method between the E1 and XFP, and E1 and OBJ scintillators is utilized to identify the secondary beam components. We will then describe how the CRDCs are used to determine ion trajectory in the S800 focal plane, which is subsequently used to determine each recoil nucleus's trajectory at the TRIPLEX target position. Finally we will describe how energy loss through the ion chamber is used in conjunction with the OBJ scintillator to identify recoil nuclei created by reactions between the secondary beam and the TRIPLEX production target.

2.3.1 Timing Scintillators

Upon ejection from the A1900 fragment separator, the secondary beam encounters a series of three plastic scintillators that act as simple counting mechanisms which record that an event occurred at a particular time. Due to the nature of the scintillator system, each scintillator provides

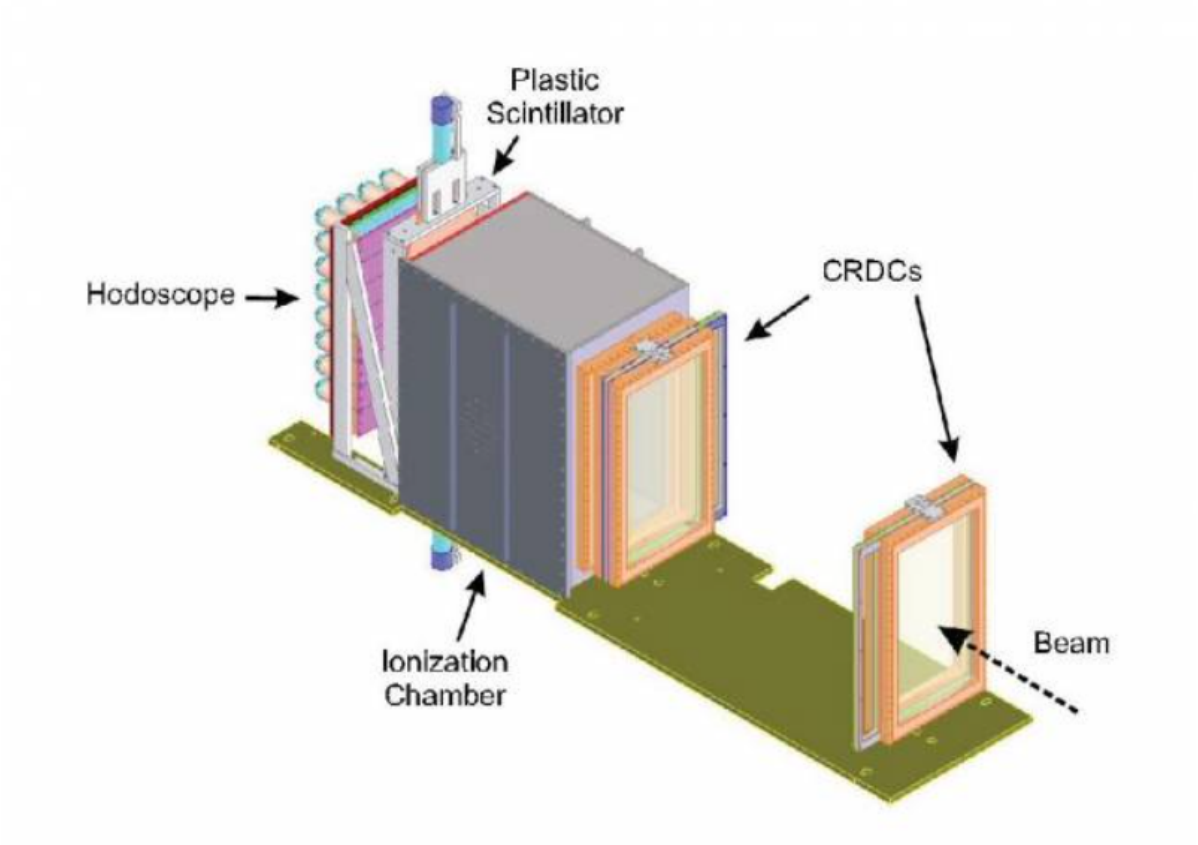

Figure 2.6 Focal plane of the S800 spectrometer. Detectors located at the focal plane include a pair of CRDCs which provide each ion's trajectory, an ion chamber which provides energy loss information, and the E1 scintillator (labeled "plastic scintillator") which acts as a trigger for the S800 DAQ and provides timing information from the XFP and OBJ scintillators. The IsoTagger hodoscope provides information about the ion's kinetic energy and charge state, and is also utilized for identifying long-lived isomeric states but was not utilized in this work. The figure has been adopted from Ref. [71].

a very fast timing resolution and can handle signal rates up to 1 MHz. These properties make the E1, XFP, and OBJ scintillator stations essential for particle identification at high beam intensities. The first scintillator is located at the A1900 focal plane (not displayed in Fig. 2.5) and is commonly referred to as the "XFP" scintillator, the second is located at the object position of the S800 in Fig. 2.5 and is referred to as the "OBJ" scintillator, the last scintillator is positioned at the end of the focal plane in Fig. 2.5 and is referred to as "E1". Here one should note that a pair of dipoles placed after the target position (D1 and D2 in Fig. 2.5) bends the ion beam, imposing a spatial separation between ions in the dispersive plane and a unique trajectory through the S800 defined by each ion's mass-charge ratio.

The scintillators are mainly composed of a polyvinyltoluene material which produces photons when energetic particles excite the scintillator atomic electrons into higher orbitals. The atoms then emit photons as the electrons deexcite to lower orbitals. The photons produced in the luminescence process are guided to two photomultipliers positioned at opposite ends of the scintillator block. When photons interact with the photocathode material, electrons are ejected from the cathode atoms in accordance with the photoelectric effect. The initially small electric signal from the ejected electrons is then multiplied up to a readable current, this signal can then be sent to the electronics stack where it can be digitized and recorded by the NSCLDAQ [72].

The E1 scintillator in the S800 focal plane provides a trigger for the coupled components of the S800 and GRETINA as well as providing a reference timing to which the XFP and OBJ timing can be compared to. For identification of the secondary beam $N = 21$ isotones, the time difference between the E1 and XFP scintillators was compared to the time difference between the E1 and OBJ scintillators (Fig. 3.2). To determine the relationship between an ion's mass-charge ratio and flight time we recall that, in the absence of an electric field, the Lorentz force F is given by

$$F = qv \times B = qv \sin\theta B = qvB \tag{2.4}$$

where q is the charge of the particle, v is the velocity of the particle, B is the strength of the magnetic field, and $\theta = 90^\circ$ as the velocity of the particle is perpendicular to the magnetic field. We can then model particle's trajectory through the magnetic field as a uniform circular motion with a centripetal force

$$F = ma = \frac{mv^2}{\rho} \tag{2.5}$$

where ρ again is the radius of curvature. By equating the Lorentz and centripetal forces (Eqns. 2.4 and 2.5), we find

$$qvB = \frac{mv^2}{\rho} \tag{2.6}$$

Further, we rearrange Eqn. 2.6 and use the definition of average velocity $v = d/t$ (distance d over time t) to find that

$$\frac{B\rho}{d}t = \frac{m}{q} = \frac{A}{q} \tag{2.7}$$

where the mass-charge ratio of a species with total nucleons $A = N+Z$ and charge q (not necessarily equal to Z due to charge states from incomplete stripping of electrons) is directly proportional to the time-of-flight (TOF) t since, for practical purposes, the ratio $\frac{B\rho}{d}$ is assumed constant. Using Eqn. 2.7 we exploit the E1-XFP and E1-OBJ time differences to resolve the isotones composing the secondary beam by plotting the time differences between each scintillator and E1 in arbitrary time units, as displayed in Fig. 3.2.

2.3.2 Cathode Readout Drift Chambers

While we have glossed over exactly how the ion trajectory is determined, in this section we will explain this process as we move our discussion to the focal plane of the S800 as depicted in Fig. 2.6. In the focal plane a set of two Cathode Readout Drift Chambers (CRDCs) are utilized to determine each ion's trajectory on an event-by-event basis. A transformation matrix is the applied to each ion's trajectory as determined by the CRDCs which maps the ion's path back through the two dipole magnets (D1 and D2 in Fig. 2.5) to the TRIPLEX target position. In this manner we are able to determine the ion's trajectory and position at the TRIPLEX target, which is essential information for the Doppler-shift energy reconstruction as it is a function of the angle of gamma-ray emittance with respect to the ion's trajectory, which will also be covered in Sect. 2.4.

Located at the focal plane of the S800 spectrograph (Fig. 2.6) are a series of detector stations which provide crucial information for the particle identification process. After passing through the S800, both the unreacted secondary beam ions and the reaction products created from interactions between the secondary beam and the TRIPLEX target are guided through the series of dipoles (D1 and D2 in Fig. 2.5) and are transmitted to the focal plane detectors pictured in Fig. 2.6. The first set of detectors that the beam encounters are a pair of Cathode Readout Drift Chambers which provide each ion's trajectory on an event-by-event basis. The pair of CRDCs will hereafter be referred to as "CRDC1" and "CRDC2", where CRDC1 provides an ion's first interaction point (X1,Y1) along its trajectory in the focal plane while CRDC2 provides the second interaction point (X2,Y2), as depicted in Fig. 2.7. Simply stated, by using these two interaction points we can determine an ion's vector in the focal plane. A transformation matrix referred to as the "inverse map" can then

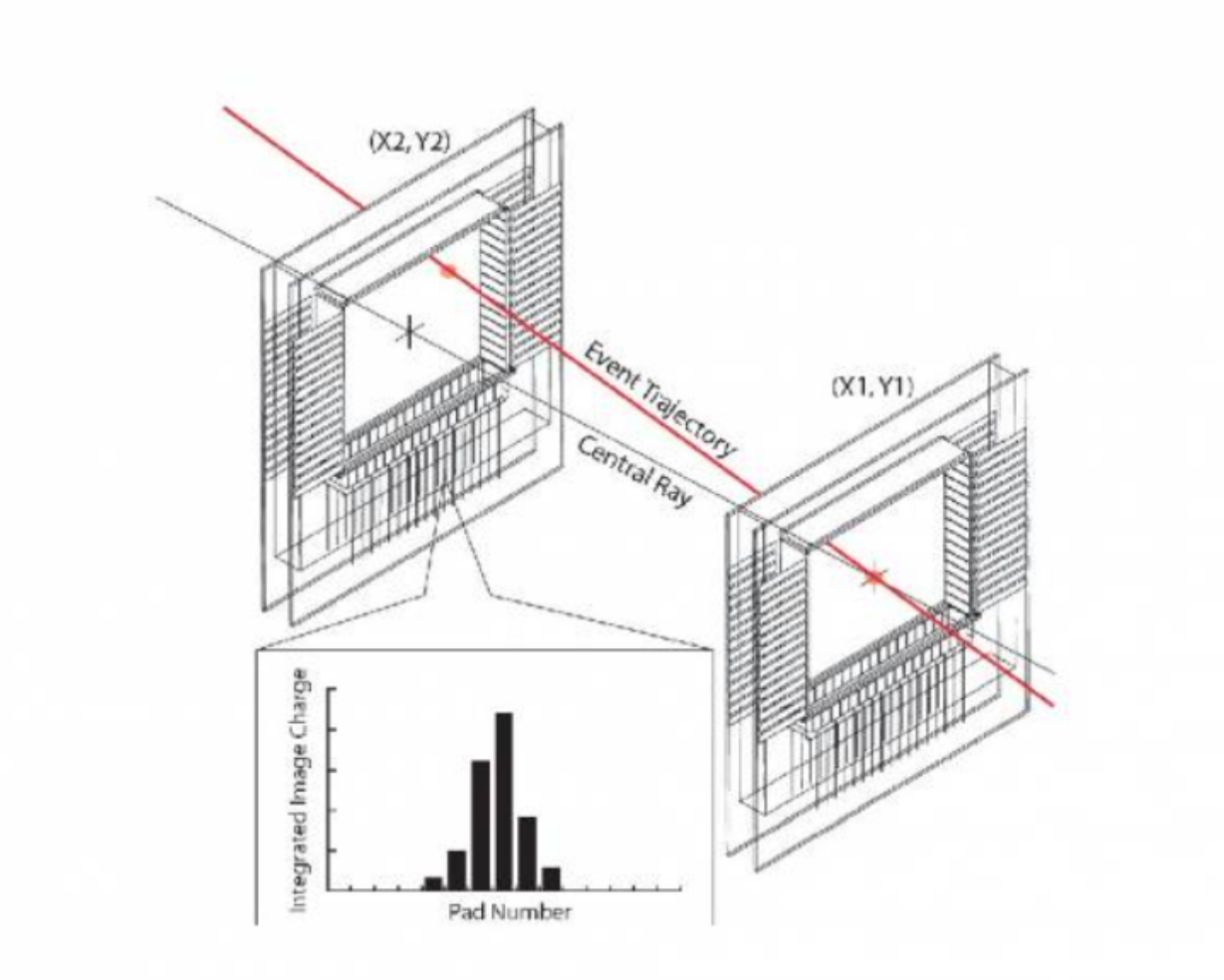

Figure 2.7 Cathode Readout Drift Chambers (CRDCs) at the focal plane of the S800. The two interaction points (X1,Y1) and (X2,Y2) determine the ion trajectory in the focal plane. Beam ions and recoil nuclei ionize gas in the CRDC chambers, the ionized electrons are collected by multiple anode wires, the charge on the anodes induces an opposite charge on the cathode pads. The ion's position in the dispersive plane (X) is determined by a Gaussian fit to the charge distribution across the cathode pads (inset) on an event-by-event basis. The drift time of the ionized electrons to each anode wire is determined with respect to the E1 trigger signal and provides the ion position in the non-dispersive plane (Y). The figure has been adopted from Ref. [71].

be applied to each ion's vector to determine the ion's trajectory backward from the focal plane, through the dipoles, and back to the TRIPLEX target location. Knowing the ion's trajectory at the TRIPLEX target position is essential for event-by-event Doppler-shift correction as the ion-frame energy is a function of angle θ between the ion's trajectory and the direction of the gamma-ray emission as determined by the main interaction point in the GRETINA detector.

Each CRDC is composed of an anode frame upon which the anode wires are mounted. The

anode frame is immersed in a carbon tetrafluoride gas which acts as the ionizing medium. Each anode provides an electric potential to which the ionized electrons will migrate accordingly. Along their paths to the anode, the electric field becomes stronger and the ionized electrons move with a greater velocity causing ionization of more gas molecules along the way and creating an avalanche effect which produces enough electrons to create a measurable charge on each anode. When charge is collected on an anode wire an image charge is induced on the cathode pads located in front of and behind of each wire. The induced charge from each pad can then be collected and the charge distribution across multiple pads (inset Fig. 2.7) can be fitted with a Gaussian function to find the mean position of greatest charge collection. The mean of the induced-charge distribution on the cathode pads provides the ion position (commonly referred to as x_{fp}) in the dispersive plane (X). Simultaneously, the drift time of ionized electrons to the anode wire is determined with respect to the E1 trigger signal, this drift time provides the ion position in the non-dispersive plane (Y) and is commonly referred to as y_{fp}.

After determining an initial position (X1,Y1) from CRDC1, the ion then travels to CRDC2 where the same principles are used to determine a second position approximately 1 m further along the focal plane. Having two position values spatially separated along the ion's trajectory allows us to calculate the ion's vector with respect to the central beam axis (z). From the second interaction point (X2,Y2) we can determine the ion's angle in the dispersive plane a_{fp} and the angle in the non-dispersive plane b_{fp}, both of which are calculated relative to the z-axis.

Given the ion's trajectory as determined by the pair of CRDCs, we can then use the ion's identity (e.g., ^{39}Ca for the main focus of this experiment), the S800 dipole magnet settings in Tesla-meters, and the TRIPLEX target position relative to the S800 pivot point to calculate the inverse map. The inverse map is a transformation matrix that is applied to the ion's trajectory vector in the S800 focal plane which provides the ion's trajectory at the TRIPLEX target position. The trajectory at the target position is commonly defined by a_{ta} (the ion's angle in the dispersive plane x with respect to the ion-of-interest's central trajectory z), b_{ta} (the angle in the non-dispersive plane relative to z), and y_{ta} (the position in the non-dispersive plane relative to z). Further, the kinetic energy and,

hence, the ion's momentum, can also be determined by the magnet settings and the position of the ion in the dispersive plane at the S800 focal plane. The energy difference with respect to the central value set for the ion of interest based on the S800 rigidity provides a distribution commonly referred to as d_{ta}.

The combined information from a_{ta}, b_{ta}, y_{ta}, and d_{ta} are used to characterize the beam at the target location. This characterization of the beam provides crucial information for the G4Lifetime simulation, which requires a realistic beam profile (trajectory and energy) to reproduce the reaction mechanisms and excited reaction products that provide the simulated gamma-ray spectra.

Of course, the description of the S800 particle identification process has excluded a very important process; that is, the process of identifying recoil nuclei produced in reactions on the TRIPLEX target. In the next section, we will discuss identification of recoil nuclei produced in the TRIPLEX target via a combined use of the ion chamber and OBJ scintillator.

2.3.3 Ion Chamber

To determine the identity of reaction products produced by interactions between the secondary beam and the TRIPLEX target we now move on to a description of the S800 ion chamber and how it is used in conjunction with the OBJ scintillator to identify the recoil nuclei from which the gamma rays are emitted. The S800 ion chamber, located just before the E1 scintillator and depicted in Fig. 2.6, serves to identify the atomic number Z of the recoil nuclei by measuring energy loss through a gaseous medium composed of 90% argon and 10% methane.

Contrary to its name, the S800 ion chamber is actually a series of 16 parallel-plate ion chambers, as depicted in Fig. 2.8. Each chamber is composed of a pair of anode and cathode plates with a gas-filled gap between each plate. As heavy nuclei travel through the ion chamber medium the heavier, more energetic nuclei interact with the ion chamber gas and transfer a portion of their kinetic energy to the gas atoms, ionizing the gas and sending electrons and gas ions toward the anodes and cathodes, respectively. When the electrons and gas ions reach the anodes and cathodes a change in voltage is observed and recorded. The heavier beam nuclei lose energy proportional to their atomic number squared (Z^2) as per the Bethe-Bloch relation discussed briefly in section

Figure 2.8 Unhoused view of the ion chamber at the focal plane of the S800. 16 parallel-plate ion chambers are stacked perpendicular to the beam axis (left to right) and cover an active area of $\approx 30 \times 60$ cm. When housed, the chamber contains a mixture of 90% argon 10% methane, typically at a pressure of 300 torr. The picture has been adopted from Ref. [71].

2.2.1. The use of multiple chambers reduces electronic noise by averaging the energy loss over the 16 chambers.

The ion chamber alone is not enough to identify the dozens of recoil nuclei produced in reactions on the target because many isotopes of the same Z may be produced in these reactions. Therefore, another channel of information must be utilized to distinguish isotopes of the same atomic number, in this case the time difference between the E1 and OBJ scintillators is utilized. Though all the unreacted secondary beam ions of the same species will travel through the S800 with similar time signatures, once those secondary beam nuclei interact with the target and produce reaction products with various A/Z ratios the time differences from the OBJ scintillator to the E1 scintillator will be changed. By gating on a particular secondary beam in the data analysis phase (our incoming beam gate), we can observe all events associated with that beam as determined on an event-by-event basis by the OBJ timestamp and energy loss through the ion chamber. Due to energy loss from the reaction mechanism and interactions with the target medium, each reaction product will have a unique trajectory through the S800 dipoles and, thus, a unique TOF through the S800. Therefore, to identify reaction products from a specific secondary beam we plot energy loss in the ion chamber as a function of time difference between the E1 and OBJ scintillators, as shown in Fig. 2.9.

By examining Fig. 2.9 we can discern most of the reaction products from general principles. The central column of nuclei all have similar time signatures because $A/Z = 2$ for all $N = Z$ nuclei. Isotopes of a given Z have different times-of-flight due the difference in their mass-charge ratio, thus we observe that heaver isotopes have longer (more negative) TOF and lighter isotopes having shorter (less negative) TOF, as can be seen by the two calcium isotopes labeled in the figure. Using these principles and the knowledge of the intensity of the incoming secondary beam we can identify one nucleus along $N = Z$ and then follow the pattern to identify all the isotopes of that nuclei by their unique TOFs and isotones by their unique energy loss. Further confirmation of particle identification can come from gating on a suspected known nucleus and examining the gamma rays associated with that "blob"; if the gamma ray energies from decays of that particular nuclei and excited state are known, the spectrum in question can be compared to known data for

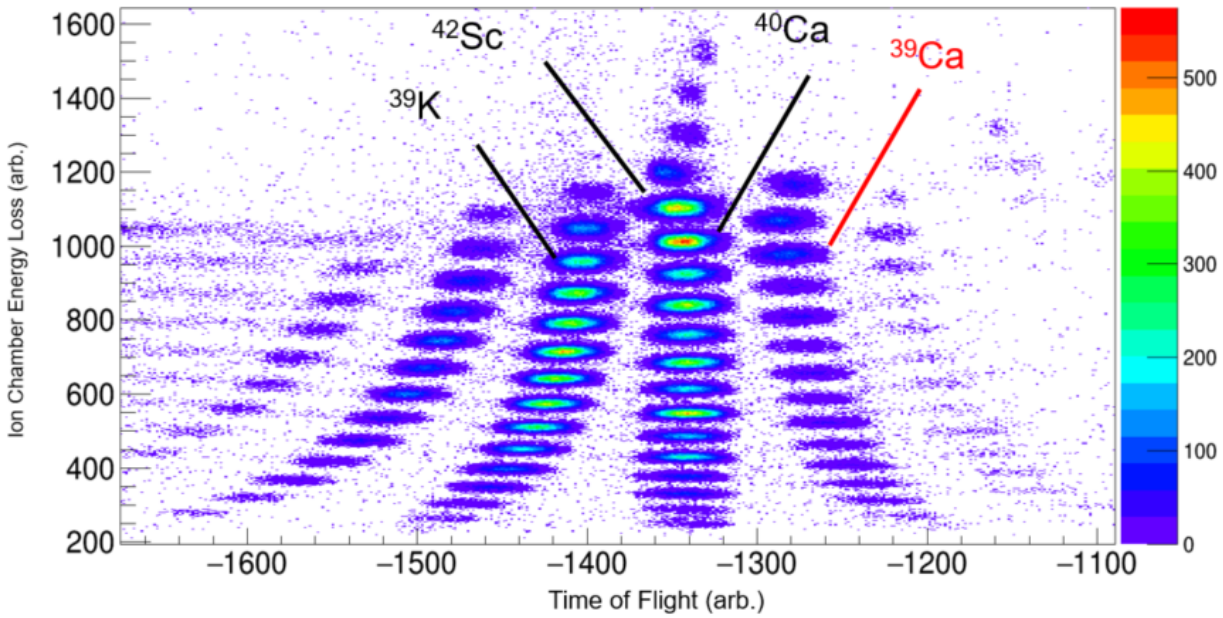

Figure 2.9 Energy loss in the S800 ion chamber as a function of time-of-flight between the E1 and OBJ scintillators. The energy loss vs TOF method is used to distinguish recoil nuclei from reactions between our choice of incoming secondary beam (in this case ^{42}Sc) and outgoing reaction products.

confirmation. In this work all of the above methods were used to confidently identify the reaction products labeled in the particle identification plot in Fig. 2.9.

Now that we understand the principals involved in primary beam production, secondary beam fragmentation, and particle identification we will move to the area of the experimental vault where GRETINA detects gamma rays emitted by nuclei in excited states which have been produced in reactions between the secondary beam and the TRIPLEX target.

2.4 Gamma Ray Spectroscopy

When secondary beam nuclei interact with target nuclei, kinetic energy is transferred to the nucleons and places them in an energetic state. The nucleus sheds this energy by de-exciting from a higher energy state to a lower state and emitting a gamma-ray photon. The energy of the emitted gamma ray is equal to the difference in energy of the initial and final states of the nucleus.

To determine the energy of a gamma ray emitted by an in-flight nucleus, the TRIPLEX target is surrounded by 12 GRETINA detector modules. A single detector module consists of 4 high-purity germanium (HPGe) crystals which are semiconductors that produce electron-hole pairs

when an energetic particle interacts with the detector medium. A high voltage is applied across the medium that provides an electric potential which guides the electron-hole pairs to the electrodes for collection. The charge collected by the electrodes is sent to a preamplifier and converted to a voltage pulse with an amplitude that is proportional to the energy of the gamma-ray. The amplified analog signal is then sent to the GRETINA DAQ where it is digitized. The digital signal is then stored by the NSCLDAQ as an event with a timestamp and an associated energy.

There are three common interactions between the gamma ray and the detector medium which can produce the electric signal: photoelectric absorption, Compton scattering, and pair production [67, 68]. Only photoelectric absorption will generate a voltage signal of amplitude proportional to the full gamma-ray energy. In the case of Compton scattering and pair production, if all the interactions occur within the detector medium the partial signals can be summed in order to obtain a voltage signal proportional to the full gamma-ray energy.

In the process of photoelectric absorption, the energy of the gamma ray is completely transferred to an atom of the medium material. This transfer of energy results in the ionization of an atomic electron which is ejected from the medium atom with an energy equal to the gamma ray energy minus the binding energy of the atomic electron. The highly energetic free electron is then collected by the electrode with a signal amplitude proportional to the original gamma-ray energy. Photoelectric absorption is the most common interaction type for gamma rays of energy lower than a couple hundred keV and the process can be enhanced by using a detector medium of high Z.

For gamma rays of energy ranging from a couple hundred keV to several MeV, Compton scattering is the most typical interaction type leading to gamma ray detection. In the process of Compton scattering, a gamma-ray photon interacts directly with an atomic electron and transfers part of its energy to this recoil electron while continuing along a diverted trajectory. The energy transferred to the recoil electron is a function of the scattering angle and, thus, the photon can transfer a very small fraction or a large fraction of its energy to the electron depending on the scattering angle. The scattered gamma ray can then transfer any remaining energy to other recoil electrons in a series of scattering events and those electrons can be collected at the anode where

the voltage amplitude is again proportional to the gamma ray energy.

When the energy of a gamma ray exceeds 1.02 MeV (twice the electron rest mass) the process of pair production becomes a possible interaction type with the probability of this interaction increasing with increased gamma-ray energy beyond the stated threshold. In the process of pair production, a sufficiently energetic gamma ray interacts with the Coulomb field of a nucleus and is converted into an electron-positron pair where the energy exceeding the threshold is converted to kinetic energy which is shared by the electron and positron. The electron from this process will be transferred toward the anode. The positron will be directed toward the cathode but will likely interact with an electron and induce an electron-positron annihilation which will result in the creation of two more photons. These photons, having conserved the energy of the annihilation pair, can then proceed to interact again via the three processes discussed here until all the energy of the initial incoming gamma ray has been converted to electrons that have been collected by the anodes.

When the processes are not contained to the detector volume, and only a fraction of the gamma-ray energy is collected by the detector before the photon escapes the detector volume, various structures may appear in the gamma-ray spectrum such as the Compton continuum, back scatter peaks, and escape peaks. Therefore, detectors with high Z and large volume are preferred to increase the chances of full-energy deposit within the detector volume, resulting in a full-energy peak. Other techniques such as the addback method can be used in the data analysis phase to gather a full energy peak from gamma rays which were scattered through multiple crystals or crystal segments.

The experiment discussed in this work utilized the Gamma Ray Energy Tracking In-beam Nuclear Array (GRETINA), pictured in Fig. 2.10, a multi-segmented HPGe gamma-ray detector array which surrounds the TRIPLEX target and collects gamma rays for analysis. In the following section we will delve into the specifics of the GRETINA configuration used in this experiment.

2.4.1 Gamma-Ray Energy Tracking In-beam Nuclear Array

The Gamma Ray Energy Tracking In-beam Nuclear Array (GRETINA) [58] is a device composed of HPGe semiconductor detectors used in this work to detect gamma rays and determine

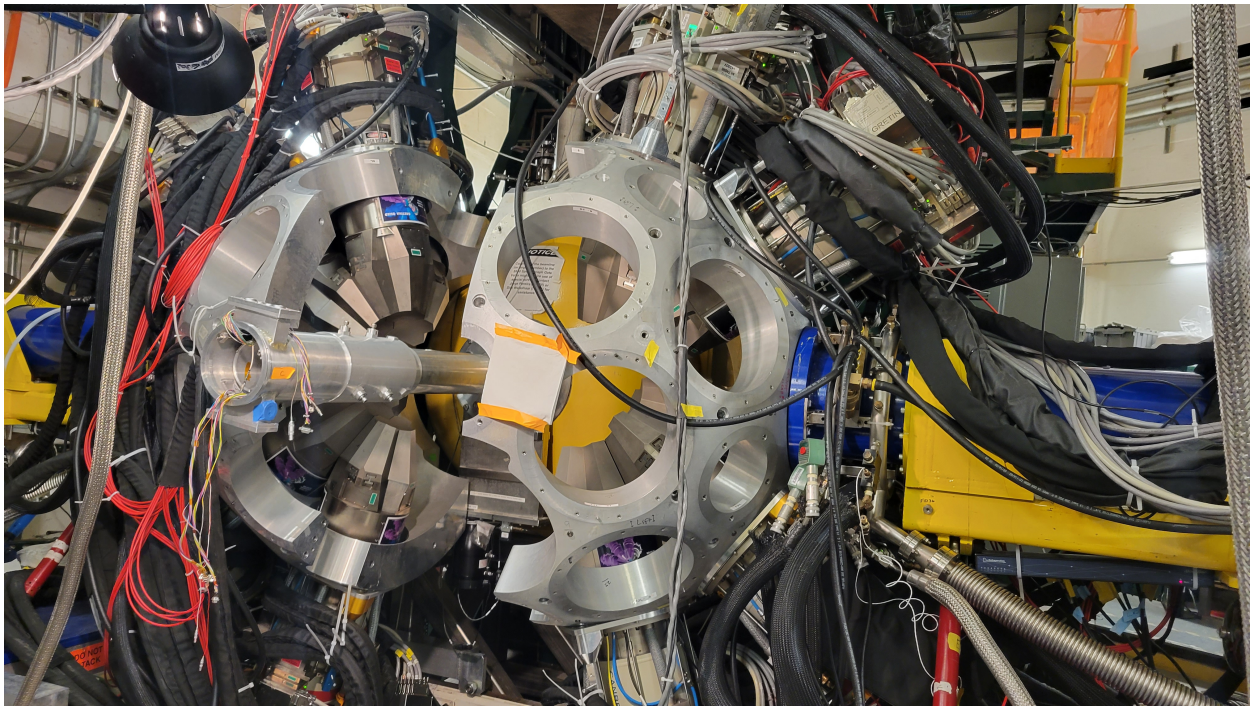

Figure 2.10 The Gamma-Ray Energy Tracking In-beam Nuclear Array with 12 modules positioned for perpendicular and forward focused detection. The module frame has been opened to allow connection of the TRIPLEX beam pipe to the S800 and alignment of the target with the beam spot. The secondary beam moves left to right and interacts with the TRIPLEX target which is located 13 cm upstream from the center of GRETINA. The beam then continues through the S800 for particle identification.

their energy. GRETINA, for this experiment, consisted of 12 detector modules (Fig. 2.11), each containing four hexagonal HPGe crystals, with each crystal consisting of 36 segments (Fig. 2.12). Each crystal has 37 contacts; a central contact which measures the total energy collected from interactions in all segments, and 36 outer contacts corresponding (to the 36 segments) which provide position information with the aid of a signal decomposition algorithm. The signal decomposition algorithm reads signals from the outer contacts and compares them to a library of simulated signals from different locations within each segment to match the real signal to a position provided by comparison to the signal library. Each segment is electrically separated which allows reconstruction of the gamma-ray interaction point(s) to within 2 mm.

Initiated by the E1 trigger, an "event" within GRETINA can be composed of multiple "hits" corresponding to interactions within the detector volume which coincide with a defined time window. Under the main interaction point assumption [59], the interaction point of the largest

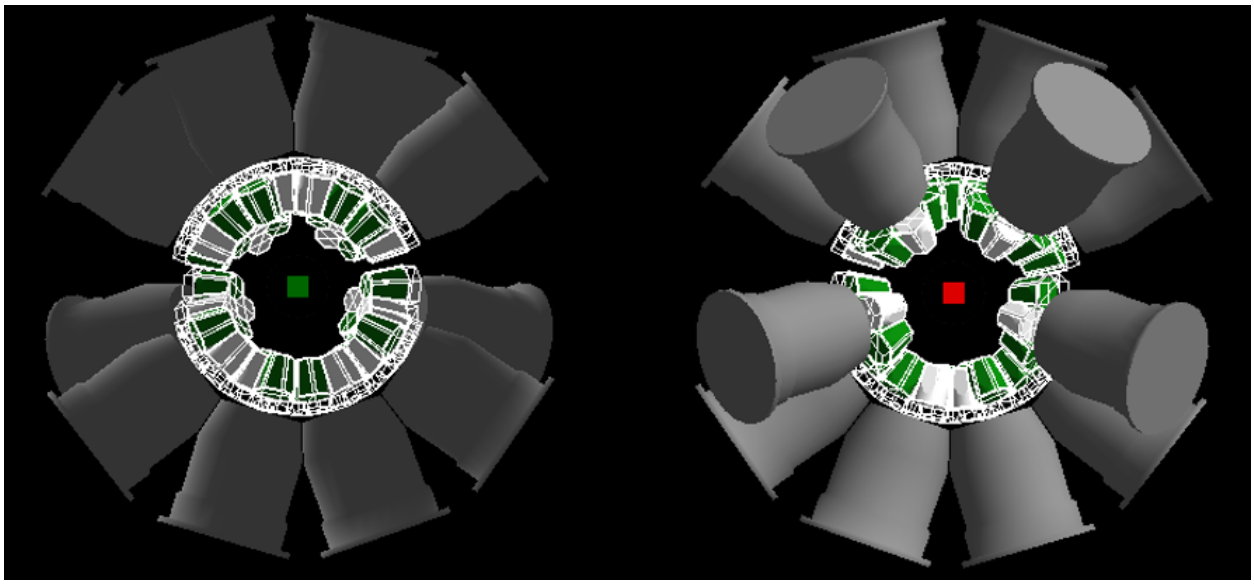

Figure 2.11 Geant4 rendering of the GRETINA module configuration utilized for this work. Each of the 12 GRETINA modules is comprised of a liquid nitrogen cryo-module (grey), 4 hexagonal crystals (green and white representing type A and B), with each crystal having 36-fold segmentation. Looking downstream (left), the beryllium target (green) and the 90° ring of modules are rendered. Looking upstream (right), the tantalum degrader (red) and the forward facing modules are rendered. Not pictured for clarity are TRIPLEX and the beam pipe which accounts for the uncovered area between 0 and 20 degrees with respect to the beam axis (into and out of the page).

energy deposit is taken as the first interaction point when multiple hits are registered within the time gate. The position resolution is high enough to allow gamma-ray tracking of multiple interaction points through the detector volume, enabling the addback method to be utilized in the data analysis phase which increases the number of counts in the full-energy peaks by adding the energy of multiple interactions together to create a single full-energy event in the gamma-ray spectrum.

For the current work, 8 quads were mounted in the 90° ring of the GRETINA frame and 4 quads were mounted in the forward focused rings, as shown in Fig. 2.11. The TRIPLEX plunger held the target approximately 13 cm upstream from the center of GRETINA. This configuration of target placement and forward mounted quads was selected to achieve balance between detection efficiency to forward focusing of gamma rays and sensitivity to varying degrees of Doppler shifts caused by different recoil velocities. A trigger signal from the E1 scintillator initiated information collection from the S800 spectrograph detectors and GRETINA. Using the coincidence between

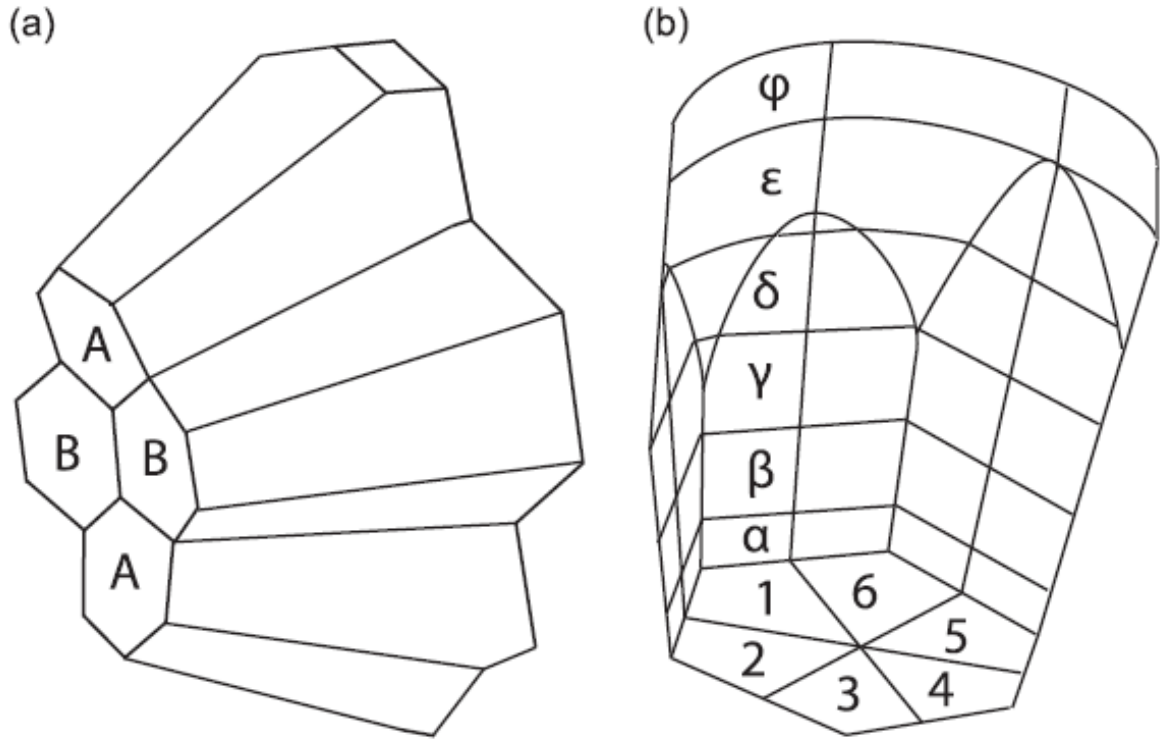

Figure 2.12 Diagram of a GRETINA "quad" (a) and a single crystal segmentation (b) [58]. Each GRETINA module contains a quad of four, closely-packed HPGe crystals (a) with the two pairs of crystals each having unique tapered-hexagonal shapes (A-type and B-type) and length of approximately 9 cm and maximum width of 8 cm. The tapered-hexagonal shapes provide maximum detector volume and solid-angle coverage. Each crystal contains a 36-fold segmentation (b) with a central core contact to collect total energy deposited and each segment with an individual outer-surface contact pad to determine interaction location (36 pads per crystal). The segmentation of each crystal allows for interaction position resolution of approximately 2 mm and tracking of gamma-ray interaction points throughout the detector volume [58]. Reprinted from Nuclear Instruments and Methods in Physics Research Section A: Accelerators, Spectrometers, Detectors and Associated Equipment, Vol. 709, S. Paschalis *et al.*,The performance of the gamma-ray energy tracking in-beam nuclear array GRETINA, Pages No. 44-55, Copyright (2013), with permission from Elsevier.

the S800 and GRETINA allows one to identify gamma ray hits and associate them with a particle event in each of the S800 detectors.

To determine the efficiency of GRETINA, a ^{152}Eu source run was conducted. Gamma rays collected during the source run are matched to adopted energy and intensities I_γ for ^{152}Eu decays. Given the activity of the source at the last measurement A_0, the amount of time since the last measurement t, and the decay constant $\lambda = \frac{ln(2)}{T_{1/2}}$, the activity A of the source at the time of the

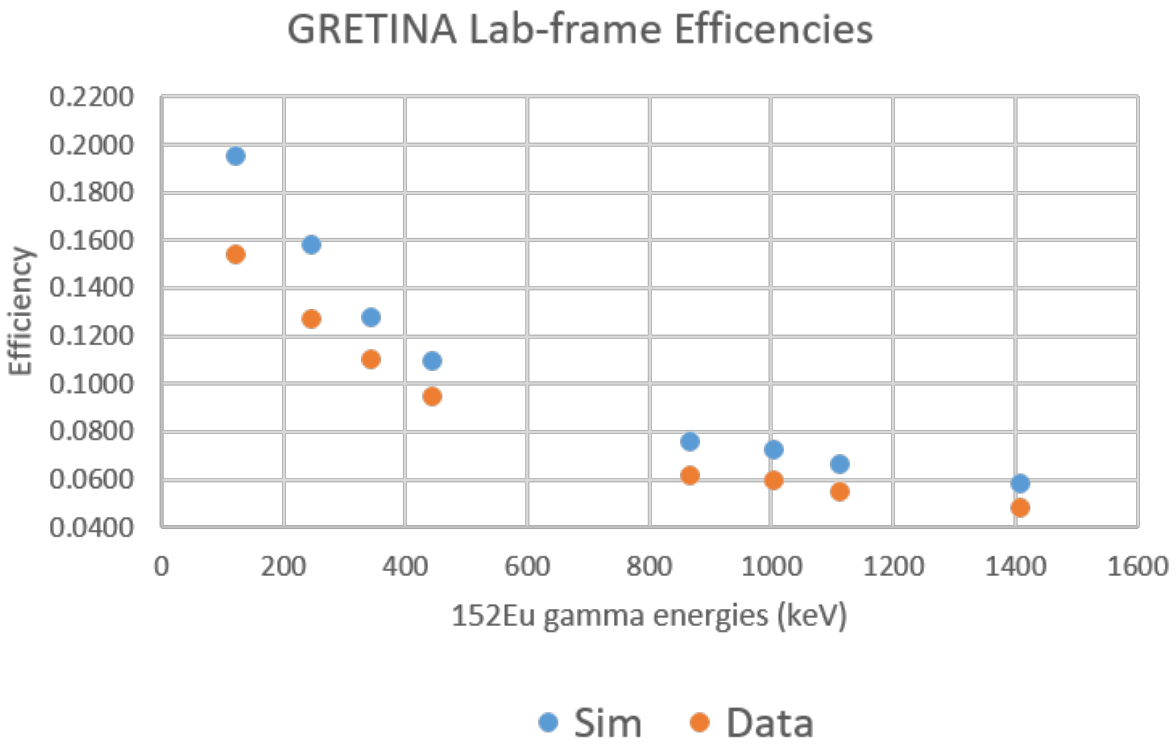

Figure 2.13 The efficiency of GRETINA at the ^{152}Eu gamma-ray energies observed in the lab-frame. The efficiency of the simulation at a given energy is given in blue while the efficiency of GRETINA is given in orange.

source run can be calculated from the radioactive decay equation. From the calculated activity A, the source run duration t_{run}, and the adopted intensities of each of the gamma rays detected, the number of gamma rays emitted from the source is calculated according to $N_{emit} = AI_\gamma t_{run}$. By integrating fits to the observed ^{152}Eu gamma-ray peaks, the number of gamma rays observed N_{obs} by GRETINA within the run time is determined. The experimental efficiency of GRETINA $\epsilon^{exp}_{\beta=0} = \frac{N_{obs}}{N_{emit}}$ in the lab-frame ($\beta = 0$) is then calculated at each gamma-ray energy, as displayed by the orange data points in Fig. 2.13. When the experimental efficiency is compared to the efficiency of a simulated source run $\epsilon^{sim}_{\beta=0} = \frac{N^{sim}_{obs}}{N^{sim}_{run} I_\gamma}$ (blue data points in Fig. 2.13), where N^{sim}_{run} is the number of simulated events, one observes that the simulation overestimates the efficiency of the GRETINA array. Therefore, to determine the experimental ion-frame efficiency $\epsilon^{exp}_{\beta>0}$, we must scale the simulated ion-frame efficiency by a factor of $\frac{\epsilon^{exp}_{\beta=0}}{\epsilon^{sim}_{\beta=0}}$. For this experiment, the simulated ion-frame efficiency was scaled by a factor of 0.84. With the efficiencies determined, the intensities

of each of the ^{39}Ca peaks could be calculated from simulated fits.

GRETINA was utilized to collect gamma rays emitted from ^{39}Ca and ^{39}K recoil nuclei. Because the gamma rays are emitted from ions moving at relativistic velocities (approximately 0.3c) the energies that were determined by GRETINA detectors in the lab frame must be converted to energies that coincide with the ions' rest frame. In the next section we will discuss the Doppler-shift correction on the gamma ray energies detected by GRETINA.

2.4.2 Doppler-Shift Correction

The energies detected by GRETINA must be corrected for the difference in reference frames between the GRETINA detectors in the laboratory frame and gamma rays emitted in the ion frame at relativistic energies. Gamma rays that are emitted from in-flight nuclei with a velocity moving toward an observer will appear to have a shorter wavelength from the perspective of the lab-frame observer while gamma rays emitted from nuclei moving away from the observer will appear to have a longer wavelength. Since the wavelength λ of a photon is inversely proportional to the energy E of the photon according to $E = \frac{hc}{\lambda}$, it is essential that the energy detected by GRETINA be Doppler corrected to account for the difference in photon wavelength and, hence, the energy collected by detectors at various angles.

Given the energy detected in the lab-frame by the GRETINA detectors E_{lab}, we can Doppler correct this value to the desired ion-frame energy E_{ion} via

$$E_{ion} = E_{lab}\gamma(1 - \beta\cos\theta) \tag{2.8}$$

where θ is the angle of gamma-ray emittance with respect to the trajectory of the in-flight nuclei, and γ is a function of $\beta = \frac{v}{c}$ defined in section 2.2.1. Therefore, knowledge of the ion velocity v with respect to the lab-frame and the angle of emittance θ is essential for determining the ion-frame energy of the gamma ray.

As shown in Eqn. 2.2, the velocity v can be obtained from the rigidity settings of the S800 dipoles and the angle of emittance θ can be obtained from the main interaction point within the GRETINA crystal. In practice, the uncertainty associated with v and θ result in an uncertainty in the determination of the ion-frame energy known as Doppler broadening. This uncertainty

expresses itself in a broadening the full-energy gamma-ray peak in the ion-frame energy spectrum. An example of a source of uncertainty in ν is the assumption of reaction location in the target, which affects the amount of differential energy loss and hence the velocity of the outgoing particle since a ^{42}Sc secondary beam particle of $Z = 21$ loses more energy than a $Z = 20$ calcium isotope; therefore, correcting data with a β which assumes a reaction in the middle of the target may introduce error to the energy measurement. Along similar lines, the location of gamma-ray emission may also affect the ion-frame energy spectrum; if the gamma was emitted from inside the target due to a short lifetime or was emitted further past the target than TRIPLEX was configured for (due to a long lifetime) the gamma-ray peak may have a high or low energy tail in the ion-frame energy spectrum, respectively. Sources of uncertainty in θ may arise from the position resolution of GRETINA, incorrect determination of the main interaction point, and incomplete knowledge of the ion trajectory at the target position.

Despite the uncertainties listed above, we are able to constrain the parameters to obtain a spectrum with sufficient resolution to utilize the recoil-distance method (RDM) for lifetime measurement. In the following section we will move to the target station of the S800 where TRIPLEX holds the secondary reaction target and the velocity degrader. We will describe the TRIPLEX configurations utilized in this experiment and see how the recoil distance method is utilized to determine the lifetimes of excited states.

2.5 RDM Lifetime Measurement with TRIPLEX

At the target station of the S800 the TRIple PLunger for EXotic beams (TRIPLEX) is positioned in the beam line. As the secondary beam approaches TRIPLEX it first encounters a 2-mm thick beryllium-9 target. Reactions on this target produce nuclei in excited states which travel some distance before decaying by gamma-ray emission according to the lifetime of the excited state. The resultant recoil nuclei then encounter a 0.13 mm stable-tantalum degrader before entering the S800 dipole magnetic fields and continuing on to the focal plane for particle identification.

Depending on the lifetime of the excited state, the recoil nuclei may decay before or after losing velocity in the tantalum degrader, thus gamma rays may be emitted from nuclei with a velocity

β_1 which is "fast", having not been slowed by the degrader, or with a "slow" velocity β_2, having lost energy and velocity to the tantalum degrader. When we Doppler correct the data for a single β value, the resultant spectrum will show two peaks for a single transition; one peak at the true ion-frame energy of the gamma ray and one peak that has been over or under corrected by the choice of β. The relative intensities of these two peaks as a function of target-degrader separation distance provides the data necessary to measure the lifetime of the excited state. In this section we will briefly describe the basic operating principles of TRIPLEX, the settings used in this experiment, and the recoil distance method for lifetime measurements.

2.5.1 TRIPLEX Design and Operation

The differential plunger device is, in essence, a target and degrader or stopper mount with a precision distance-measurement system. Differential plunger devices have been employed at laboratories around the world for various measurements. The Differential-Plunger for lifetime measurements of tagged Unbound Nuclear States (DPUNS) [73] was designed to measure lifetimes of unbound states and deformations. The TIGRESS Integrated Plunger device (TIP) [74] has been utilized at TRIUMF [75] to determine electromagnetic transition rates via lifetime and low-energy Coulomb excitation measurements. The Triple-foil differential Plunger for Exotic Nuclei (TPEN) [76] was developed to measure excited state lifetimes with small cross sections. The charge plunger device [77] has been designed to work with the MARA mass separator [78] to determine lifetimes by detection of charge-state distribution of recoil nuclei. The Cologne Compact Differential Plunger (CoCoDiff) [79] has been compactly designed to work with many different spectrometers and detectors and to be sensitive to two regions of lifetimes simultaneously. The TRIple PLunger for EXotic beams has been used with both the GRETINA and SeGA [80] gamma-ray detectors to measure excited state lifetimes and cross sections using fast beams of rare isotopes.

TRIPLEX allows multiple targets to be mounted at various distances to conduct recoil-distance measurements for excited states with lifetimes ranging from hundreds to tens of picoseconds. The cylindrical shape of TRIPLEX allows it to be mounted inside a custom beam pipe which provides feed-through connections from the TRIPLEX motors and conductance wires to the electronics

stack outside the beam line and finally to a computer dedicated to TRIPLEX operation. The main components of TRIPLEX are three coaxial tubes separated by bearings to allow motion with minimal friction and the motors that move the inner and outer tubes. Each tube is attached to a ring upon which the target, degrader, and second degrader cones are mounted, with the target, degrader, second degrader being mounted on their respective cones. The central tube remains stationary and holds the first degrader ring upon which the first degrader cone is mounted. The inner tube is connected to a precision motor which can move the target toward and away from the first degrader. The outer tube holds the second degrader and is also connected to a precision motor that can move the second degrader toward or away from the first degrader.

The distance between the target and degrader is measured by capacitance between the two materials as the capacitance is inversely proportional to the distance between the plates. Great effort is expended to ensure that the target and degraders are mounted parallel to each other so as to model the system as a parallel plate capacitor. To determine the separation distance, a pulsed charge is sent to the first degrader by a pulse generator in the electronics crate; the charge on the first degrader induces an image charge on the target or second degrader which creates an electric field which can be measured as a voltage difference. The electronics crate amplifies and shapes the induced voltage signal received from the plunger and sends the signal to a multi-channel analyzer which, in turn, transmits the signal to a computer that displays motor position and voltage and provides a control panel through which to send movement commands to the plunger. TRIPLEX also benefits from a second measurement system called the TESA [81], which relies on a mechanism similar to a ball and spring interaction to determine position differences down to a tenth of a micron.

The position of the target and second degrader relative to their start points can be displayed in the TRIPLEX LabVIEW GUI, but the absolute separation distance must be calculated from the electrical contact position between plates, the relative distance the target has been moved away from the contact position, and the voltage at each target position. When the motor reading, TESA reading, and the voltage measurements are all calibrated sufficiently the position of the target or second degrader with respect to the stationary first degrader can be determined to within tens of

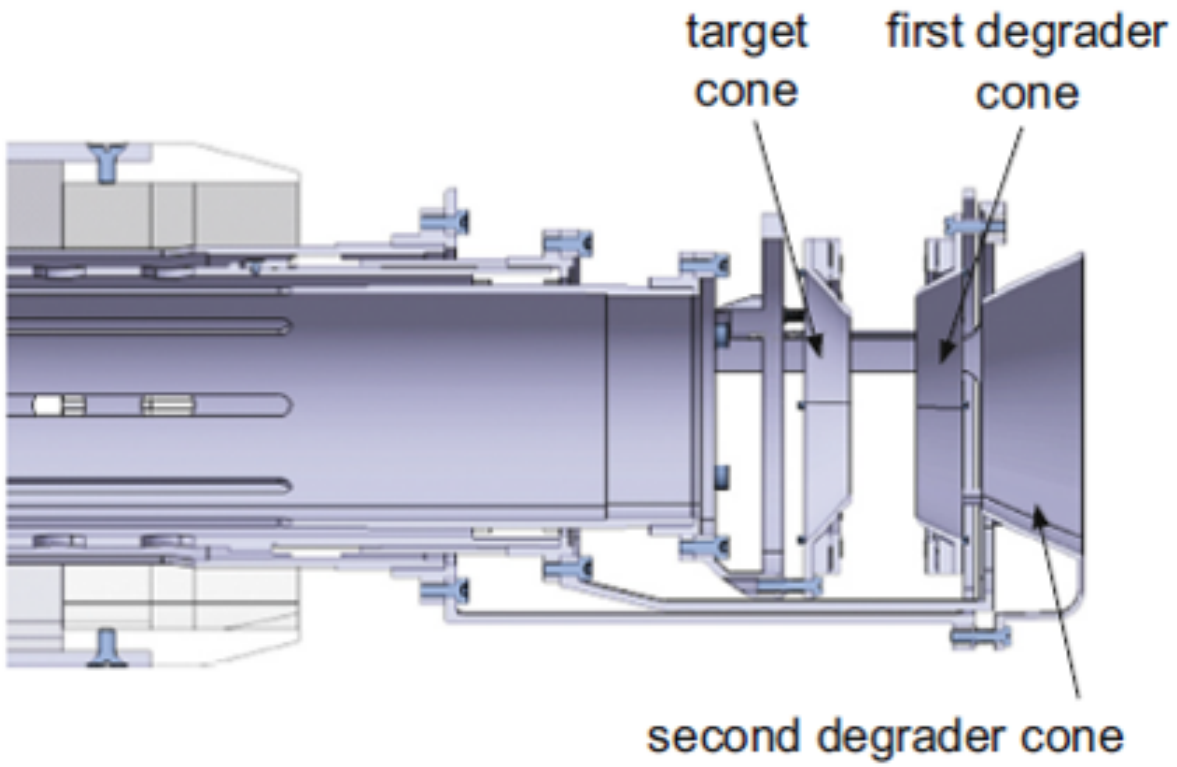

Figure 2.14 Diagram of the TRIple PLunger for EXotic beams [57]. TRIPLEX is designed to hold a production target and two degraders. In this diagram, the secondary beam enters from the left then interacts with a ^{9}Be target mounted on the target cone which can be moved toward or away from the stationary first degrader cone to allow measurement of lifetimes generally the 10s of picoseconds. Although TRIPLEX can hold a second degrader in the secondary degrader cone, the second degrader was not required for this experiment but the second degrader cone held a stripper foil to increase the number of fully stripped ions. Reprinted from Nuclear Instruments and Methods in Physics Research Section A: Accelerators, Spectrometers, Detectors and Associated Equipment, Vol. 806, H. Iwasaki *et al.*, The TRIple PLunger for EXotic beams TRIPLEX for excited-state lifetime measurement studies on rare isotopes, Pages No.123-131, Copyright (2016), with permission from Elsevier.

microns. This precision reduces systematic error resulting from uncertainty in the target-degrader separation distance.

Once the target position has been calibrated, the TRIPLEX plunger uses the voltage readings to maintain a constant distance setting by utilization of the feedback system. Using distance measurements and voltage readings, LabVIEW operational software plots this data and a fit of the data points is used by the feedback system to convert the voltage reading at any given moment into a distance reading. When TRIPLEX is used in feedback mode, the software will automatically adjust and maintain a separation distance defined by the plunger operator. The feedback system is

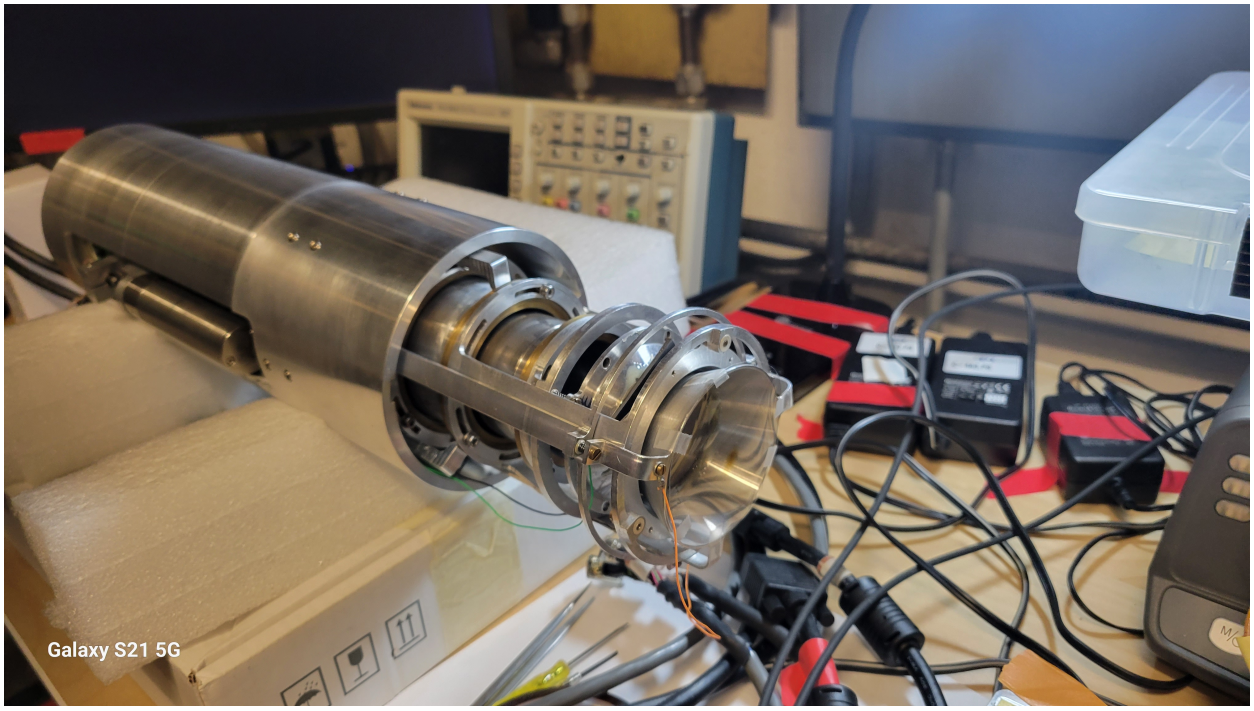

Figure 2.15 Full view of the TRIple PLunger for EXotic beams [57]. The secondary beam enters TRIPLEX from the back (left) and interacts with the target and degraders (right). The outer-most cylindrical housing protects motor control electronics and the TESA precision distance measurement system. A target motor is displayed on the left (small cylinder parallel with housing), this motor moves the inner cylinder which connects to the target ring.

necessary to maintain continual confirmation of the target position and correct any deviance from the user-defined location by automatically moving the target motors to maintain a constant voltage.

2.5.2 TRIPLEX Experimental Configurations

For gamma-ray energy and efficiency calibrations, a 2-mm thick ^{9}Be production target was mounted to the target cone of TRIPLEX and moved to the position where the stationary tantalum degrader would normally be located. For energy calibrations, a ^{152}Eu gamma-radiation source was mounted on the downstream face of the target and the TRIPLEX plunger was inserted into the beam pipe so that the target was positioned 13 cm upstream from the center of GRETINA, as discussed in section 2.4.1. GRETINA data was recorded for 60 minutes with the europium source to determine the experimental efficiency of the GRETINA detectors with consideration given to attenuation of gamma rays which are absorbed by the target and aluminum crystal shielding and to account for areas lacking in solid angle detector coverage.

After the source run was completed, the target was dismounted and the beam was sent to the experimental vault so characterization of secondary beam could be performed. The secondary beam rate was measured over the course of two short runs (3 and 5 minutes) where the two runs correspond to two different incoming beam acceptances, $dp/p = 1\%$ and $dp/p = 0.5\%$. These two runs provided important beam properties such as secondary beam energy, ion momentum, and ion trajectory which are essential for producing the most realistic simulation of the incoming beam.

The target was then mounted again, the secondary beam was directed to the experimental vault, and the S800 was tuned for the target-only data runs. The S800 dipoles were tuned to a rigidity of $B\rho = 2.2188$ Tm, which placed the unreacted secondary beam nuclei on a central trajectory through the S800, and two runs were again performed for the two momentum acceptances. This configuration of rigidity settings and beam on target aids in characterizing the target itself as the density of the material cited by the manufacturer may not be uniform; thus, our simulation allows for a scale factor that compensates for discrepancies between the target manufacturer's quoted density and the effective density. This scale factor can be determined by simulating the position distributions (a_{ta}, b_{ta}, y_{ta}) and the energy distribution d_{ta} of the unreacted beam on target, fitting simulations to the data, and adjusting the scale parameter accordingly to achieve reasonable fits. For this target, a scale factor of approximately 0.93 was found to properly reproduce the effective thickness of our target. Two mask calibration runs were performed to calibrate the position readings from CRDCs 1 and 2, and a 10 minute background run was conducted to quantify the level and type of environmental background radiation. With the secondary beam on target, the S800 magnets were re-tuned to center on the reaction products with a rigidity setting of $B\rho = 2.1296$ Tm. Data was then taken in the target-only configuration for approximately 18 hours with coincidence between the S800 and GRETINA triggered by event detection in the E1 scintillator. The target-only runs provided valuable information regarding which excited states were populated during reactions on target and how often they were populated relative to the other states.

Upon completion of the target-only runs, the target was moved 1 mm upstream and the 0.13-mm Ta degrader was mounted to the stationary first-degrader cone. The S800 was re-tuned to center on

the unreacted secondary beam with rigidity of $B\rho = 1.9578$ Tm and two short runs were taken with the two incoming-beam acceptance settings. These unreacted beam runs provide the information necessary to characterize the tantalum degrader in the same manner described above for the target. The S800 dipoles were then tuned to $B\rho = 1.8577$ Tm to center on the reaction products and data was taken with the target-degrader separation distance of 1 mm for approximately 2 days. This two-foil data-collection period resulted in the gamma-ray spectrums shown in the Data Analysis chapter and provide data essential for the recoil-distance lifetime measurement.

Finally, the target was moved downstream toward the first degrader to take the 0-mm separation data. The S800 settings were maintained from the 1-mm configuration as the energy loss remains unchanged when no other components are added to the system. The 0-mm separation was maintained by the feedback system and data was taken for approximately 2 days in this configuration. The second configuration is essential for the recoil distance lifetime method as this method relies on the relative change in peak intensities as a function of separation distance. The short separation distance also allows for measurement of faster lived states, though for this work, those states primarily decayed within the thick production target.

Reactions on target for all target and target-degrader configurations produced ^{39}Ca and ^{39}K in excited states. When these nuclei de-excite by gamma-ray emission the resultant gamma-rays are detected by GRETINA. In the next section we will describe how the relative intensities of the gamma-ray peaks in a spectrum are used to determine the lifetime of an excited state via the recoil-distance method.

2.5.3 Recoil-Distance Method

The recoil-distance method for lifetime measurements was utilized for this experiment as the target-degrader separation distances were sensitive to the lifetime of the states of interest. As with other types of radioactive decay, the decay of a nucleus by gamma-ray emittance is a spontaneous and probabilistic process which can be described by an exponential decay function. Given some initial number N_0 of a particular species of nuclei in a particular excited state, the number of nuclei

remaining in the excited state N as a function of time t is given by

$$N(t) = N_0 e^{-\frac{t}{\tau}} \tag{2.9}$$

where τ is the mean lifetime of the excited state. The mean lifetime of a state is the time necessary for the number of excited state nuclei to be reduced by a factor of e and is approximately 44% longer than the half-life of a nuclei, a value that is commonly quoted in other fields which measure properties of radioactive nuclei. Of course, the mean lifetime τ can be related to the half-life $T_{1/2}$ of an excited state by $T_{1/2} = \ln(2)\tau$, but mean lifetime is most commonly used in RDM experiments and thus we will restrict our discussion to this value.

The recoil-distance method exploits the exponential nature of the decay process to determine the mean lifetime of an excited state by using the ratio of peak intensities of gamma rays emitted from fast nuclei I_f and slow nuclei I_s according to

$$\frac{I_s}{I_s + I_f} = e^{-\frac{x}{v\tau}} \tag{2.10}$$

where x is the target-degrader separation distance and v is the velocity associated with the slow nuclei (i.e., nuclei which emit gamma rays after losing velocity to the degrader). While this relation is sufficient to describe the decay of a single excited state, when a nucleus decays by a series of emissions from a higher orbital to an orbital multiple levels below (commonly referred to as a "cascade"), the relation becomes more complicated as each state has a unique lifetime which feeds the observed lifetime of the lower states. Rather than repeat what has already been sufficiently described, this author will direct readers to Ref. [82] for a rigorous derivation of the relevant relations. However, Fig. 2.16 provides an illustration of the basic principles underpinning the RDM lifetime measurement with a more intuitive visual description of the relation between fast and slow peak intensities resulting from a single transition.

The 2D-plot in figure 2.16 depicts the relation between the Doppler-corrected energy of the gamma rays (x-axis), the angle of emittance as determined by the main interaction point in GRETINA (y-axis), and the number of gammas rays detected at a particular angle and energy (z-axis). The diagram below the 2D spectrum depicts the relation between gamma-ray energy

and Doppler correction when a single velocity β_2 is used to correct gamma-ray energies from fast (blue) and slow (red) in-flight nuclei. When the secondary beam interacts with the target, a reaction occurs which produces ^{39}Ca* in an excited state (indicated by the asterisk). The recoil nuclei then travel beyond the target, through the degrader, and into the S800 for particle identification. Upon excitation in the target the radioactive decay process begins. Some nuclei will decay before the degrader with a fast velocity β_1, other nuclei will lose energy in the degrader and decay with a slow velocity β_2. Because the nuclei are randomly oriented, each gamma ray will be emitted with a different trajectory with respect to the trajectory of the in-flight nucleus; therefore, GRETINA detects gamma rays from interactions with crystals at all angles covered by the detector configuration (see Fig. 2.10 for a rendering of the solid angle coverage for this experiment).

The detection of gamma rays at a single energy by detectors at all angles can be observed in the 2D plot in Fig. 2.16 as the vertical lines at approximately 1100 keV and 900 keV, these are the gamma rays emitted from the slow nuclei and Doppler corrected with β_2 according to Eqn. 2.8. Meanwhile, gamma rays originating from decays of the same excited state, but emitted before the degrader and Doppler corrected with β_2 (the beta associated with velocity after the degrader), result in counts with under-corrected energy, producing higher energy components at low detector angles. These fast components gradually converge with the straight, properly-corrected gammas at high-angle detectors since the Doppler shift is very small to an observer (or detector) perpendicular to the ion-trajectory. This merging of gamma ray energies in the 2D spectrum at high angles gives a characteristic "chopstick" pattern for gamma rays originating from the same transition, with the same energy, but Doppler corrected with different β. Gamma rays emitted in the lab-frame appear over corrected in the 2D spectrum, the diagonal lines with low energy at low angles and higher energy at high angles are typically the result of laboratory-frame gamma rays where recoil neutrons created by the fragmentation of the secondary beam excite aluminum nuclei in the beam pipe or germanium nuclei in the detector crystals which then emit gamma rays; these gamma rays are commonly referred to as "neutron-induced background" gamma rays. The excitation of the surrounding beam pipe, TRIPLEX components, and germanium nuclei result in

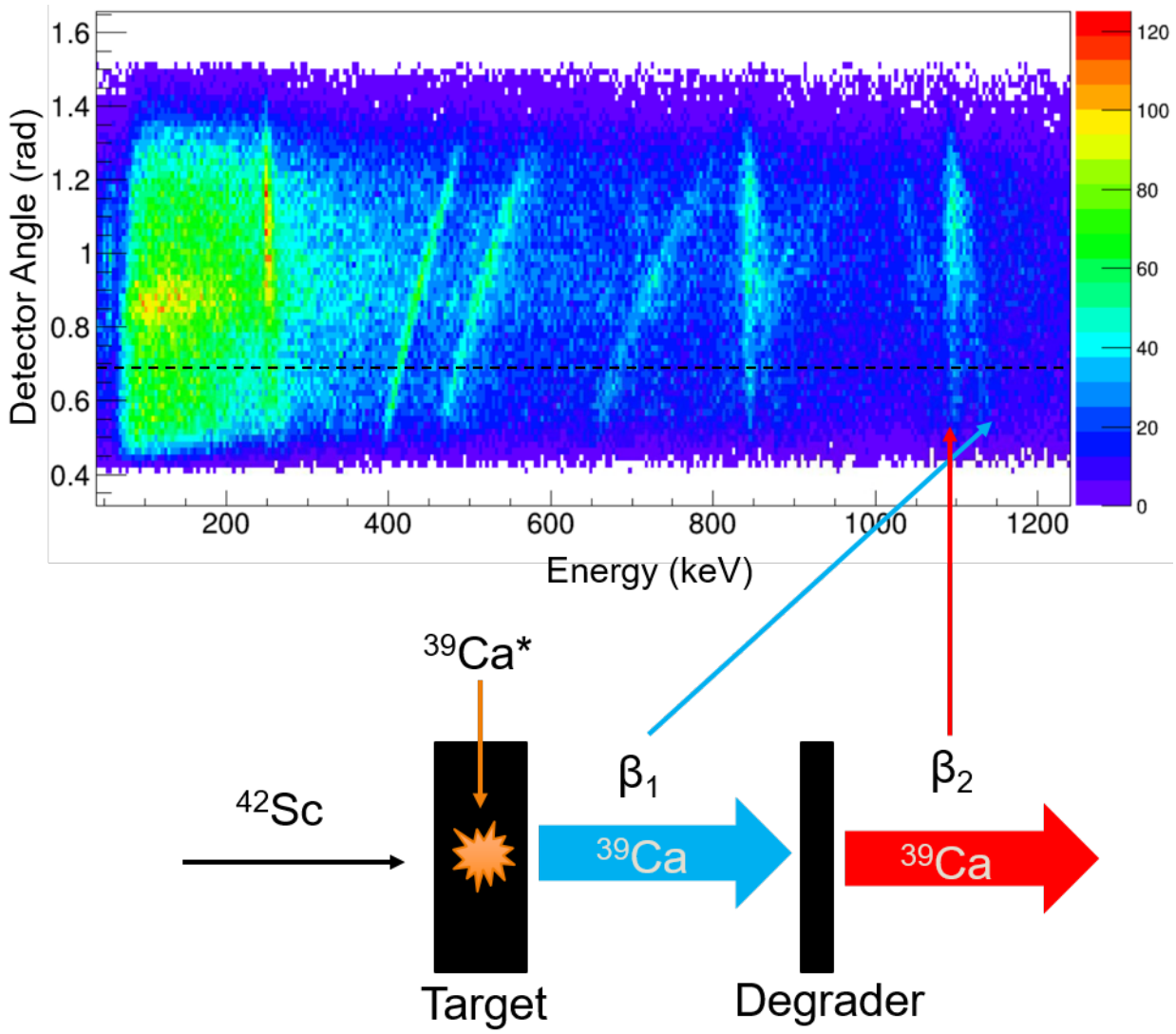

Figure 2.16 The ^{9}Be(^{42}Sc, ^{39}Ca*)X reaction produces nuclei in excited states (denoted by "*"). Gamma rays may be emitted from "fast" nuclei of velocity β_1 or "slow" nuclei of β_2, having been slowed by the degrader. The gamma-ray emittance angle (y-axis) is plotted as a function of the Doppler-corrected gamma-ray energy (x-axis) and the number of counts at a particular angle and energy (z-axis).

gamma rays emitted from stationary nuclei and produce the over-corrected diagonal lines when Doppler corrected with a β associated with in-flight nuclei.

Given the 2D spectrum in Fig. 2.16, we can "cut" the spectrum at a low angle (represented by the dashed line) and project the spectrum onto the x-axis for all events below our cut angle; this projection produces a 1D gamma-ray energy spectrum with counts on the y-axis and gamma-ray energy on the x-axis, as shown in Fig. 3.13. When we make this low-angle projection onto the x-

axis we see a characteristic 2-peak structure for a single gamma ray transition; e.g., the true-energy gamma peak at 1100 keV and the under-corrected peak at 1130 keV in Fig. 3.13. From the 1D gamma-ray spectrum we can then calculate the intensities of the slow peak I_s at 1100 keV and the fast peak I_f at 1130 keV and use Eqn. 2.10 with the separation distance x and the velocity v to solve for the lifetime τ of the excited state. But again, this simple calculation omits important details.

The number of counts observed in each peak includes gamma-ray counts that originated from cascades which fed the state-of-interest, this makes the slow peak appear to have more counts than it would if the all the decays were the result of direct population of the state-of-interest. A nucleus may be excited to a higher-lying state in the target, travel some distance associated with the lifetime of that higher-lying state, emit a gamma ray by de-excitation to the lower-lying state-of-interest, then travel more distance associated with the lifetime of the state-of-interest before finally decaying at some location along its trajectory. The cascade of decays from higher-lying states results in an increase in the intensity of the slow peak, resulting in a calculation of an apparent lifetime which is longer than the actual lifetime of the state-of-interest. Therefore, knowledge of the direct population of all higher-lying states that feed the state-of-interest is crucial for proper utilization of the recoil-distance method for lifetime measurements. This topic will be explored extensively in the Data Analysis section of this work as the states-of-interest which are the focus of this work are fed by two higher-lying states and significant effort was expended to account for feeding effects that contribute to the systematic uncertainty in the lifetime measurements.

In practice, the relevant relations utilized in RDM lifetime measurements are coded into a GEANT4 [83, 84] simulation package which utilizes parameters such as secondary beam characteristics, target-degrader separation distance and material properties, direct population fractions of the excited states in a cascade, and the mean lifetimes of excited states to produce a simulated gamma-ray spectrum. Many of these parameters can be constrained with knowledge of the beam profile, S800 dipole settings, and the position, angle, and energy distributions at the target. Once these parameters are constrained one can focus on the two most important parameters for this work: the lifetimes of the excited states, and the direct population fractions for excited states which feed the

states of interest. The simulation package and the relevant parameters utilized to fit the simulated gamma-ray spectra to the experimental spectra will be discussed further in the following chapter.

CHAPTER 3

DATA ANALYSIS

This chapter describes the analysis of data taken with all plunger settings, including detailed procedures of calibrations, simulations and determination of the lifetimes of interest. The analysis is conducted in three main steps: calibration of the experimental data, the adjustment of parameter sets used in the simulation, and determination of the lifetime of the state of interest by fitting simulations to the experimental data. In the case of the present work, each step was repeated separately for the analysis of ^{39}Ca and again for the analysis of the mirror nucleus ^{39}K.

Within the lifetime analysis phase for each nucleus, the analysis of the both the $11/2^-$ and $9/2^-$ states was performed. The analysis of the $11/2^-$ state lifetime in ^{39}Ca was the primary focus of this work due to its structural similarity to the 2^+ state in ^{38}Ca, while the analysis of the $9/2^-$ state was conducted because the TRIPLEX configuration happened to be sensitive to the lifetime of the $9/2^-$ state. The analysis of the $11/2^-$ state in ^{39}K was performed for two reasons; first, since the lifetime of the state had been measured previously, the current analysis served as a verification of the techniques used to study the lesser known ^{39}Ca state. Secondly, the analysis of the mirror $11/2^- \rightarrow 7/2^-$ transition in ^{39}K provided the opportunity for a self-consistent application of the matrix element decomposition being that the ^{39}Ca analysis provided the proton matrix element while the ^{39}K provided the neutron matrix element.

In the following sections, we will discuss the relevant calibrations of the data and simulations used in this work and then move into the lifetime analysis. Because the analysis spans two states in two nuclei from data taken with three plunger settings, we will attempt to minimize repetitive explanations and keep the majority of the analysis technique descriptions restricted to the ^{39}Ca analysis, unless there was reason for a significant departure in the analysis of the mirror nucleus, in which case, the difference in techniques utilized will be explained when required.

3.1 Experimental Data Calibration

During the experiment, the data collection was monitored using the SpecTcl software package [85]. SpecTcl allows for online viewing of data and limited offline analysis tools. A rough

calibration of the relevant detector data was used during the experimental run time to view a sample of the data taken and ensure that all the devices were working, the device settings were suitable for the experiment, and to make necessary adjustments to the device settings during experimental run time. But the SpecTcl online analysis tool was used only to display a small fraction of the actual number of events that the NSCLDAQ is recording. For a proper analysis of the experimental data, all events must be analyzed and the data must be calibrated to a higher standard to get the most accurate representation of each event. Thus, after the experiment was over, the raw-event data was unpacked and the data from specific devices was corrected for a complete analysis.

When experimental data is collected by the NSCLDAQ, the data is stored in run files with each run file containing a number of events. The events coincide with the S800 triggers and the data collected from all the coincident detectors that were triggered by each event, this data structure allows for event-by-event detail and correction. A C-type library called GrROOT [86] is used to unpack the raw event data, perform corrections to the data based on the device settings, and create histograms from the events. The histograms are displayed in ROOT trees [87] which can then be analyzed. Using the histograms created from raw data from each of the detector components described in the previous section, we calibrated the data to correct for any mismatching of device settings and irregularities to provide the most accurate representation of the secondary beam, the recoil nuclei produced in reactions on the TRIPLEX target, and the gamma-ray events that provide the basis for the lifetime analysis.

In the following sections we will describe the experimental data calibration processes. We will then move the discussion to calibration of our simulation in a similar fashion. Finally, we will explain the lifetime analysis process and results for each of our nuclei of interest.

3.1.1 Scintillator Data Calibration

As described in section 2.3.1, the differences between the E1 trigger and XFP and OBJ scintillators are used to identify the secondary beam components. The timing information of the scintillators must be individually corrected as the first step of the data calibration phase in order to produce a secondary beam PID where each isotone is well separated. Since the time-of-flight (TOF) of a

nuclei is dependent on the nuclei's trajectory through the S800 as determined by the CRDCs, we must correct the TOF with respect to the angle in the S800 focal plane a_{fp} and the position in the dispersive plane x_{fp}. As a backup measure, the scintillators are connected to multiple time signal converters to add redundancy to the data acquisition system. Time-to-analog converters (TACs) and time-to-digital converters (TDCs) offer two avenues of signal conversion to record the timing signals in the NSCLDAQ. For this work, corrections were made for both of the converters, but the TDC was used for further data calibration as it offered superior resolution over the TAC after calibration.

As shown in Fig. 3.1, a linear correction on the E1-OBJ time difference produces a spectrum where each species of the secondary beam is well separated in time (OBJ) while the trajectory angle in the dispersive plane a_{fp} forms a distribution across the CRDCs. Similar timing corrections were performed with the E1-XFP scintillators and the position in the focal plane x_{fp}. After the scintillator data has been corrected, we plot E1-XFP against E1-OBJ to produce the incoming secondary beam histogram. Figure 3.2 is produced from data taken while no target was installed in TRIPLEX and the S800 rigidity set to center on the secondary beam with an incoming-beam momentum acceptance $dp/p = 1\%$.

As one can see in Fig. 3.2, the $N = 21$ isotones are separated due to a calibration of the timing signal data from the XFP and OBJ scintillators. In addition to the labeled groups of events, we also see another group of events at lower XFP and higher OBJ time differences that is due to other isotone contaminants which are present in the incoming beams. Although it is not included in the plot of Fig. 3.2, there is an additional group of events which is a ghost-type image resulting from the bunched structure of the beam and the timing window imposed on the data collection. When the data collection time window for an event is wider than the time associated with the cyclotron frequency, data will be recorded from the next (or previous) bunch of nuclei that interact with the scintillator, resulting in the second image of the secondary beam isotones.

In practice, the timing corrections were performed with a run where the target was installed in TRIPLEX. It is necessary to use a target-only run for the target-only data calibration as the desired

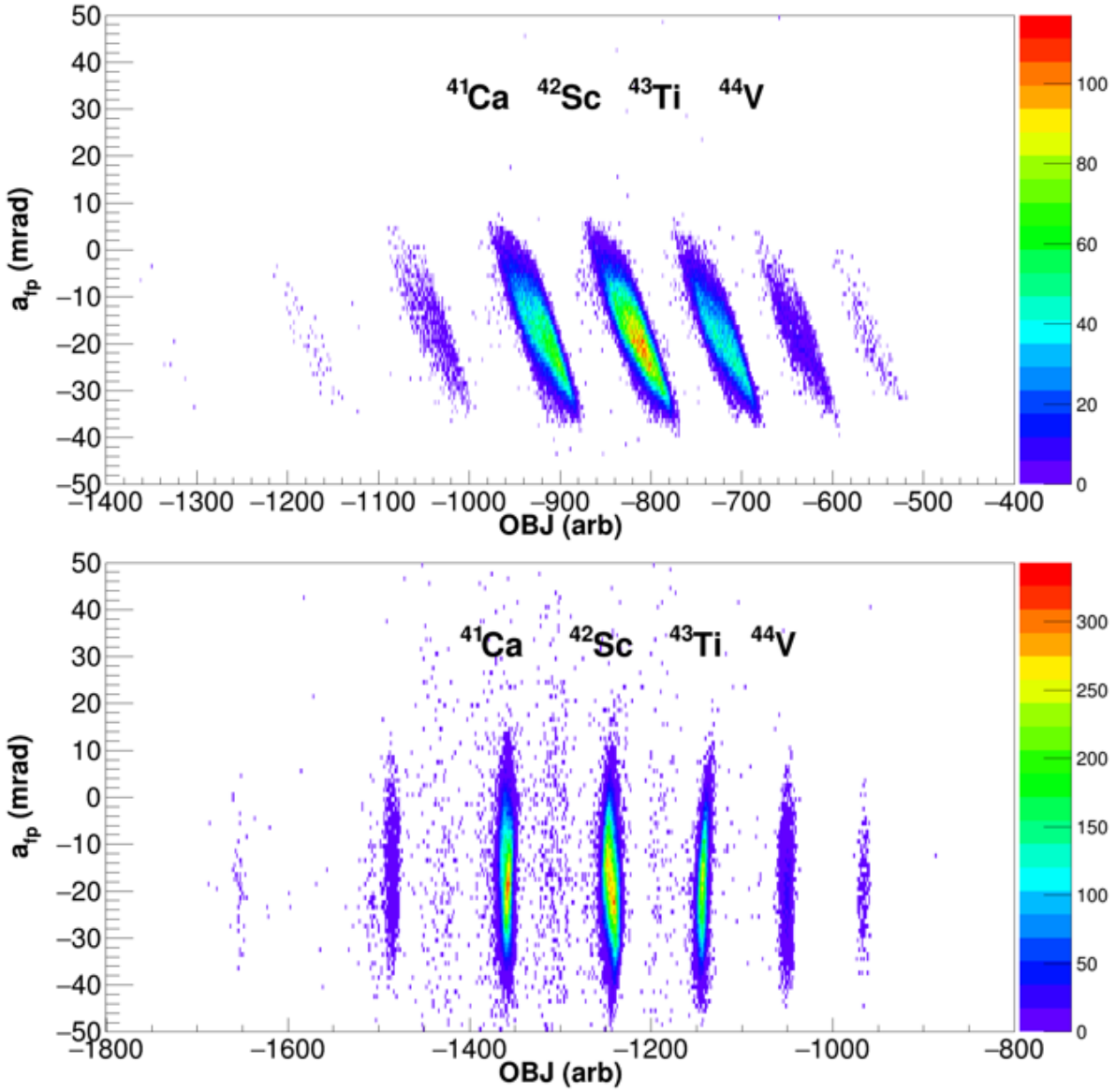

Figure 3.1 Top: Angle a_{fp} in the focal plane as a function of the uncorrected time between the E1 and OBJ scintillators. Bottom: Angle a_{fp} in the focal plane as a function of the corrected time between the E1 and OBJ scintillators After the timing correction, the tilted distributions (top) become aligned (bottom) within narrow time distributions such that the secondary beam nuclei are well separated in time. These plots serve as examples of the timing corrections that were performed as the first step of the data calibration process.

end result of our calibration process is a particle identification diagram (PID, Fig. 2.8) which displays the reaction products associated with the chosen secondary beam. With the PID, we can gate on a specific reaction product and see all gamma rays associated with that ion of interest. The reaction product PID requires proper calibration of the OBJ scintillator data and the ion chamber

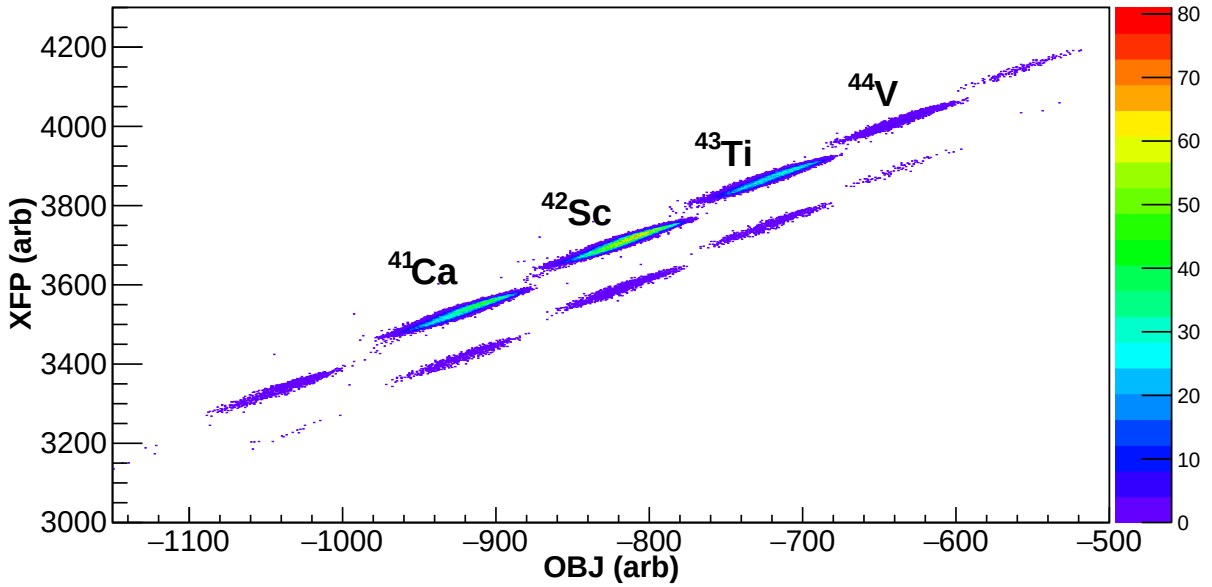

Figure 3.2 Secondary beam components separated by the TOF method where the time differences between the E1 and XFP or OBJ scintillators are plotted on their respective axes. The axes represent arbitrary units of time and the $N = 21$ isotones have been labeled for the reader. This plot was created from a run without the target installed in TRIPLEX and is used to characterize the secondary beam properties.

data which we will describe in the next section.

3.1.2 Ion Chamber Data Calibration

Once the timing corrections have been applied to the scintillator data the next step is calibration of the ion chamber data. We begin the process by plotting the XFP and OBJ scintillator time differences from a target-only run as shown in Fig. 3.3. One may notice that the plot created from the target-only run is a "smeared" version of the plot with no target installed (Fig. 3.2). When we place the target in the beam line, the differences in differential energy loss of individual ions within a given species becomes apparent because each ion is interacting with the target at different locations and losing different amounts of energy than other ions of the same species. This "energy straggling" of the secondary beam ions is attributed to each ion's unique interaction with the Coulomb forces inside the target, resulting in different energy losses for each event. In addition, the S800 spectrograph is set to have a fixed magnetic rigidity and therefore a different velocity component is selected for each isotope based on its A/Z value. The result of energy straggling

within the target is that each ion leaves the target with a slightly different energy, and thus, a slightly different velocity, leading to a distribution of time differences from both scintillators with respect to E1.

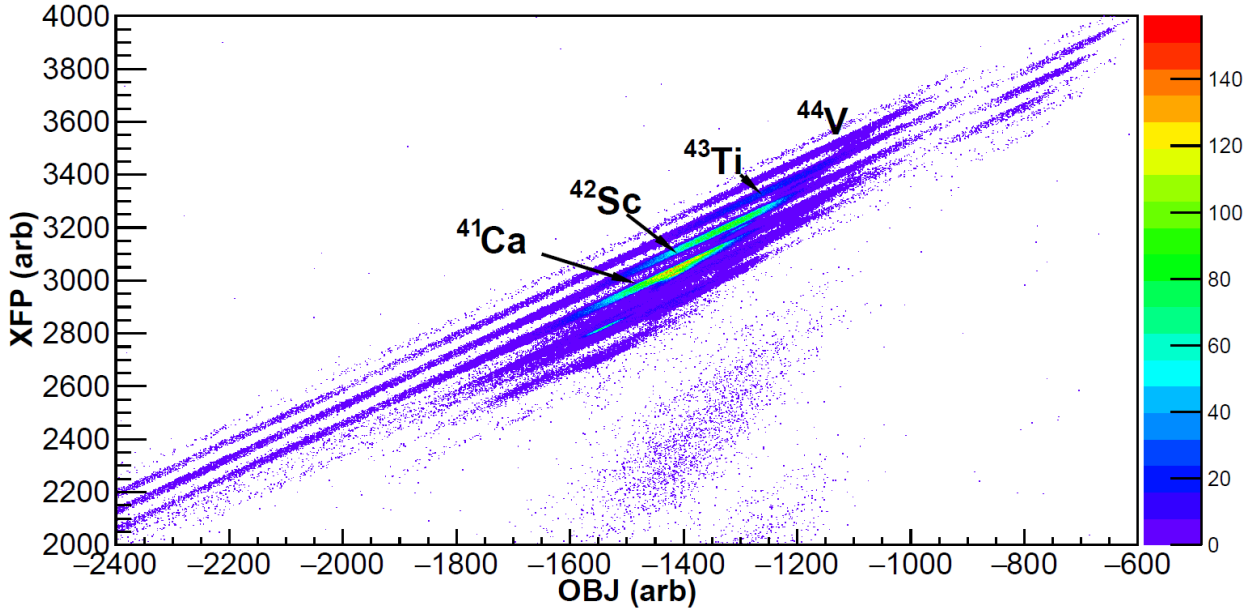

Figure 3.3 Secondary beam components separated by the TOF method for a target-only data run. The axes represent arbitrary units of time and the $N = 21$ isotones have been labeled for the reader. This plot was created from a run with the target installed in TRIPLEX. Gating on a particular secondary beam such as ^{42}Sc for this work allows calibration and analysis of all reaction products from that beam.

Once we have identified the species in the secondary beam PID, as labeled in Fig. 3.3, a graphical tool within ROOT is used to draw a "gate" around the particular isotone we are interested in seeing reaction products from. Using this gate we can then create an uncorrected ion chamber energy loss (dE) versus TOF plot and see all the reaction products associated with that incoming beam. The uncorrected dE vs TOF plot will appear smeared and difficult to resolve but this gives a basic plot to which the corrected version can be compared to. We can then identify a particular reaction product and create a gate that allows us to calibrate the ion chamber data such that energy loss in the ion chamber does not depend on the ion's position in the dispersive plane. This is an important calibration as energy straggling in the target may cause recoil nuclei of the same species to follow slightly different trajectories through the S800 and be detected at different positions in the dispersive plane. Figure 3.4 displays the corrected energy loss in the ion chamber as a function

of position in the dispersive plane (x) for our reaction product of interest, ^{39}Ca. One will note that once the ion-chamber data has been properly corrected, the energy loss of a particular ion traveling through the ion chamber is independent of the recoil nuclei's position in the dispersive plane.

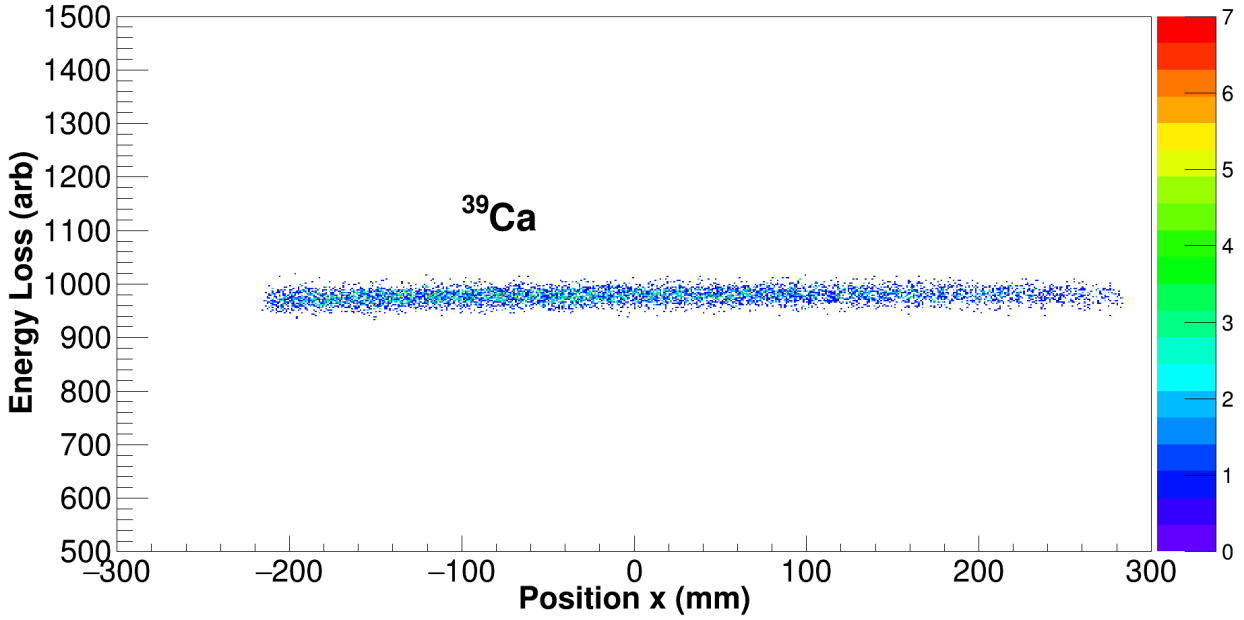

Figure 3.4 The corrected energy loss of ^{39}Ca in the ion chamber (y-axis) is independent of the ion's position (x-axis) in the dispersive plane. Though this ion chamber data correction was performed with a secondary beam of ^{42}Sc and reaction product ^{39}Ca, the calibration holds for our mirror nucleus ^{39}K as well.

3.1.3 CRDC Pad Calibration

As stated in section 2.3.2, the CRDCs detect positions by fitting a Gaussian to the induced-charge distribution over multiple CRDC pads when an ion passes through the chambers. In the data calibration phase, the signals from each of the 224 pads on each CRDC must be gain matched such that they provide consistent voltage information independent of the channel and electronics used to read the signal. The CRDC pad calibration is an iterative process in which the calibration of one pad affects the induced signal read by a neighboring pad; therefore, one pad must be calibrated and then the next pad may be calibrated based on the corrected signal from the previous pad. After several iterations of pad corrections, the induced signal across all pads should be relatively constant, as we see in Fig. 3.5. Though not pictured, both CRDCs must be calibrated in a similar fashion to get accurate gain matching across all channels.

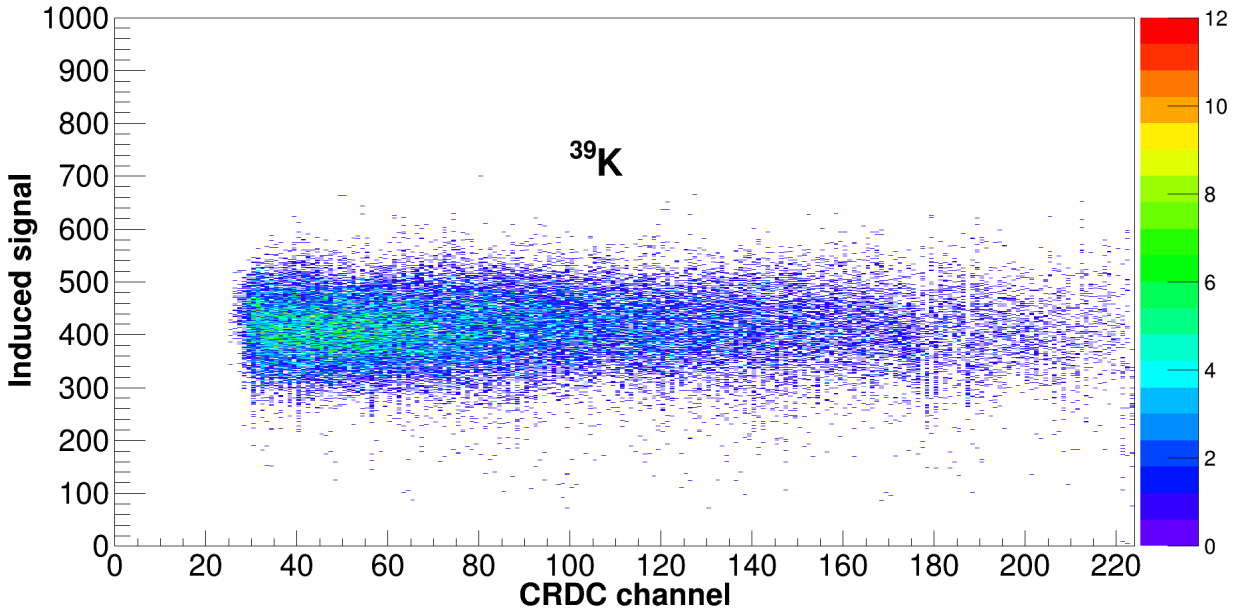

Figure 3.5 The induced signal (y-axis) for a given CRDC pad (x-axis) will be relatively constant after the pad gain-matching calibration. The pad readings from the ^{39}K recoil nuclei are given as an example of a corrected spectrum for a single CRDC.

3.1.4 CRDC Mask Calibration

The final calibration performed on the CRDC data is referred to as the "mask" calibration. As stated in section 2.5.2, two mask-calibration runs were conducted during the experiment with the target installed on TRIPLEX. During these runs, an aluminum plate is placed in front of a CRDC and data is taken for approximately 10 minutes per run. The aluminum plate contains a pattern of holes through which beam particles are allowed to pass. Particles that pass through the mask create a pattern in the CRDC that corresponds to the hole pattern on the aluminum plate. The readings from the CRDC mask runs are then used to calibrate the position readings from the CRDC pads.

Figure 3.6 shows the result of a mask run in the left panel and the mask pattern in the right panel. During the mask calibration the hole pattern from the data run on the left is matched to the corresponding mask pattern on the right. Multiple holes are used in the calibration and the position information from the data is plotted as a function of the known hole-position information from the pattern on the right. A linear function is then fit to the calibration-plot data which contains a slope and offset. The experimental data is then re-run with the proper CRDC slope and offset information to calibrate the CRDC position data. Here we will note that although the aluminum mask was

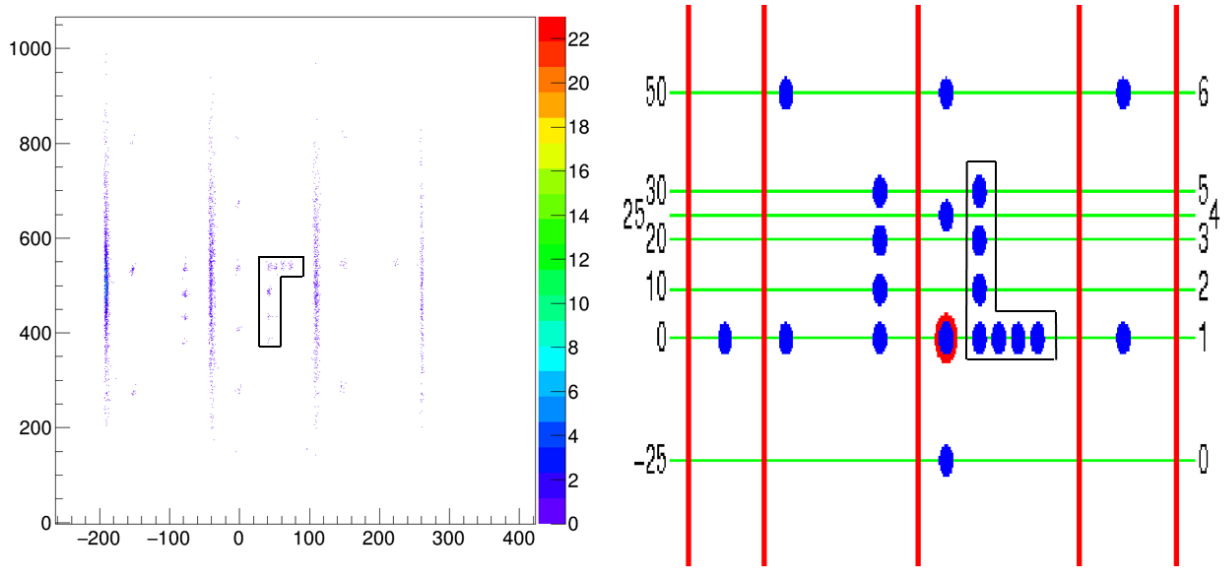

Figure 3.6 CRDC X and Y position calibration using the mask pattern. The aluminum mask was inverted when placed in front of the first CRDC, but the position calibration holds so long as each cluster of data points on the left is correctly matched to the associated mask hole on the right. An outline of the "L" pattern has been added to show correspondence between the data in the left panel and the calibration pattern in the right panel.

inverted when placed in front of the upstream CRDC, as shown by the "L" outlines provided in Fig. 3.6, the calibration process is independent of the plate orientation so long as each cluster of data points is associated with the proper hole pattern.

3.1.4.1 S800 Inverse Map

Once the CRDC position data has been corrected, we calculate the trajectory of ions at the target location from the CRDC data taken in the focal plane. To obtain the ion trajectory angle in the dispersive plane a_{ta}, the angle in the non-dispersive plane b_{ta}, the ion position in the non-dispersive plane y_{ta}, and the difference in ion energy d_{ta} with respect to the energy of an ion along the S800 central trajectory, we must use a transformation matrix that maps the trajectory detected by the CRDCs back to the trajectory at the target location on an event-by-event basis.

The transformation matrix, commonly referred to as the "inverse map", is calculated from the magnet settings of the S800 for a particular nuclei of interest; specifically: two quadrupole current settings (in Amps), the two S800 dipole current settings, the rigidity setting (in Tm) of the S800 during the specific run type (no target, target-only, or target+degrader), the mass (A) and charge

(Z) of the nuclei of interest, and the distance between the TRIPLEX target and the S800 pivot point. From these values a transformation matrix can be produced which, when applied to the data calibration, builds the a_{ta}, b_{ta}, y_{ta}, and d_{ta} distributions on an event-by-event basis.

The distributions are Gaussian in nature but may not have a mean centered at the zero position or angle due to inconsistencies in the CRDC readings which may cause the position reading to drift over the course of hours or days. Therefore, once the inverse map is applied to the data, run-by-run corrections are made to the trajectory distributions to center the mean at the zero position and zero angle. Because our simulation does not drift over time, the run-by-run corrections to a_{ta}, b_{ta}, and y_{ta} are applied to the data so that the simulated distributions align with the experimental distributions.

This concludes the discussion of the data calibration. In the next section, a description of the simulation calibration processes will be discussed followed by the lifetime analysis of the ^{39}Ca and ^{39}K states covered in two sections which are associated with the particular nucleus of interest.

3.2 Simulation Calibration

Calibrating the G4Lifetime simulation to the experimental data starts with the characterization of the incoming beam profile. As displayed in Fig. 3.2, the time-of-flight method is employed for two runs without a target installed to aid in determining the secondary beam characteristics, which are parameters necessary for the most accurate reproduction of the experimental data. From the S800 rigidity settings and data runs with no target installed we can determine the secondary beam energy. But when the target is installed, reactions in the target produce recoil nuclei and knocked out nucleons which carry energy and provide information about the reaction. Therefore, we must adjust the parameters in our simulation to match the experimental measurements.

Figure 3.7 provides the corrected trajectory distributions for the unreacted secondary beam of ^{42}Sc for a single, target-only run. The incoming secondary beam energy of 85.2 MeV/u was calculated from the S800 rigidity setting $B\rho$ = 2.2188 Tm for the run. By fitting the simulated d_{ta} distribution (red) to the data (blue) it was determined that a scale factor of 0.93 was required to replicate the effective density of the ^{9}Be target. In a similar fashion, another unreacted beam run

was used to determine that the effective density of the ^{181}Ta degrader was best replicated with a scale factor of 0.96.

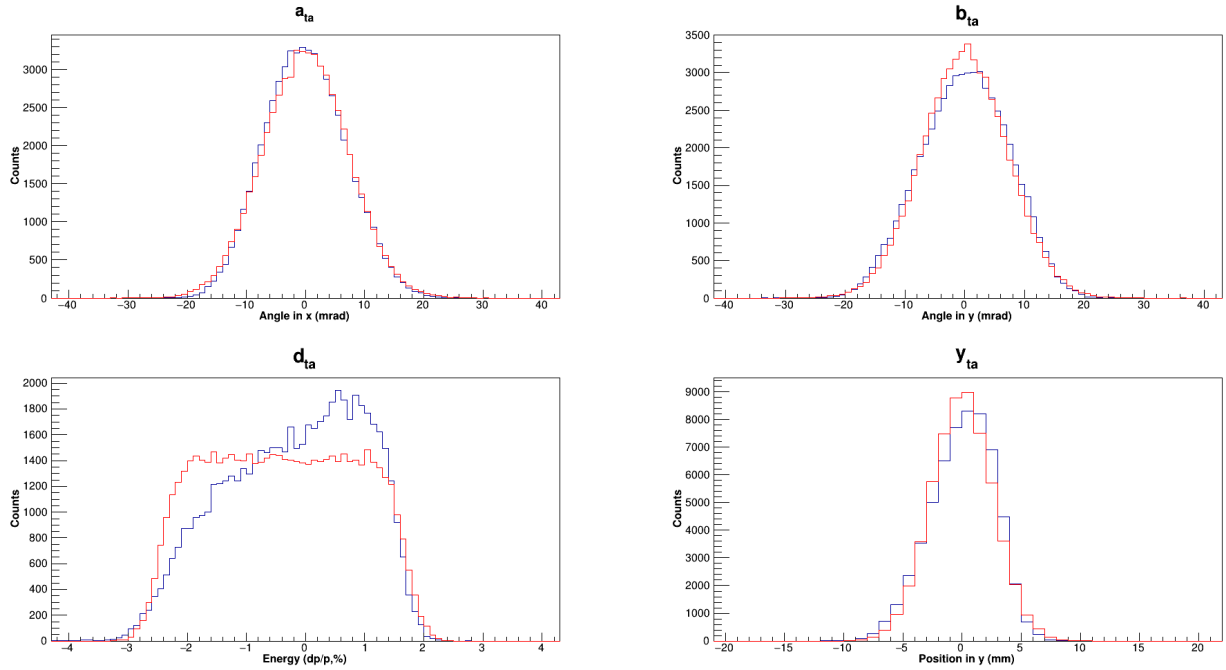

Figure 3.7 Trajectory distributions at the TRIPLEX target position for the unreacted ^{42}Sc beam. Experimental data for the angle in the dispersive plane a_{ta}, angle in the non-dispersive plane b_{ta}, position in the non-dispersive plane y_{ta}, and the energy distribution d_{ta} are displayed in blue. The simulated secondary beam trajectory information is displayed in red.

Once the incoming beam, target, and degrader properties were determined we began characterization of the outgoing, reaction-product beam. This process again relies on the trajectory distributions at the target position. For outgoing beam properties relevant to our nuclei of interest, we gate on the particular recoil nuclei and use the trajectory distributions to determine the outgoing beam properties. Fig. 3.8 displays the trajectory distributions at the target for the reaction product ^{39}Ca during a target-only run. From the S800 rigidity setting $B\rho$ = 2.1296 Tm, we calculated that our recoil nuclei have an energy distribution centered at 55.9 MeV/u. We then adjusted parameters associated with the energy centroid and distribution width of the knocked-out nucleon and the difference in velocity between the incoming beam and outgoing beam to fit the simulated d_{ta} (red) to the data (blue), as is displayed in Fig. 3.8. By fitting the d_{ta} spectrum, the necessary reaction information is passed to the simulation such that the angle distributions a_{ta} and b_{ta}, and position distribution y_{ta}, are replicated by the simulation.

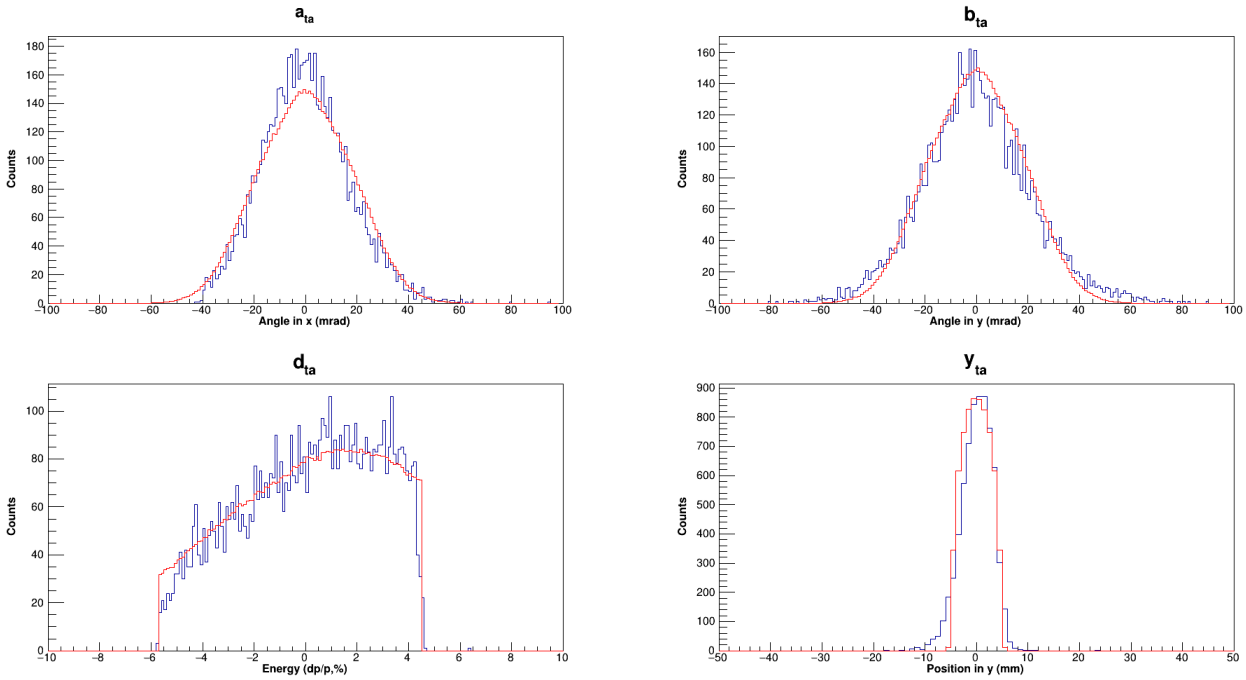

Figure 3.8 Trajectory distributions at the TRIPLEX target position for the reaction product ^{39}Ca taken during a target-only run. Experimental data for the angle in the dispersive plane a_{ta}, angle in the non-dispersive plane b_{ta}, position in the non-dispersive plane y_{ta}, and the energy distribution d_{ta} are displayed in blue while the simulation is displayed in red.

Finally, for the runs with both target and degrader installed on TRIPLEX another set of trajectory distributions was created to characterize the outgoing beam information after interaction with the tantalum degrader. From the S800 rigidity setting $B\rho$ = 1.8351 Tm, we calculated that our recoil nuclei have an energy distribution centered at 41.9 MeV/u. The distributions associated with the plunger data (target and degrader) are given in Fig. 3.9. Parameters associated with the energy of the knocked-out nucleon were adjusted, as was done with the target-only distributions, and the relevant parameters were passed to the simulation to produce the most accurate representations of the gamma-ray spectra.

The same calibration process described above was also performed for the ^{39}K simulations. The ^{9}Be(^{42}Sc, ^{39}K)X reaction relied on the same ^{42}Sc beam properties and target/degrader properties, therefore, the energy distribution d_{ta} was fitted to obtain the unique parameters required to characterize the outgoing ^{39}K beam. With both the data and the simulations calibrated we could then create the gamma-ray spectra and move onto the analysis of the data by comparison to the

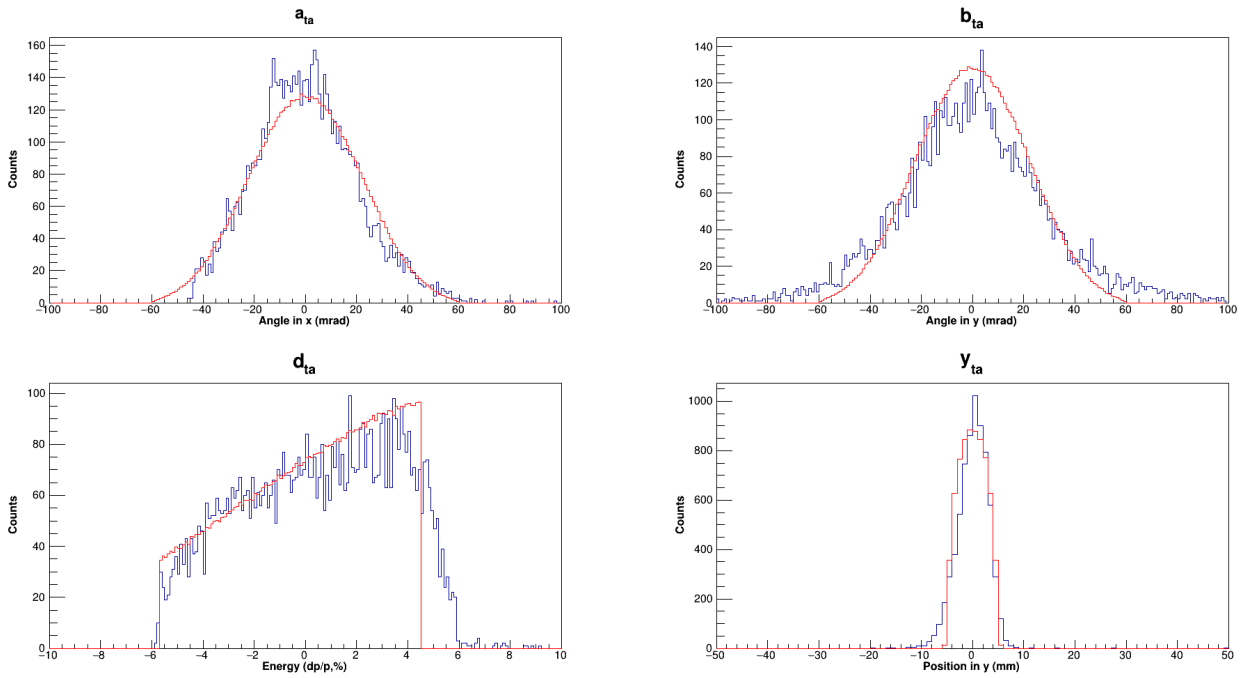

Figure 3.9 Trajectory distributions at the TRIPLEX degrader position for the reaction product ^{39}Ca taken during a run with target and degrader mounted. Data for the angle in the dispersive plane a_{ta}, angle in the non-dispersive plane b_{ta}, position in the non-dispersive plane y_{ta}, and the energy distribution d_{ta} are displayed in blue while the simulation is displayed in red.

simulations for the purpose of determining the lifetime of our states of interest.

3.3 Analysis Overview

As mentioned in section 2.5.2, the data were taken for three TRIPLEX configurations: target-only, target and degrader with 1 mm separation, and target and degrader with 0 mm separation. The gamma-ray peaks from the target-only spectra were compared to the adopted values [45] of the transition energies to determine which excited states were populated and which gamma-ray peaks were associated with which transitions. The states which were populated in this experiment as well as the transitions observed are depicted in Fig. 3.10. The target-only spectra were also used to determine in what percentages each excited state was populated in both ^{39}Ca and ^{39}K.

The 1 and 0-mm spectra were used to determine the lifetimes of the excited states of interest; that is, the $11/2^-$ and $9/2^-$ excited states. Application of the recoil-distance method for the lifetime measurement of the $11/2^-$ state provided a model independent determination of the reduced transition strengths ($B(E2)$). Evaluation of the lifetime of the $9/2^-$ state in ^{39}Ca was opportunistic

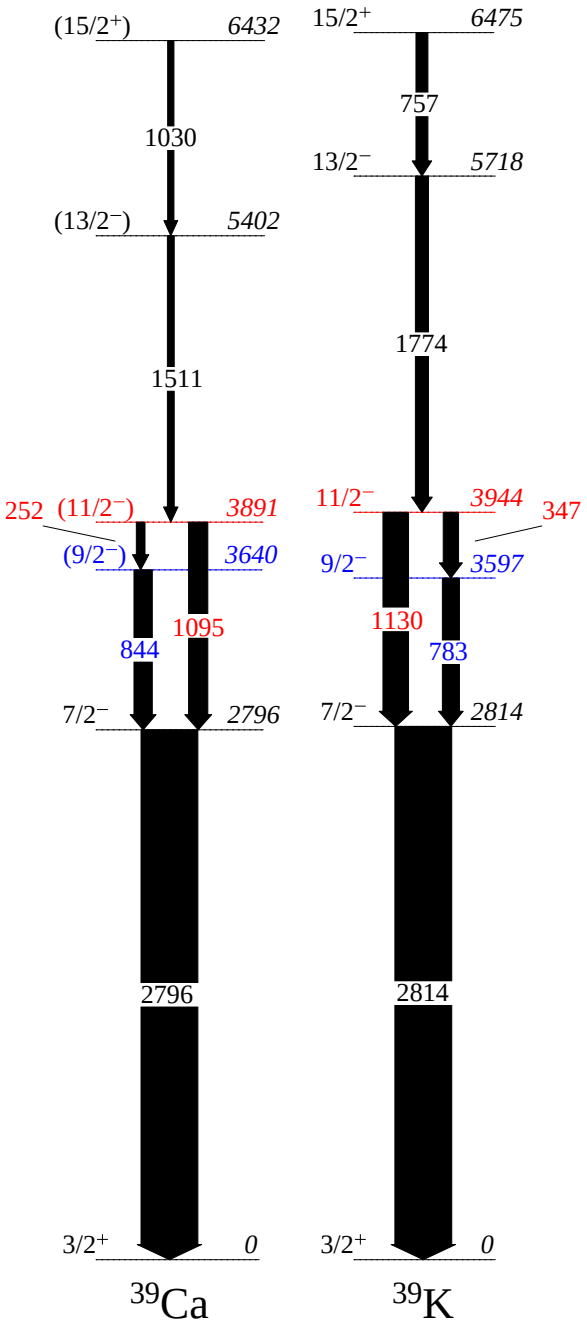

Figure 3.10 Level diagrams for gamma rays observed in the target-only spectra for ^{39}Ca (left) and ^{39}K (right). The energy information is from Ref.[45] and rounded to keV. The relative intensities of the observed gamma-ray transitions, indicated by the widths of the arrows, are normalized to the intensity of the $7/2^- \rightarrow 3/2^+_{g.s.}$ transition for the respective nuclei. The energy information for the $(11/2^-)$ state is highlighted in red, while those for the $(9/2^-)$ state are highlighted in blue [88]. Reprinted figure with permission from A. Sanchez *et al.*, Phys. Rev. C, vol. 110, p. 024322 (2024). Copyright (2024) by the American Physical Society.

as the plunger configurations were, by chance, sensitive to the $9/2^-$ state as well as the $11/2^-$ state of interest, thus allowing for a more precise measurement of the $9/2^-$ state lifetime, which had only been measured once prior to this work [53]. Agreement between the known lifetimes of the $11/2^-$ and $9/2^-$ states in ^{39}K and the lifetimes determined in this work strengthened confidence in the analysis methods employed for lesser known lifetimes of the analog states in ^{39}Ca.

For both nuclei, a rigorous analysis of systematic errors which contributed to uncertainty in the lifetime measurements was performed. The systematic error analysis accounted for the effects of lifetime and population of the higher lying $15/2^+$ and $13/2^-$ states on the lifetime measurement of the lower lying $11/2^-$ and $9/2^-$ states. The observation of the short-lived $13/2^-$ state provided data that were used to constrain the ratio of reactions on target to reactions on degrader, which was another parameter used in the simulation.

In the following sections we will delve into the analysis of each nucleus by examining the spectra obtained from each TRIPLEX configuration. Since the analysis performed on ^{39}Ca was validated by using the same method on the ^{39}K data, most of the detailed analysis methods will be contained in the ^{39}Ca sections. The particular analysis procedures for ^{39}K which diverged from the ^{39}Ca procedures will be examined in the ^{39}K analysis sections.

3.3.1 ^{39}Ca Target-only Data

The gamma-ray spectrum for ^{39}Ca measured with the target-only configuration is provided in Fig. 3.11. This figure presents the energy spectrum for gamma rays measured by all GRETINA detectors where Doppler-shift corrections were applied with the gamma-ray emission angle θ and ion velocity at the downstream face of the target, $\beta = 0.33$. Figure 3.11 includes background contributions from neutron-induced reactions which were evaluated in the laboratory frame and whose responses in the ion frame were simulated and included in the fit [89]. The neutron-induced backgrounds are depicted in green and it should be noted that a low-angle cut was not applied to the target-only data; therefore, the lab-frame backgrounds appear "smeared out" in the Doppler-corrected spectra; but when the cut is applied, as it is in the 1 mm and 0 mm data, the contributions from the lab-frame backgrounds are evident. Two exponential functions are assumed

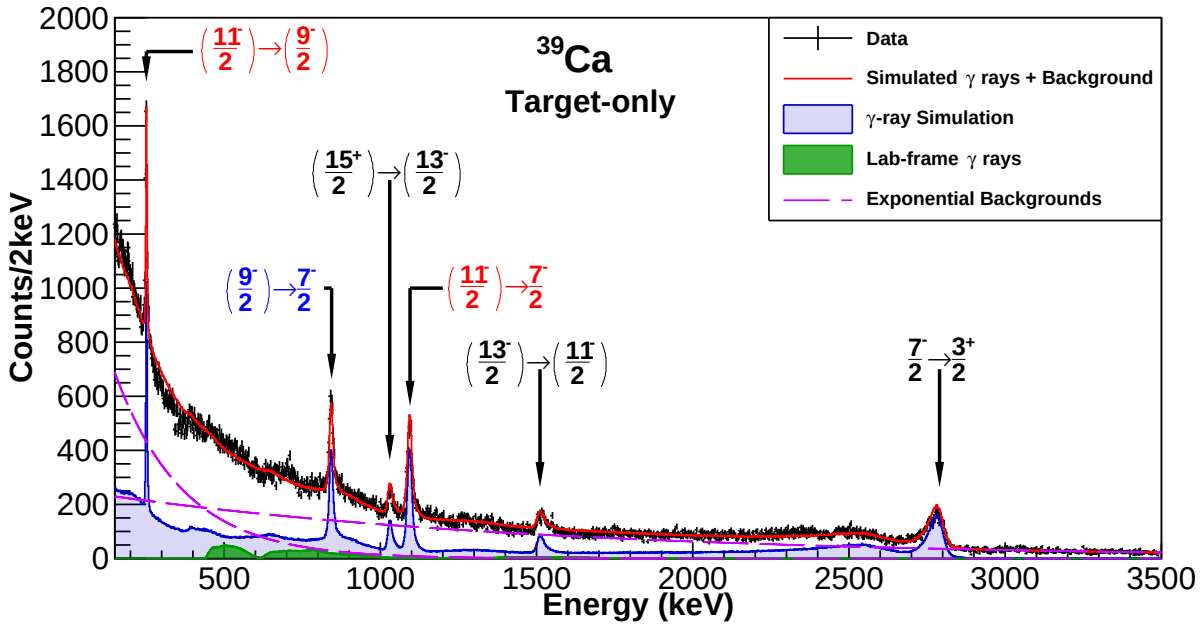

Figure 3.11 Doppler-corrected gamma-ray spectrum for ^{39}Ca for the target-only run. Transitions from the $(11/2^-)$ state are labeled in red, from which the lifetime is determined in the present work. Gamma rays from the $(9/2^-)$ state are labeled in blue, for which we provide an improved lifetime result [88]. Reprinted figure with permission from A. Sanchez *et al.*, Phys. Rev. C, vol. 110, p. 024322 (2024). Copyright (2024) by the American Physical Society.

for the background and the simulation was fit to the data using the log likelihood method. The gamma-ray peaks associated with ^{39}Ca are clearly visible at 252 keV, 844 keV, 1030 keV, 1095 keV, 1511 keV, and 2796 keV. By matching the experimental gamma-ray energy to available data for ^{39}Ca, the spin-parities and energies of each transition were clearly identified. Gamma-gamma coincidence was used to verify that the gamma-ray transitions observed in Fig. 3.11 belong to the cascade shown in Fig. 3.10, with the 6432-keV $(15/2^+)$ state being the highest populated.

Once the coincidences had been verified, the order of the cascade was discernible from the Nuclear Data Sheets [45] for ^{39}Ca, available from the National Nuclear Data Center (NNDC) [33]. A reaction in the target could result in the direct population of the $15/2^+$ state at 6432 keV and a subsequent decay by emission of a 1030 keV gamma-ray to the $13/2^-$ state, which then proceeds to decay to the $11/2^-$ state by emission of a 1511 keV gamma-ray. When the $11/2^-$ state was populated by direct population from the reaction or by indirect population from decay of the $13/2^-$ state, a transition to the $9/2^-$ state at 3640 keV or to the $7/2^-$ state could ensue. The probability

of the $11/2^-$ state decaying to the $9/2^-$ or to the $7/2^-$ state is the branching ratio of the state. An interaction with the target could also directly populate the $7/2^-$ state at 2796 keV or the state could be indirectly populated by decay from the $9/2^-$ or $11/2^-$ states.

The spectrum was compared to a simulation which utilizes the GEANT4 [83, 84, 90] package developed to reproduce RDM experiments utilizing TRIPLEX and GRETINA [89, 91, 90, 51]. The gamma-ray transitions indicated by arrows in Fig. 3.10 were included in the simulation. Once properly calibrated, the G4Lifetime simulation requires four parameters to produce a gamma-ray spectrum: the level energy, the gamma-ray transition energy, the direct population fraction of the state, and the lifetime of the state. Since the level energies and the gamma-ray transition energies are known quantities, the two main parameters that were adjusted in the simulations were the lifetimes and direct populations of the states. A cascade can be implemented in the simulation when the level energy of the lower state is equal to the level energy of the higher state minus the energy of the emitted gamma ray. In this manner, we were able to simulate cascades of decays starting with the $15/2^+$ state and ending with a decay from the $7/2^-$ state to the $3/2^+$ ground state. Though the order of the cascade was evident, quantifying the probability that a particular state was directly populated in a reaction required a more rigorous methodology using two simulations to reproduce the two cascade paths created by the branch in the $11/2^-$ state. Suffice it to say, the direct populations to all excited states in the cascade from the ^{9}Be(^{42}Sc, ^{39}Ca)X reactions were determined from the yields of the gamma-ray peaks in the target-only spectrum, with considerations given to indirect populations from the observed higher-lying states.

The results of the analysis of the direct population fractions for each of the observed states were normalized such that their sum is 100% and direct population to the ground state was not calculated, nor were populations to unobserved states, due to the absence of gamma-ray peaks to analyze. Reactions on the target resulted in a weak direct population of 11(3)% to the 6432-keV $(15/2^+)$ state, which then decays by emission of the 1030-keV gamma ray to the $(13/2^-)$ state. The weakest direct population of 1(1)% was observed for the 5402-keV $(13/2^-)$ state, which decays by emission of the 1511-keV gamma ray to the $(11/2^-)$ state. The strongest direct population of

37(8)% was observed for the 3891-keV $(11/2^-)$ state, which emits the 252-keV gamma ray decaying to the $(9/2^-)$ state and the 1095-keV gamma ray decaying to the $7/2^-$ state. A direct population of 17(4)% was determined for the 3640-keV $(9/2^-)$ state, which decays via the 844-keV gamma-ray transition to the 2796-keV $7/2^-$ state. Finally, a direct population of 34(10)% was observed for the $7/2^-$ state, which decays directly to the $3/2^+$ ground state. One may also note that we did not observe the population to the $1/2^+$ state at 2467 keV in our target-only measurement, as was the case for a recent study of ^{39}Ca by Gade *et al.* [92].

The relative branching ratio of the 252-keV gamma ray $b_{rel} = 43(3)$ with respect to the 1095-keV gamma-ray branch $b_{rel} = 100(6)$ for the $(11/2^-)$ state was calculated from the ratio of gamma-ray intensities at each energy. Within quoted uncertainties, our result agrees with the adopted value of the relative branching ratio for the 252-keV branch, $b_{rel} = 51(6)$ [45]. Based on our relative branching ratio, we find an absolute branching ratio $b_{abs} = 70(2)\%$ for the 1095-keV decay; this value is later used with the gamma-ray energy and the lifetime to calculate the reduced transition strength $B(\mathrm{E2}, (11/2^-) \rightarrow 7/2^-)$.

3.3.2 ^{39}Ca RDM Analysis

Having determined the populations of excited states from the target-only data, we move to the analysis of the recoil-distance lifetime data. The measured spectrum for the 1-mm target-degrader separation is presented in Fig. 3.13 where Doppler-shift correction was performed with $\beta = 0.29$, corresponding to the velocity of the ions on the downstream face of the degrader. The spectrum measured with the 0-mm separation is presented in Fig. 3.14 and was corrected for Doppler shifts with the same β value.

As discussed in Sect. 2.5.3, excited states with lifetimes to which the target-degrader configuration is sensitive show a characteristic double-peak structure in the 1D gamma-ray spectrum. These structures can be seen in the 1-mm spectrum for the $(11/2^-) \rightarrow 7/2^-$ and $(11/2^-) \rightarrow (9/2^-)$ transitions labeled in red, and the $(9/2^-) \rightarrow 7/2^-$ transition in blue, in Fig. 3.12. The two components of the gamma-ray double-peak structure are defined by their decay location along the ion trajectory; gamma rays emitted before an ion reaches the degrader are denoted "fast" components

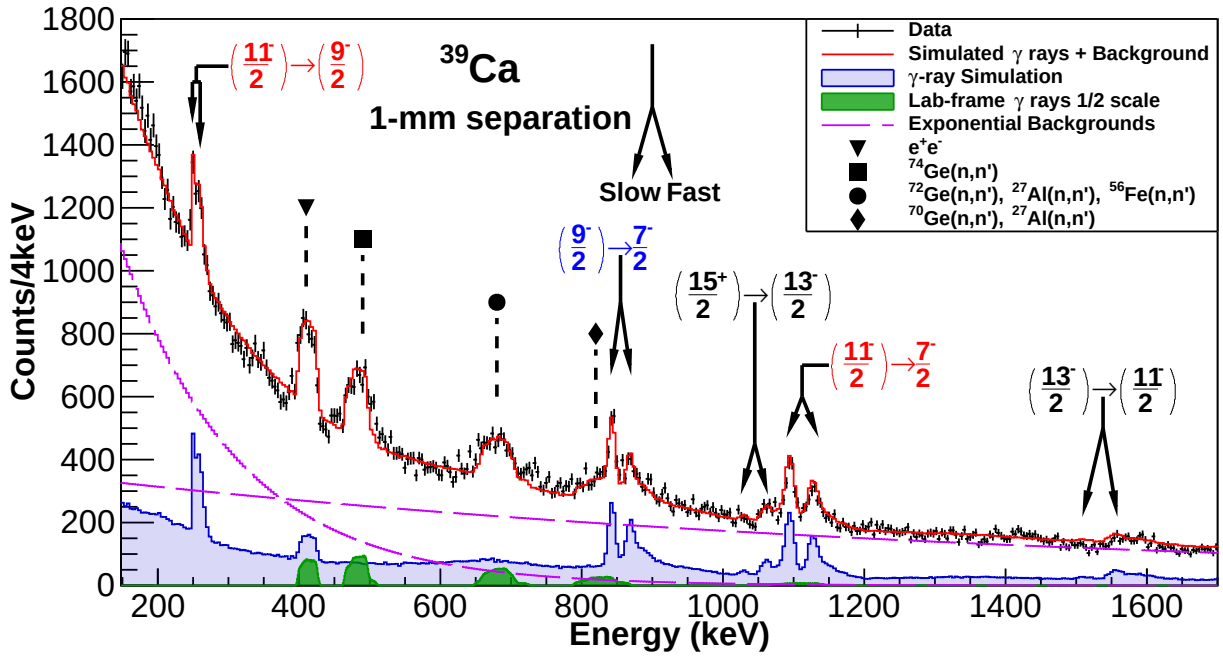

Figure 3.12 Doppler-corrected gamma-ray spectrum for ^{39}Ca taken with the 1-mm target-degrader separation. The spectrum has been gated for the gamma-ray emission angle between $\theta = 29°$ and $\theta = 46°$ to improve sensitivity to Doppler shifts. Transitions from the $(11/2^-)$ state are labeled in red, while transitions from the $(9/2^-)$ state are labeled in blue. Laboratory-frame background gamma rays, associated with neutron-induced reactions [89], are shown in green and downscaled by a factor of 2 for clarity [88]. Reprinted figure with permission from A. Sanchez *et al.*, Phys. Rev. C, vol. 110, p. 024322 (2024). Copyright (2024) by the American Physical Society.

while gamma rays emitted after an ion passes through the degrader are called "slow" components. Both spectra were produced from an angle gate of a 2D histogram for detectors between 29° and 46°. The low-angle gate improved sensitivity to Doppler shifts while separating the fast component of the $15/2^+ \rightarrow 13/2^-$ transition at 1060 keV from the slow component of the $11/2^- \rightarrow 7/2^-$ transition at 1095 keV.

In Figs. 3.12 and 3.13, we observe that the low-angle cut results in sharpened background peaks resulting from lab-frame emissions which are simulated in green and labeled with black geometric icons. Starting at the low-energy end of the spectra, we first observed the pair-production peak at approximately 400 keV. As discussed in Sec. 2.4, pair production can occur when a gamma ray interacts with the Coulomb field of a nucleus, producing an electron-positron pair in which the positron will annihilate with another electron to produce another pair of gamma rays. If the pair-

production occurs outside the detector volume, say by a gamma ray interacting with the aluminum beam pipe, a gamma ray of energy 511 keV may enter the detector volume and deposit its full energy, thereby creating a peak at 511 keV in the lab-frame spectrum. After the spectrum has been Doppler corrected to the ion frame, the Doppler corrected energy at low angles is over corrected and the 511 keV peak will be displayed at a lower energy after a low-angle gate is applied to the spectrum. Another common process which produces lab-frame peaks in the plunger spectra is neutron-induced radiation; in this process, an energetic neutron is released from the beam-target reaction and proceeds to interact with other materials in the detector vicinity such as the aluminum beam pipe or the germanium detector volume. When the energetic neutron inelastically scatters off another nucleus, the lab-frame nucleus becomes excited and releases a gamma ray by deexcitation. The gamma rays from neutron-induced radiation are released from lab-frame nuclei and are absorbed in the detector volume. These gamma rays can be identified as originating from a specific material by their energy in the lab-frame spectra and, as with the pair-production peak, are overcorrected at low angles in the Doppler correction process and therefore appear at lower energies when a low-angle gate is applied to the ion-frame data. In both the ^{39}Ca and ^{39}K spectra we observe peaks at approximately 500 keV which are the result of the 596 and 609-keV gamma rays released by neutron excitation of ^{74}Ge nuclei in the detector volume. At approximately 700 keV we observe a single peak which is the combined result of an 834-keV gamma ray from the excitation of ^{72}Ge, an 844-keV gamma ray from the excitation of ^{27}Al, and an 846-keV gamma ray due to the excitation of ^{56}Fe. Finally, at approximately 825 keV we observe a peak which is the combined result of a 1014-keV gamma ray released from excited ^{27}Al and a 1040-keV gamma ray released from excited ^{70}Ge. The above listed background contributions were identified in the lab-frame spectra and their responses in the ion-frame were simulated and added to the exponential backgrounds and the simulated ^{39}Ca spectra to produce the overall fits shown in red.

Since the Doppler-shift correction was optimized for decays behind the degrader, the slow components appear at the proper ion-frame energies for the transitions. On the other hand, the fast components are under-corrected and therefore appear at higher energies. For instance, in Fig. 3.12,

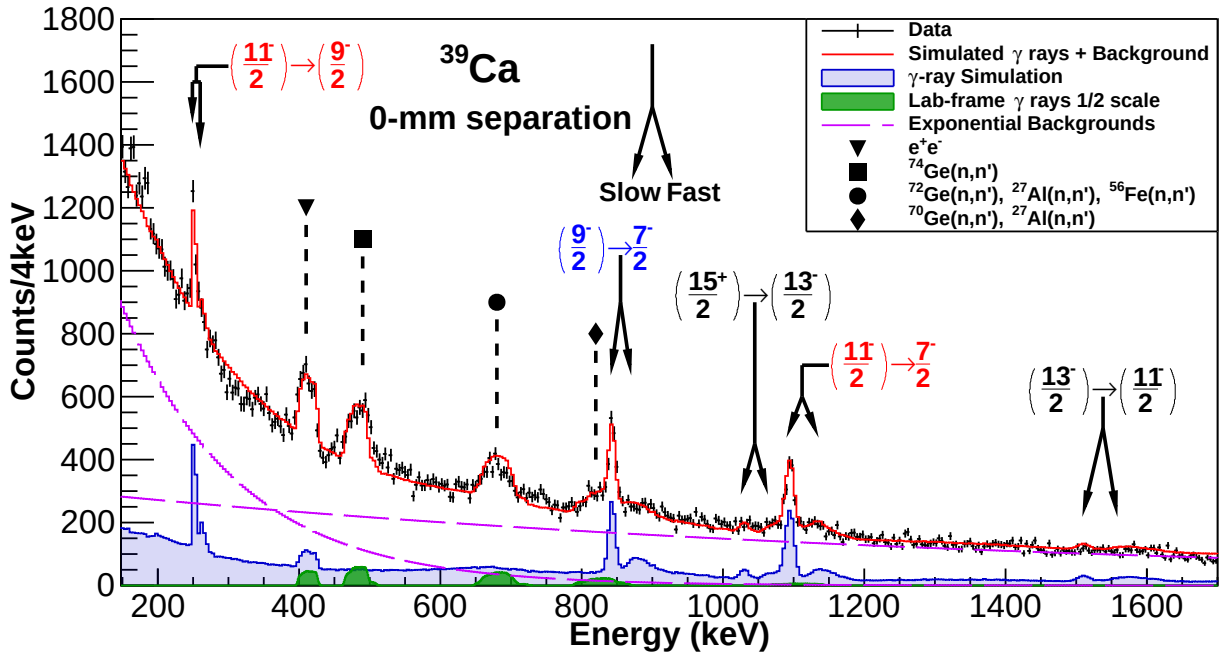

Figure 3.13 Doppler-shift corrected gamma-ray spectrum for ^{39}Ca taken with the 0-mm target-degrader separation setting. The spectrum has been gated between $\theta = 29°$ and $\theta = 46°$ to improve sensitivity to Doppler shifts. Transitions from the $(11/2^-)$ state are labeled in red, while transitions from the $(9/2^-)$ state are labeled in blue. Laboratory-frame background gamma rays are shown in green and downscaled by a factor of 2 [88]. Reprinted figure with permission from A. Sanchez *et al.*, Phys. Rev. C, vol. 110, p. 024322 (2024). Copyright (2024) by the American Physical Society.

gamma rays from the $(11/2^-)$ state emitted after the degrader compose the true energy peak at 1095 keV, whereas those emitted before the degrader form the higher-energy fast-component peak observed at 1150 keV, having been under-corrected by the choice of lower β.

Based on data available for the mirror states in ^{39}K, the $(15/2^+)$ and $(13/2^-)$ states in ^{39}Ca are both expected to have lifetimes that are relatively short for this target thickness and foil separation and, in Fig. 3.12, we observe only the fast components of the transitions at 1060 keV and 1570 keV, respectively. The $7/2^-$ peak at 2796 keV has been omitted from the analysis; since it is the lowest-lying excited state, it does not feed any states of interest and therefore has no effect on the lifetime measurements of the higher lying states. We also note from Fig. 3.13 that when the target-degrader separation is 0 mm we observe a diminished fast component, which is consistent with more decays occurring behind the degrader.

In Sect. 2.5, the basic methodology fo RDM measurements was introduced where the ratio of

fast and slow components provides a sensitivity to the lifetime. But because other experimental conditions contribute to the yields of fast or slow components, the ratio must be measured at multiple distance settings to quantify the evolution of the ratio due to the lifetime [93]. These additional contributions can be constrained by taking additional data sets tailored to determine the contributions, but usually it is not possible or practical to have such extensive data sets. Therefore, data is taken such that the most significant contributions to peak ratios can be constrained.

For recoil-distance lifetime measurements with relativistic-energy beams, it is important to understand and constrain contributions of reactions occurring within the degrader, which can act as a second target to populate excited states of interest. In practice, the ratio of reactions on target to reactions on degrader should be quantified to obtain the best possible parameter set in our simulations [35]. To quantify this ratio we used the 1-mm separation data and analyzed the transitions from the $(15/2^+)$ and $(13/2^-)$ states, which are expected to be short-lived with respect to flight time over the foil separation. As can be observed in Fig. 3.12, both transitions from the $(15/2^+)$ and $(13/2^-)$ states are dominated by their fast components, with very little hint of slow components for each transition. Since the lifetimes of these states are not known [45], we estimated their lifetimes from the available data for analogue states in ^{39}K by accounting for the energy differences of the decays based on the $1/E_\gamma^{2\lambda+1}$ dependence; that is, the reduced transition strength for an electromagnetic transition can be given by

$$B(\pi\lambda,\downarrow) = \frac{C}{E_\gamma^{2\lambda+1} T_p} \tag{3.1}$$

where $\pi = E$ for electric transitions, $\pi = M$ for magnetic transitions, E_γ is the gamma-ray energy for the transition, λ is the allowed change in angular momentum for the transition, C is a constant specific to each transition type (E1, E2, M1, M2, etc...), and T_p is the partial half-life. If we assume isospin symmetry, the ratio of transition strengths for a pair of mirror states could be equal to 1 and the partial half-life of an unknown state $J^{\pi*}$ can be estimated from the ratio of gamma-ray energies and the half-life of the known state J^π by

$$T_{p,J^{\pi*}} = \frac{E_\gamma^{2\lambda+1}}{E_{\gamma*}^{2\lambda+1}} T_{p,J^\pi} \tag{3.2}$$

For this work, we assumed a dipole ($\lambda = 1$) transition for the $(15/2^+) \rightarrow (13/2^-)$ case as the quadrupole component with $\delta(M2/E1) = 0.002$ [45] is negligible, and we calculated a mean lifetime of $\tau = 4.8$ ps for the $(15/2^+)$ state of ^{39}Ca. For the $(13/2^-) \rightarrow (11/2^-)$ transition in ^{39}Ca we also assumed a prominent dipole component as the evaluation of the $(13/2^-)$ state yields a 6% quadrupole component (from $\delta(E2/M1) = -0.25$ [45]) based on data for analogue states in ^{39}K, from which we estimated a lifetime of $\tau = 0.4$ ps. Therefore, both states in ^{39}Ca are expected to be relatively short-lived compared to our 1-mm separation distance. The gamma-ray spectra including the $(15/2^+) \rightarrow (13/2^-)$ and $(13/2^-) \rightarrow (11/2^-)$ transitions were then simulated as a cascade to account for feeding effects on the $(13/2^-)$ state. By adjusting the ratio of reactions on target to degrader within our simulation we determined a lower limit of the ratio to be $15(1) : 1$, indicating that reactions on the target are dominant compared to those on the degrader in the ^{39}Ca data.

Using the direct populations and the target-degrader reaction ratio calculated above, simulations for the cascade in Fig. 3.10 were performed with a wide range of lifetimes for the states of interest. The lifetime range was then narrowed down accordingly with fit results. The analysis of the $(11/2^-)$ state was conducted utilizing both the 1095-keV and 252-keV branches, leading to the lifetime result of $\tau_{11/2-} = 37(1)$ ps for the 1095-keV branch and $\tau_{11/2-} = 37(^{+1}_{-2})$ ps for the 252-keV branch, where the error is statistical only.

To evaluate additional systematic errors, the direct population of the $(15/2^+)$ state was varied and the effect on the lifetime of the $(11/2^-)$ state was examined. Since the direct population of the $(13/2^-)$ state was consistent with zero within uncertainty, it was determined that variation of the $(15/2^+)$ direct population was the dominant contributor to systematic uncertainties. Due to feeding effects from the population of the $(15/2^+)$ and $(13/2^-)$ states, we determined a $(^{+1}_{-4})_{syst}$ ps systematic uncertainty for the mean lifetime of the $(11/2^-)$ state. Similarly, the lifetime of the $(15/2^+)$ state was varied within our simulations and its effects on the observed lifetime of the $(11/2^-)$ state were evaluated. From feeding effects due to the lifetimes of the $(15/2^+)$ and $(13/2^-)$ states we found an additional systematic uncertainty of $(^{+1}_{-3})_{syst}$ ps to our result.

The systematic uncertainties were added in quadrature with the statistical uncertainties and are

presented below as a single, combined error to our lifetime results. The analysis of the 1095-keV branch resulted in a lifetime of $\tau_{11/2-} = 37(^{+2}_{-5})$ ps. The analysis of the 252-keV branch yields the same result for the 1095-keV branch with a lifetime of $\tau_{11/2-} = 37(^{+2}_{-5})$ ps. The agreement of the lifetimes from the evaluation of both the 252-keV and 1095-keV branches strengthened confidence in the analysis. For the purpose of this study we adopt a mean lifetime $\tau_{11/2-} = 37(^{+2}_{-5})$ ps for the $(11/2^-)$ state in ^{39}Ca. Using the lifetime above, the absolute branching ratio of the $(11/2^-) \rightarrow 7/2^-$ transition $b_{abs} = 70(2)\%$, and the gamma-ray energy $E_\gamma = 1095(4)$ keV, we determined the reduced transition strength $B(\mathrm{E2};(11/2^-) \rightarrow 7/2^-)$=9.8$(^{+14}_{-6})$ e^{2}fm^4.

3.3.3 ^{39}K Target-only Data

The analysis method used for ^{39}Ca was tested and validated by studying the reference data for the mirror nucleus ^{39}K, for which the ^{9}Be(^{42}Sc, ^{39}K)X reaction was employed. The gamma-ray spectrum for the target-only data is presented in Fig. 3.14 with the analogue cascade of transitions originating from the $15/2^+$ state noted with arrows, as observed in ^{39}Ca. The relevant level scheme of ^{39}K is provided in Fig. 3.10 and the analogue transitions in ^{39}K that are the focus of this work are highlighted in red and blue.

In Fig. 3.14 one may notice transition peaks near 900 keV and 1400 keV which are not labeled; we have chosen to omit these transitions from our analysis because the associated states do not significantly populate the $11/2^-$ state, as explained below. The $7/2^-_4$ state at 5010 keV was populated in our experiment and decays via two branches; the prominent branch emits a 883-keV gamma ray to the $7/2^-_2$ state at 4127 keV which, in turn, decays by cascade to the $7/2^-_1$ state at 2814 keV via emission of a 1312-keV gamma ray. The minor branch of the $7/2^-_4$ state decays by emission of a 1412-keV gamma ray to the $9/2^-_1$ state at 3597 keV with an absolute branching ratio of $b_{abs} = 23(4)\%$. Therefore, decays from the $7/2^-_4$ state bypass the $11/2^-_1$ state of interest and have no effect on the lifetime measurement of the $11/2^-_1$ state. We also observed transitions from the $9/2^-_2$ state at 4520 keV whose largest branch leads to the $9/2^-_1$ state at 3597 keV by emission of a 923-keV gamma ray. The $9/2^-_2$ state also has a minor branch which feeds the $11/2^-_1$ state at 3944 keV by emission of a 576-keV gamma ray which we do not observe in our data. The absolute

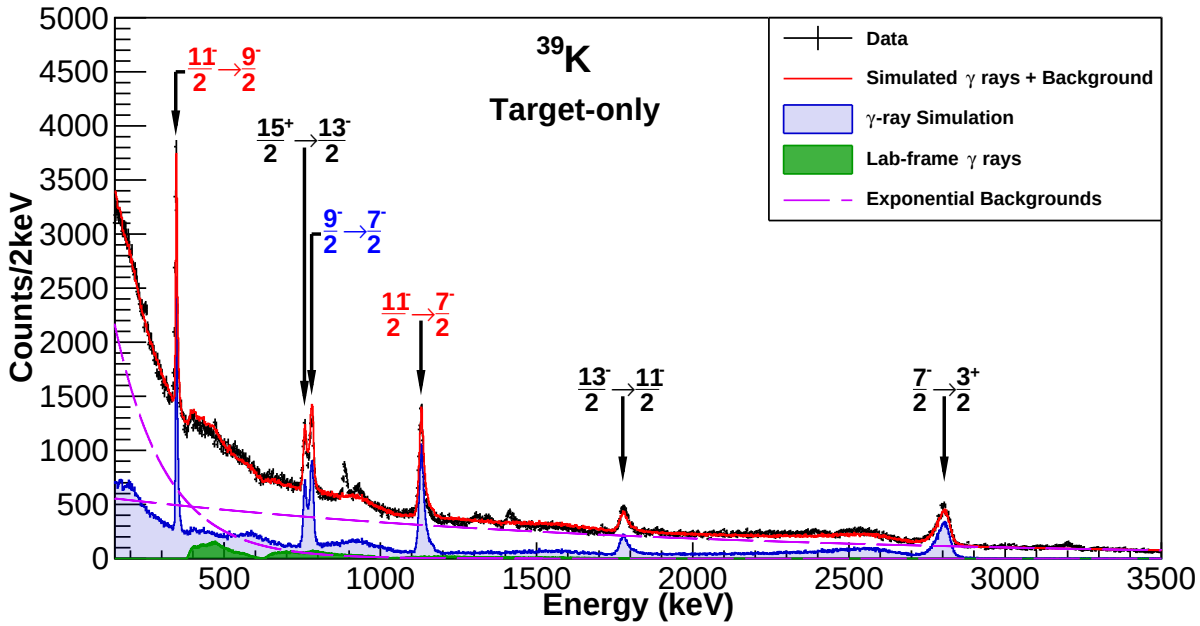

Figure 3.14 Doppler-shift corrected gamma-ray spectrum for ^{39}K from the target-only measurement. Transitions from the $(11/2^-)$ state are labeled in red, while transitions from the $(9/2^-)$ state are labeled in blue [88]. Reprinted figure with permission from A. Sanchez *et al.*, Phys. Rev. C, vol. 110, p. 024322 (2024). Copyright (2024) by the American Physical Society.

branching ratio for this $9/2^-_2 \rightarrow 11/2^-_1$ transition is weak (b_{abs} = 9.2(8)% [45]) and the state has a short lifetime of $\tau_{9/2^-_2}$ = 0.14(4) ps [45], from which we conclude that feeding effects to the $11/2^-_1$ state from the $9/2^-_2$ state are negligible, if any. Thus, we acknowledge the existence of these transitions in our data while determining that their influence on our state of interest is negligible and can therefore be excluded from the analysis, allowing us to focus on the mirror cascade in ^{39}K as shown in Fig. 3.10.

When comparing the ^{39}Ca and ^{39}K target-only spectra, the similarity of decay schemes is apparent, but one should note a 300-keV increase in the energy of the $13/2^-$ state in ^{39}K. This shift displaces the $15/2^+ \rightarrow 13/2^-$ transition from 1030 keV in ^{39}Ca to an energy of 757 keV in ^{39}K, placing it in close proximity to the 783-keV peak from the $9/2^- \rightarrow 7/2^-$ transition. As with our observations of the fast components of the higher-lying transitions in ^{39}Ca, the lifetime of the $13/2^-$ state in ^{39}K is short ($\tau_{13/2^-}$ = 0.27(7) ps [45]) and the direct population is small (2(2)%) and therefore the $13/2^-$ state has a negligible feeding effect on the $11/2^-$ state.

As was explained for ^{39}Ca, the intensities of the observed transitions in ^{39}K were determined from the ^{152}Eu source data. Using the intensities, a relative branching ratio for the $11/2^-$ state of $b_{rel} = 52(4)$ was determined by the intensity of the 347-keV peak with respect to the intensity of the major branch at 1130 keV with $b_{rel} = 100(4)$. This result was found to agree with the literature value of the relative branching ratio $b_{rel} = 57.3(13)$ [45].

The analysis of the target-only data for ^{39}K was accomplished by determining the direct population fractions of the populated states via the method explained for ^{39}Ca. To the $15/2^+$ state at 6475 keV, we assigned a population of 21(3)%. This state decays via emission of a 757-keV gamma ray to the $13/2^-$ state. The $13/2^-$ state at 5718 keV has a direct population of 2(2)% and decays to the $11/2^-$ state via emission of a 1774-keV gamma ray. Again, we observed the strongest population to the $11/2^-$ state at 3944 keV, for which we calculated a direct population of 49(7)%. This state decays by emission of either a 347-keV gamma ray to the $9/2^-$ state or an 1130-keV gamma ray to the $7/2^-$ state. The $9/2^-$ state at 3597 keV was observed to be much more weakly populated in the ^{9}Be(^{42}Sc, ^{39}K)X reaction with a direct population of 3(2)%, decaying by emission of a 783-keV gamma ray to the $7/2^-$ state. Finally, for the 2814-keV $7/2^-$ state, we found a direct population of 26(10)% with ambiguities due to feeding from states not included in this study.

3.3.4 ^{39}K RDM Analysis

The spectra for ^{39}K taken with the 1 and 0-mm separation distance are provided in Fig. 3.15 and Fig. 3.16, respectively. The decrease in the target-degrader ratio, compared to the case of ^{39}Ca, is evident in the $13/2^- \rightarrow 11/2^-$ transition measured with the 1-mm distance as shown in Fig. 3.16, where one can observe comparable yields for the fast and slow components. As was explained for ^{39}Ca, the effective lifetime of the short-lived $13/2^-$ state in ^{39}K was used to determine the ratio of reactions on target to reactions on degrader, which was found to be 2.3(4) : 1. By considering the rigidity setting of the S800 spectrograph, the reduced ratio was attributed to an effect of the momentum acceptance setting, which was sufficient to accept nearly all of the ^{39}Ca recoil nuclei, but was only able to cover the lower-momentum components of ^{39}K. Since multi-nucleon (-2p-1n) removal reactions of ^{42}Sc are used to populate ^{39}K, the final momentum of ^{39}K depends largely

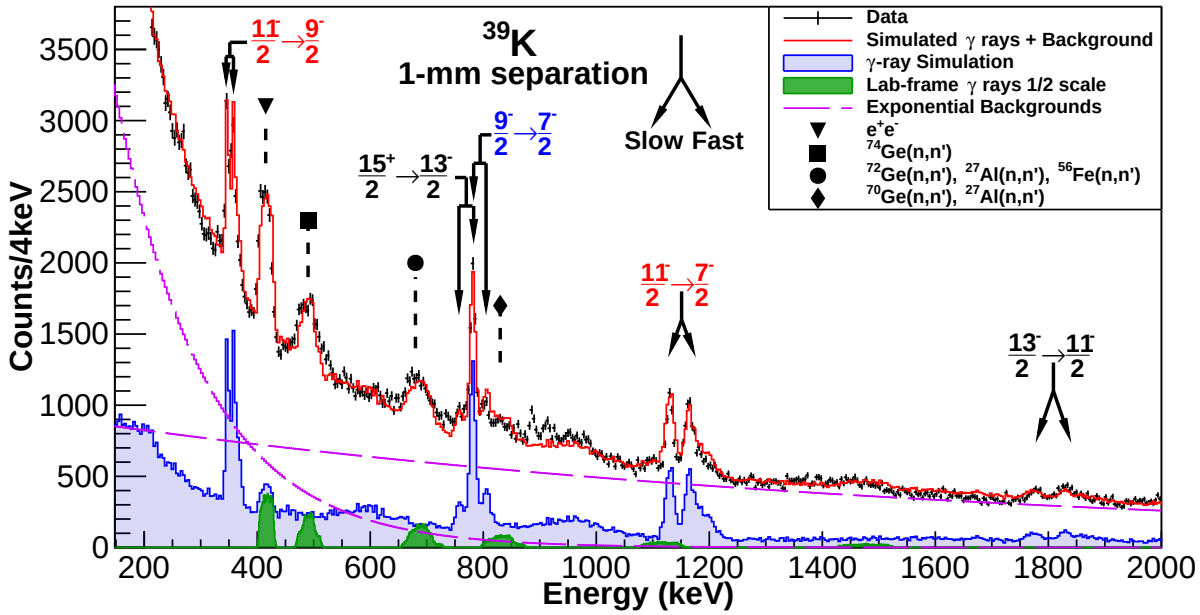

Figure 3.15 Doppler-shift corrected gamma-ray spectrum for the 1-mm target-degrader separation setting in ^{39}K. The spectrum has been gated between $\theta = 29°$ and $\theta = 46°$ to improve sensitivity to Doppler shifts. Transitions from the $(11/2^-)$ state are labeled in red, while transitions from the $(9/2^-)$ state are labeled in blue. Laboratory-frame background gamma rays are shown in green and downscaled by a factor of 2 [88]. Reprinted figure with permission from A. Sanchez *et al.*, Phys. Rev. C, vol. 110, p. 024322 (2024). Copyright (2024) by the American Physical Society.

on the reaction points, yielding low-momentum components when reactions occur in the degrader. The rigidity setting used in this experiment therefore resulted in the decreased target-degrader ratio. These features are incorporated in the simulation and the target-degrader ratio should be considered as an effective parameter used for the lifetime analysis.

Lifetime analyses of the ^{39}K states were performed using the adopted lifetime values for higher-lying states [45] combined with the direct population of the excited states determined from the target-only data. By varying the target-degrader ratio and observing the effect on the lifetime of the $11/2^-$ state we determined that a systematic error of $(\pm 2)_{syst}$ ps contributes to the overall uncertainty of the lifetime measurement of the $11/2^-$ state. As a result, a lifetime of $\tau_{11/2^-} = 13(2)$ ps was determined for the $11/2^-$ state at 3944 keV from fits to the 1130-keV and 347-keV peaks in both the 0- and 1-mm spectra. The statistical and systematic uncertainties were added in quadrature for the result above and our result agrees with the adopted value of 12.3(14)

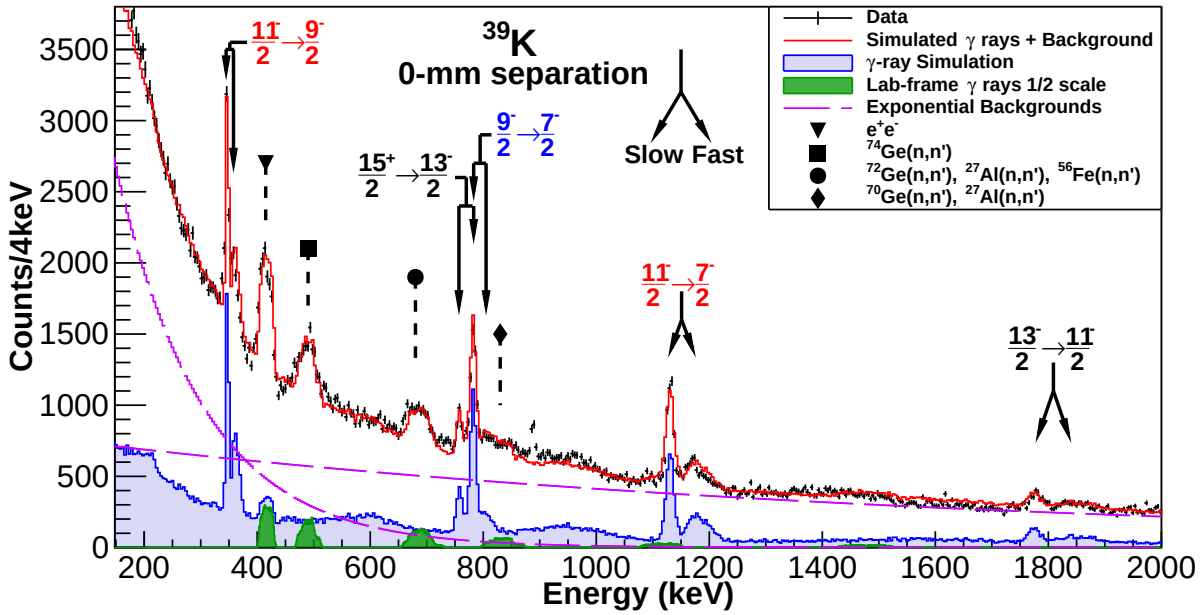

Figure 3.16 Doppler-corrected gamma-ray spectrum for the ^{39}K 0-mm target-degrader separation. The spectrum has been gated between $\theta = 29°$ and $\theta = 46°$ to improve sensitivity to Doppler shifts. Transitions from the $(11/2^-)$ state are labeled in red, while transitions from the $(9/2^-)$ state are labeled in blue. Laboratory-frame background gamma rays are shown in green and downscaled by a factor of 2 [88]. Reprinted figure with permission from A. Sanchez *et al.*, Phys. Rev. C, vol. 110, p. 024322 (2024). Copyright (2024) by the American Physical Society.

ps. The experimental values for the absolute branching ratio of the 1130(4)-keV branch found from the target-only data $b_{abs} = 66(2)\%$ and the lifetime above give the reduced transition strength of $B(\mathrm{E2}; 11/2^- \rightarrow 7/2^-) = 22.4(35)$ e^{2}fm^4 as presented in the following section.

CHAPTER 4

DISCUSSION OF RESULTS

Having determined the reduced transition strengths for the $11/2^- \rightarrow 7/2^-$ E2 transitions in the $A = 39$ system we now discuss their relation to matrix elements M_p and M_n and compare the results to the data systems and shell-model calculations. From comparison of the current results for the $A = 39$ system to the adopted values for other neutron-deficient calcium isotopes, we observe an increasing ratio M_n/M_p as we move from $A = 36$ toward $A = 40$, implying an increased degree of neutron excitation. We then compare the results of this study to shell-model calculations for the $A = 38$ and $A = 39$ systems using three effective interactions common to this region of the nuclear chart. The shell-model calculations also point toward the importance of both proton and neutron cross-shell configurations for $A = 39$ system, as opposed to the the $A = 38$ system which appears to be largely dominated by proton cross-shell excitations.

4.1 Experimental Data and Systematics

The experimental mean lifetimes τ, the absolute branching ratios b_{abs} for the $11/2^-$ states, and the gamma-ray energies E_γ given in the previous sections were used to calculate the $B(\mathrm{E2};11/2^- \rightarrow 7/2^-)$ values for ^{39}Ca and ^{39}K as presented in Table 4.1. Also presented in Table 4.1 are the adopted $B(\mathrm{E2})$ values and their related matrix elements for the $A = 38$ system [43, 44]. The $B(\mathrm{E2})$ values were converted to the absolute value of proton matrix elements M_p according to Eqn. 4.1 and are presented in Table 4.1 for the $A = 38$ system with $J_i = 2$ and the $A = 39$ system with $J_i = 11/2$.

$$M_p = \sqrt{B(\mathrm{E2}; J_i \rightarrow J_f) \times (2J_i + 1)} \tag{4.1}$$

As described in Sect. 1.1, under the assumption of isospin conservation, the neutron matrix elements M_n of ^{39}Ca and ^{38}Ca are obtained from the proton matrix elements of the mirror nuclei ^{39}K and ^{38}Ar, respectively, via Eqn. 1.7. For the present work, the equivalencies are $M_n(^{39}\mathrm{Ca}) = M_p(^{39}\mathrm{K})$ and $M_n(^{38}\mathrm{Ca}) = M_p(^{38}\mathrm{Ar})$. Here we should note that, to avoid redundancies, the M_n and M_n/M_p values have been omitted from the table for the $T_z \geq 0$ nuclei.

Table 4.1 The present results of B(E2), proton (M_p) and neutron (M_n) matrix elements for the $11/2^- \rightarrow 7/2^-$ transitions in the $A = 39$ system are compared to adopted values for the $2^+ \rightarrow 0^+$ transitions in the $A = 38$ system [43, 44]. The M_n values and M_n/M_p ratios are presented only for ^{39}Ca and ^{38}Ca and corresponding values in mirrors ^{39}K and ^{38}Ar, respectively, are omitted to avoid redundancy. The table has been adapted from Ref. [88].

	B(E2) (e^2fm^4)	M_p (efm^2)	M_n (efm^2)	M_n/M_p
^{39}Ca	$9.8(^{+14}_{-6})$	$10.8(^{+8}_{-4})$	16.4(13)	1.5(2)
^{39}K	22.4(35)	16.4(13)	–	–

As with the $A = 38$ system, the $M_p(T_z)$ values for the $A = 39$ mirror nuclei increase as a function of increasing T_z, which results in $M_n > M_p$ for ^{39}Ca, as is the case for the $A = 38$ system. This common feature of the $A = 38$ and $A = 39$ systems appears to go against the trends set by the $A = 22, 26, 30, 34$, and 42 systems observed in Fig. 1.6 and implies that the $A = 39$ and $A = 38$ mirror nuclei have a negative isovector matrix element M_1 [51, 40]. The ratios M_n/M_p observed among neutron-deficient calcium isotopes are found to be 0.8(1) and 1.1(1) for the $2^+ \rightarrow 0^+$ transitions of ^{36}Ca and ^{38}Ca [49], respectively, and 1.5(2) for the $11/2^- \rightarrow 7/2^-$ transition of ^{39}Ca, indicating an increased degree of neutron excitations toward $N = Z$.

In a broader view of the systematics, the M_n/M_p ratios for the $2^+ \rightarrow 0^+$ transitions in the neutron deficient calcium isotopes near $N = Z$ are plotted in Fig. 4.1 along with the ratio for the analog $11/2^- \rightarrow 7/2^-$ transition for the $A = 39$ system studied in this work. The N/Z expectation from the homogeneous collective model is also provided, as was similarly provided by Bernstein *et al.* in Ref. [47] and displayed in this work as Fig. 1.7 in Sect. 1.2. Also plotted, is the expectation for single-closed shell (SCS) mirror nuclei from the ratio of effective charges $e_p/e_n = 3.0(4)$, as derived in Eqns. 1.9 and 1.10.

In Fig. 4.1 we observe agreement between the collective model assumption N/Z and the M_n/M_p ratio for $A = 36$ system of calcium and sulfur [49, 48], suggesting a large degree of collectivity for this system and a positive isovector matrix element M_1. As one adds neutrons to the system, a divergence from the N/Z assumption is observed as one approaches ^{40}Ca. Recall that the ratio

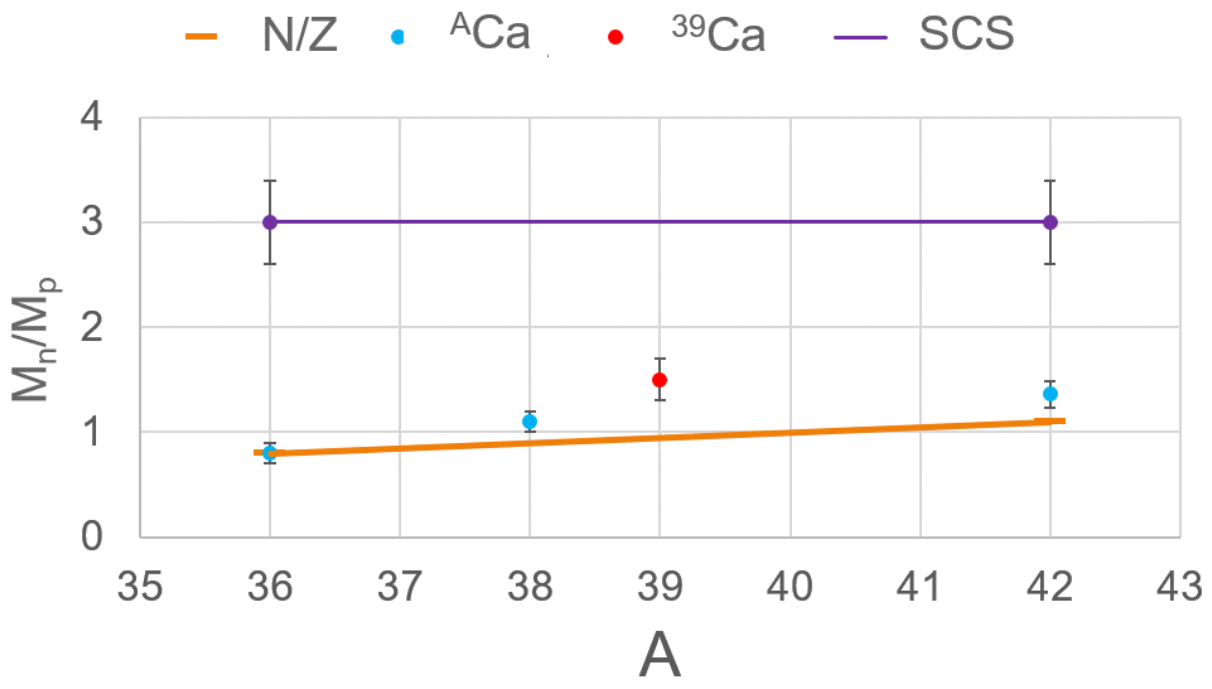

Figure 4.1 Ratios M_n/M_p for calcium isotopes near $N = Z$ compared to the homogeneous collective model (N/Z) and the single-closed shell (SCS) esitmation $e_p/e_n = 3.0(4)$. The figure shows an enhanced M_p when compared to the SCS expectation. The $A = 36$ ratio was obtained from Refs. [49, 48]. The $A = 38$ ratio is from Refs. [43, 44]. The $A = 39$ ratio is from this work [88]. And Ref. [40] provides the $A = 42$ ratio.

M_n/M_p is independent of the $T_z = 0$ data point; this is especially relevant for $A = 38$ system [43, 44] as recent evaluation has enlarged the error bars of the ^{38}K data point. We observe in Fig. 4.1 that the M_n/M_p ratio for the calcium isotopic chain begins to diverge from N/Z at the $A = 38$ system. This work has further illustrated this divergence with the addition of the $A = 39$ system [88]. Since ^{40}Ca is self-conjugate (it is its own magic nucleus), we expect $M_n/M_p = 1$. However, from Fig. 1.7 in Sect. 1.2, we see that the ratios tend to increase drastically for doubly magic nuclei such as ^{48}Ca and ^{208}Pb, diverging from the trend set by the single closed shell nuclei. This implies that ^{40}Ca similarly may have a ratio much larger than the N/Z assumption, though the methods of probing this neutron matrix element are outside the scope of this work. Upon filling of the *sd* shell, there is a decrease in the M_n/M_p ratio as observed in the $A = 42$ system [40]. Further, Fig. 4.1 suggests that ^{39}Ca displays more collectivity than one would expect when compared to the SCS expectation, making its M_n/M_p ratio similar to the other neutron deficient Ca isotopes displayed in the figure.

4.2 Shell Model Calculations

In the following sections we will examine the effective interactions utilized to replicate the B(E2) and proton matrix elements that are the focus of this work. We will begin with descriptions of the shell-model effective interactions involved and provide the context in which these interactions were developed. Following the brief description of each interaction, we will then consider the results of the calculations for the energies of the negative parity states examined in this work. We then move on to the results of the B(E2) and M_p calculations from each interaction, as well as the predicted ratios M_n/M_p for the$A = 39$ system, and in the last section we will discuss the same calculations for the $A = 38$ system.

4.3 Effective Interactions Employed in this Work

Three effective interactions common to this mass region were employed to replicate the experimental data: FSU [94], ZBM2 [95], and ZBM2m [96]. These interactions average the forces acting between nucleons allowing for more manageable calculations when compared to ab initio models. The choice of which interactions to use is highly dependent on the model space for orbitals most likely to be occupied by the particle configurations for the nuclei in question. The parameters within the effective interactions are often derived from fits to experimental data such as binding energies, excitation energies, and other observables.

The FSU [94] effective interaction was developed from a modified version of the WBP [97] interaction and adopted the WBP model space ($spsdfp$) as a starting point. This interaction assumes isospin invarience while allowing Coulomb corrections to the binding energies. Lower sp orbital single-particle energies (SPEs) and two-body matrix elements (TBMEs) were taken from the WBP interaction while the TBMEs for the sd shell were adopted from the USDB [38] Hamiltonian. The $sd - fp$ cross-shell matrix elements required modification of the monopole and isospin strengths while the remaining multipoles for the upper shells of the model space were fit to data with the GXPF1A [98] Hamiltonian as a starting framework. Special attention was paid to data from intruder states sensitive to the $p - sd$ shell gap, negative parity states sensitive to particle excitation from sd to fp shells, neutron-rich cross-shell nuclei with $Z < 20$ and $N > 20$, and

fp shell nuclei of $Z \geq 20$ and $N \geq 21$. Based on pure n-particle n-hole configurations of either $0\hbar\omega$, $1\hbar\omega$, and $2\hbar\omega$ excitations in the $spsdpf$ model space, the FSU interaction provides accurate predictions of level energies for nuclei in the sd-shell region, including neutron-rich nuclei in the island of inversion [94].

The ZBM2 [95] effective interaction employs a smaller model space of the $2s_{1/2}$, $1d_{3/2}$, $1f_{7/2}$, and $2p_{3/2}$ orbitals while allowing all configurations within this space. The ZBM2 interaction was developed to reproduce the odd-even charge radii staggering in the ^{40}Ca to ^{48}Ca isotopic chain while simultaneously replicating the parabolic dependence on mass A of the low-lying excited-state energies [95]. The TBMEs from Ref. [99], which are defined with respect to a ^{16}O core, were adopted as a starting point. The SPEs were modified to reproduce the ^{29}Si spectrum and the $sd-fp$ monopoles from Ref. [99] were adjusted to replicate the masses of the neutron rich isotopic chains then returned to reproduce the ^{40}Ca shell gap and the spectra of ^{39}K and ^{41}Ca [95]. Because the ZBM2 interaction does not rely on pure particle-hole states we are able to get a more detailed picture of the mixed configurations underlying the states being studied.

In an attempt to have theoretical calculations which are in closer agreement to data, we also used a modified ZBM2 interaction [96], denoted as ZBM2m. This interaction was developed to better describe the charge radius of the ^{38}K^m isomer and reproduce the correct order of the 3^+ ground state and 0^+ isomeric state of ^{38}K [96]. While the ZBM2 interaction provided a fair description of the low lying 0^+ and 2^+ states in ^{40}Ca, it could not properly replicate the ordering of the ground and isomeric states in ^{38}K mentioned above and predicted a 3^+ excited state at nearly 500 keV instead of the 0 keV ground state which has been observed. For the ZBM2m interaction, the $T = 1$ and $T = 0$ strengths were adjusted within the monopole Hamiltonian, with one coefficient fixing the poistion of the configurations of a given isospin T and another coefficient fixing the the position of configurations dependent on the particle number involved [96]. As with the ZBM2 interaction, the ZBM2m interaction utilizes the $sdfp$ model space while allowing configuration mixing within the space.

4.3.1 Shell Model Predictions of ^{39}Ca Level Energies

The calculated energy level diagrams for the negative parity states in ^{39}Ca which are the subject of this work are provided in Fig. 4.2. The results from the three effective interaction calculations (FSU, ZBM2, and ZBM2m) are compared to the experimental energies (Exp) observed in the gamma-ray spectra presented in Sect. 3.3.

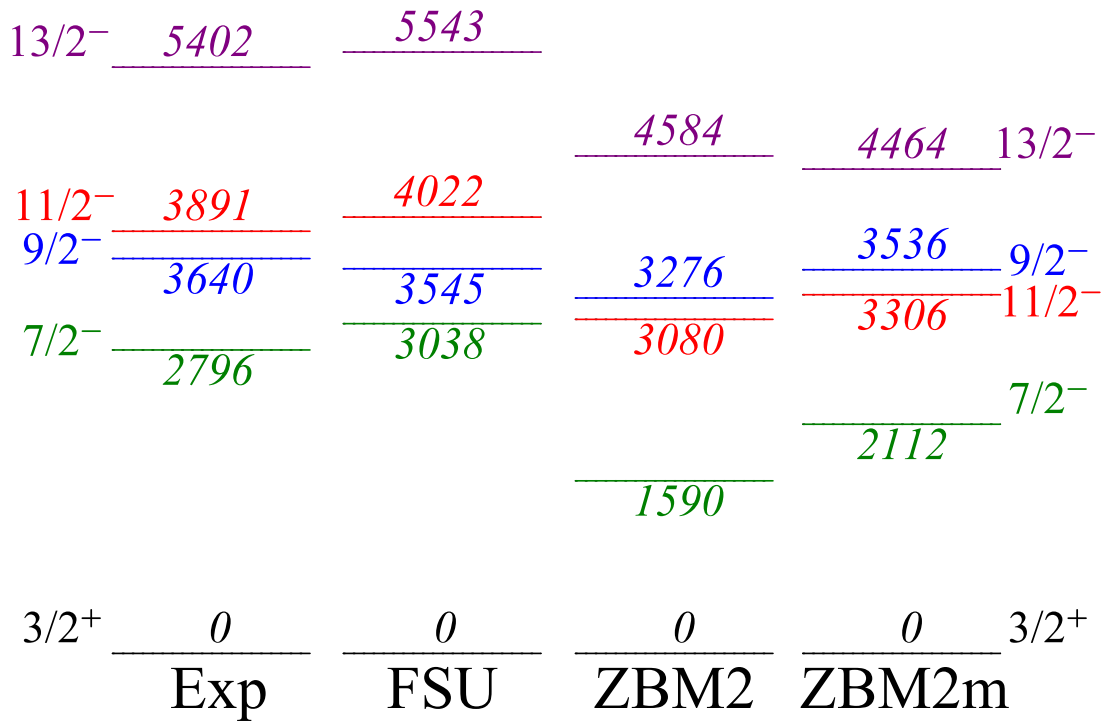

Figure 4.2 Level energies of the lowest $7/2^-$, $9/2^-$, $11/2^-$, and $13/2^-$ states of ^{39}Ca from experiment (Exp) compared to shell-model calculations with the FSU [94], ZBM2 [95], and ZBM2m [96] effective interactions [88]. Reprinted figure with permission from A. Sanchez *et al.*, Phys. Rev. C, vol. 110, p. 024322 (2024). Copyright (2024) by the American Physical Society.

One will notice that the FSU calculations for all the observed levels in the ^{39}Ca spectra are in good agreement with the experimental level scheme, having replicated the correct J^π ordering of each state correctly and predicting the energies of each state accurately to within approximately 200 keV at most, and often much closer. Most importantly for this work, the $11/2^-$ state is predicted accurately to within 30 keV of the experimental data while the $7/2^-$ state shows a 200 keV discrepancy from the data. The FSU calculation predicts an energy difference between the $11/2^-$ and $7/2^-$ states of 984 keV which is in reasonable agreement with the gamma-ray energy of

1095 keV observed in the ^{39}Ca spectra.

The ZBM2 calculations do not reproduce the levels in ^{39}Ca as well as the FSU calculation. Working from the ground state up, we first notice a $7/2^-$ state that is approximately 1.2 MeV lower than the experimental data. Generally, level energy predictions that agree with data to within a couple hundred keV are considered "good" calculations; if this is an acceptable margin of error then the ZBM2 prediction of the $7/2^-$ state with energy 1.2 MeV below the data does not fall into that category. Moving up in energy we next encounter the $11/2^-$ state at an energy 800 keV below the experimental data, this significant decrease in the $11/2^-$ energy with respect to the data results in an inversion of the $9/2^-$ and $11/2^-$ states which is not supported by observation. The ZBM2 calculation predicts the energy of the $9/2^-$ state best compared to other levels with a difference between data and calculation under 500 keV. The $13/2^-$ state, whose energy value is not of particular importance to this work, does also suffer from a 800 keV descrepency with the data. Overall, the ZMB2 calculation appears to under-predict excitation energies for every state while predicting a gamma-ray energy of 1490 keV, which is not representative of the 1095 keV gamma ray associated with the $11/2^- \rightarrow 7/2^-$ transition that is the focus of this work.

For the ZBM2m calculation we again begin with the lowest excited state and work up the level diagram. While the $7/2^-$ state prediction is approximately 600 keV lower than the experimental data, the difference between the $11/2^-$ and $7/2^-$ states is 1194 keV which, like the FSU calculation, is in reasonable agreement with the data. As with the ZBM2 interaction, the ZBM2m interaction also under predicts the energy of the $11/2^-$ state by approximately 600 keV, again resulting in the inversion of the $9/2^-$ and $11/2^-$ states. The $9/2^-$ state is well replicated, as it is with each interaction used in this work, predicting an energy about 100 keV lower than the experimental data. Finally, the $13/2^-$ state is calculated to have an energy of approximately 1 MeV lower than the data, but as was stated for the ZBM2 calculation, this level energy is not tied closely to the $11/2^- \rightarrow 7/2^-$ E2 transition which is the focus of this work.

Overall, while the FSU interaction best reproduces the absolute level energies, both the FSU and ZBM2m interactions well replicate the $11/2^- \rightarrow 7/2^-$ transition energy. While the FSU interaction

obtains close agreement for this transition energy by predicting the absolute energies of the two states within suitable margins, the ZBM2m obtains similar agreement through a down scaling of both the $11/2^-$ and $7/2^-$ energies resulting in a transition energy that is in good agreement by the 200 keV metric discussed above.

4.3.2 B(E2) and M_p for the $A = 39$ system

We now employ Eqn. 1.4 to calculate the reduced transition strengths $B(\mathrm{E2};11/2^- \rightarrow 7/2^-)$ for ^{39}Ca and ^{39}K based on our determination of the experimental mean lifetimes τ, the absolute branching ratios b_{abs} for the $11/2^-$ states, and the gamma-ray energies E_γ provided in Sect. 3.3. The B(E2) determined from this work are presented in Table 4.2 in the row labeled "Exp". The FSU, ZBM2, and ZBM2m effective interactions were also used to predict the B(E2) values for the E2 transitions in both ^{39}Ca and ^{39}K and the values are presented in Table 4.2 accordingly with the interaction name.

Table 4.2 The present results of B(E2), proton (M_p) and neutron (M_n) matrix elements for the $11/2^- \rightarrow 7/2^-$ transitions in the $A = 39$ system [88]. The M_n values and M_n/M_p ratios are presented only for ^{39}Ca and corresponding values in mirror ^{39}K are omitted to avoid redundancy [88]. Reprinted table with permission from A. Sanchez *et al.*, Phys. Rev. C, vol. 110, p. 024322 (2024). Copyright (2024) by the American Physical Society.

		B(E2) (e^2fm^4)	M_p (efm^2)	M_n (efm^2)	M_n/M_p
^{39}Ca	Exp	$9.8(^{+14}_{-6})$	$10.8(^{+8}_{-4})$	16.4(13)	1.5(2)
	FSU	3.4	6.4	11.4	1.8
	ZBM2	20.6	15.7	18.0	1.1
	ZBM2m	13.7	12.8	14.9	1.2
^{39}K	Exp	22.4(35)	16.4(13)	–	–
	FSU	10.8	11.4	–	–
	ZBM2	27.0	18.0	–	–
	ZBM2m	18.5	14.9	–	–

Upon inspection, we find that the FSU calculation tends to under predict the B(E2) for ^{39}Ca and ^{39}K. For the E2 transition in ^{39}Ca, the FSU calculation predicts a B(E2)= 3.4 e^2fm^4, which is approximately 35% of the experimental result determined by this work. For ^{39}K, the FSU interaction predicts a value that is closer to the experimental value with B(E2)= 10.8 e^2fm^4 for

the analog $11/2^- \rightarrow 7/2^-$ transition, which is approximately 50% of the value determined in this work.

The ZBM2 prediction for the ^{39}Ca transition is B(E2)= 20.6 e^{2}fm^4 which is over twice the experimental value, making a stark contrast between its utility for this work compared to the FSU and ZBM2m interactions. For ^{39}K, the ZMB2 calculation of B(E2)= 27.0 e^{2}fm^4 is a much more accurate prediction than what was calculated for ^{39}Ca being only 20% larger than the experimental value. This is unsurprising considering that the parameters which were adjusted from WBP to make ZBM2 were modified to fit the ^{39}K spectra, as described in Sect. 4.2.

Out of the three effective interactions, the ZBM2m most accurately reproduces the ^{39}Ca E2 transition strength with B(E2)= 13.7 e^{2}fm^4 which is approximately 40% larger than the experimental value but is the best prediction out of the three interactions chosen for this work. The ZBM2m also best replicates the analog transition in ^{39}K with B(E2)= 18.5 e^{2}fm^4, 17% lower than the experimental result. This is a bit unexpected considering that the ZBM2m interaction was tailored to replicate ^{38}K^m, as discussed in Sect. 4.2.

For a more detailed description of the origin of the differences among the interactions used for this work, the bare matrix elements A_p and A_n used in the calculations of M_p are examined below. The effective interactions use Eqn. 1.5 to calculate M_p using the bare matrix elements and the effective charges. For each calculation, the effective charges of $e_p = 1.36$ and $e_n = 0.45$ [42] were used as Dronchi *et al*. [49] used for the ZBM2 calculations of ^{36,38}Ca. One should also note that the effective charges employed here are comparable to the charges $e_p = 1.31$ and $e_n = 0.46$ which were used with the SDPF-U-MIX Hamiltonian for calculations of ^{36}Ca and ^{36}S [48]. Therefore, the calculations presently used should be on equal footing with respect to the choice of effective charges for calculations of other neutron-deficient Ca isotopes.

The calculated values of A_p and A_n used in the shell-model calculations for ^{39}Ca are provided in Table 4.3; as discussed in Sect. 1.1, these correspond to the matrix elements calculated with the free-nucleon charges $e_n = 0$ and $e_p = 1$. The bare matrix elements A_p and A_n are scaled by the effective charges mentioned above and summed to calculate the proton matrix elements provided

in Table 4.2. By examining A_p and A_n for the ZBM2 and ZBM2m interactions, we notice that both values are larger than those calculated by the FSU interaction and both predict relatively even distributions of proton and neutron contributions. Conversely, the FSU interaction predicts a much larger neutron contribution to the M_p.

As described in Sect. 1.1, under the assumption of isospin conservation, the neutron matrix elements M_n of ^{39}Ca are obtained from the proton matrix elements of the mirror nuclei ^{39}K via Eqn. 1.7. For the $A = 39$ system, the equivalency is $M_n(^{39}\text{Ca}) = M_p(^{39}\text{K})$. Here we should note that, to avoid redundancies, the M_n and M_n/M_p values for the $T_z > 0$ nucleus have been omitted from Table 4.2.

Table 4.3 The calculated values of the bare proton (A_p) and neutron (A_n) matrix elements for the $11/2^- \rightarrow 7/2^-$ transition of ^{39}Ca from shell-model calculations with the FSU [94], ZBM2 [95], and ZBM2m [96] effective interactions. The table has been adapted from Ref. [88].

		A_p (efm^2)	A_n (efm^2)
^{39}Ca ($11/2^- \rightarrow 7/2^-$)	FSU	2.14	7.65
	ZBM2	8.06	10.57
	ZBM2m	6.51	8.81

In examining the predicted matrix elements for the $A = 39$ system we note that all the $M_p(T_z)$ calculations increase as a function of increasing T_z, which replicates the in $M_n/M_p > 1$ feature observed in the ^{39}Ca data. Referring back to Table 4.2, the FSU calculation replicates the M_p value of ^{39}Ca to within 40% of the M_p derived from the data. Similarly, the FSU interaction replicates the M_p of ^{39}K to within 30% of the experimental value. The ZBM2 calculation for the M_p of ^{39}Ca is approximately 40% larger than the experimental value with a calculated $M_p = 15.7$ efm^2. For ^{39}K, the ZMB2 interaction provides the best prediction of the proton matrix element with $M_p = 18.0$ efm^2 which is within 10% of the experimental value. Again, the ZBM2m interaction appears to best replicate the results of the ^{39}Ca values with $M_p = 12.8$ efm^2, predicting the proton matrix element value to within 19% of the experimental value. And for ^{39}K, the ZBM2m interaction similarly reproduces M_p to within 10% Therefore, when we examine the ratio M_n/M_p and see that both the FSU and ZBM2m calculations are just outside the experimental uncertainty, one must also

take into account that the ZBM2m calculations predicted the individual M_p values more accurately than the FSU calculation.

Table 4.4 The numbers of protons (Δ_p) and neutrons (Δ_n) excited from the ($2s_{1/2}$, $1d_{3/2}$) to ($1f_{7/2}$, $2p_{3/2}$) orbitals calculated with the ZBM2 [95] and ZBM2m [96] interactions. The percentages (%) for different configurations are given for the $11/2^-$ state of ^{39}Ca (top) and for the 2^+ state of ^{38}Ca (bottom). The percentage for each of the higher-order configurations is less than 6%, and only the sum of these configurations is listed as "other" in the table. The table has been adapted from Ref. [88].

	Δ_p	Δ_n	ZBM2 (%)	ZBM2m (%)
^{39}Ca ($11/2^-$)	1	0	26	38
	0	1	21	18
	2	1	23	20
	1	2	10	9
	other		20	15

While the FSU interaction describes the $11/2^-$ state as a pure $1\hbar\omega$ configuration with approximately 60% proton and 40% neutron excitations into the fp shell, the ZBM2 and ZBM2m interactions provide a more robust picture of the state. Because the ZBM2 and ZBM2m interactions do not rely on pure particle-hole configurations, we are able to estimate the probabilities of various configurations which contribute the $11/2^-$ state. Table 4.4 provides the percentages of different configurations which compose the $11/2^-$ state in ^{39}Ca in terms of the number of protons (Δ_p) and neutrons (Δ_n) excited from the ($2s_{1/2}$, $1d_{3/2}$) to the ($1f_{7/2}$, $2p_{3/2}$) orbitals. In this notation, the ZBM2 calculation predicts lowest-order excitations with (Δ_p, Δ_n) values of (1,0) and (0,1) and probabilities of 26% and 21% respectively, which are followed by higher-order excitations of (Δ_p, Δ_n)=$(2,1)$ with 23% and $(1,2)$ with 10%. Excitation configurations with low probabilities are summed and grouped as "other" in the table and for the ZBM2 interaction these configurations account for 20% of the configurations of the $11/2^-$ state in ^{39}Ca. The ZBM2m calculation predicts a larger (Δ_p, Δ_n)=$(1,0)$ component that the ZBM2 calculation, but a further increase of A_n may be favored given that the ZBM2m interaction underestimates the M_n/M_p ratio. We see from Table 4.4 that both ZBM2 and ZBM2m calculations predict non-negligible proton and neutron contributions to the cross-shell excitations, providing an enhancement of M_p accompanied by an enhanced M_n

value for ^{39}Ca. The present work supports the ZBM2m calculations for both M_p and M_n in ^{39}Ca, emphasizing the important role of cross-shell excitations of both protons and neutrons across the $Z = N = 20$ shell gap [88].

4.3.3 B(E2) and M_p for the $A = 38$ system

Presented in Table 4.5 are the adopted $B(\text{E2},2^+ \rightarrow 0^+)$ values and their related matrix elements for the $A = 38$ system [43, 44]. We begin by comparing the adopted B(E2) values (Exp) to the values calculated with the three effective interactions. We will then examine the effective interaction predictions for M_p in the ^{38}Ca and ^{38}Ar and compare these matrix elements to those calculated from the adopted B(E2) values.

Table 4.5 The present results of reduced transition strength B(E2), proton (M_p) and neutron (M_n) matrix elements for the $2^+ \rightarrow 0^+$ transitions in the $A = 38$ system are compared to shell-model calculations with the FSU [94], ZBM2 [95], and ZBM2m [96] effective interactions. The M_n values and M_n/M_p ratios are presented only for ^{38}Ca and corresponding values in mirror ^{38}Ar are omitted to avoid redundancy [88]. Reprinted table with permission from A. Sanchez *et al.*, Phys. Rev. C, vol. 110, p. 024322 (2024). Copyright (2024) by the American Physical Society.

		B(E2) (e^2fm^4)	M_p (efm^2)	M_n (efm^2)	M_n/M_p
^{38}Ca	Exp	20.2(22)	10.0(5)	11.3(2)	1.1(1)
	FSU	2.8	3.7	11.3	3.0
	ZBM2	22.0	10.5	13.4	1.3
	ZBM2m	22.5	10.6	13.4	1.3
^{38}K	Exp	$13(^{+10}_{-6})$	$8(^{+3}_{-2})$	–	–
	FSU	11.3	7.5	–	–
	ZBM2	28.5	11.9	–	–
	ZBM2m	28.8	12.0	–	–
^{38}Ar	Exp	25.6(8)	11.3(2)	–	–
	FSU	25.5	11.3	–	–
	ZBM2	35.8	13.4	–	–
	ZBM2m	35.9	13.4	–	–

Perhaps the first and most obvious observation is that the FSU calculation dramatically under predicts the $B(\text{E2},2^+ \rightarrow 0^+)$ for ^{38}Ca with a value just 10% of the experimental value. The FSU interaction does predict the B(E2) for ^{38}Ar quite accurately with a value within the experimental

uncertainty. In fact, no other interaction gets closer to the adopted B(E2) for ^{38}Ar than the FSU interaction.

Both the ZBM2 and ZB2m interactions quite accurately predict the B(E2) values for ^{38}Ca. While the ZBM2 interaction does predict the B(E2) within the uncertainty of the adopted value, the ZBM2m prediction is only a negligibly outside the adopted uncertainty. For the cases of ^{38}Ar and ^{38}K, both the ZBM2 and ZBM2m interactions significantly over predict the B(E2) values. While the near 40% divergence from the adopted value for ^{38}Ar is significant, both the ZBM2 and ZBM2m intreacions predict a ^{38}K transition strength over twice the experimental value.

As was explained for the ^{39}Ca calculations, the proton matrix elements for the $A = 38$ system were calculated with the bare matrix elements A_n and A_p and the same effective charges used for ^{39}Ca calculations. The bare matrix elements calculated by the three effective intreacions for the $2^+ \rightarrow 0^+$ transition in ^{38}Ca are presented in Table 4.6. Here we see the similarity between the FSU calculation and assumptions made for the single-single closed shell prediction derived in Eqn. 1.10. The ZBM2 and ZBM2m calculations make near identical predictions for both A_p and A_n, showing the importance of both valence proton and neutron contributions to the matrix element M_p.

Table 4.6 The calculated values of the bare proton (A_p) and neutron (A_n) matrix elements for the $2^+ \rightarrow 0^+$ transition of ^{38}Ca (bottom) from shell-model calculations with the FSU [94], ZBM2 [95], and ZBM2m [96] effective interactions. The table has been adapted from Ref. [88].

		A_p (efm^2)	A_n (efm^2)
^{38}Ca ($2^+ \rightarrow 0^+$)	FSU	0.00	8.31
	ZBM2	5.00	8.19
	ZBM2m	5.10	8.16

In examining the proton matrix element predictions in Table 4.5, we see that the trend observed in the B(E2) calculations is propagated through to the M_p calculations. The FSU interaction again severely under predicts M_p with a value of approximately 35% of the value calculated from the adopted B(E2). The FSU calculation does predict the M_p for ^{38}Ar to within the experimental uncertainty, as it did with the B(E2) value for the same nucleus. On the other hand, both the ZBM2 and ZBM2m interactions quite accurately predict the M_p values for ^{38}Ca with no discrepancy

between the ^{38}Ca predictions and adopted values and a 20% over prediction for ^{38}Ar.

In examining the ratio M_n/M_p for the $A = 38$ system, we again see the similarity between the FSU calculation and the single-closed shell model prediction from Eqn. 1.10; that is, the FSU interaction corresponds to the prediction made by the ratio of effective charges $e_p/e_n = 3.0$. But as was stated during the derivation of Eqn. 1.1, the assumptions are naive as most nuclear configurations exist as a superposition of states which makes the single-closed shell model an unrealistic picture of an excited state. The ZBM2 and ZBM2m predictions for M_n/M_p ratio agree with each other and with the experimental data only slightly over-predicting the ratio extracted from the adopted B(E2) values. These calculations show that the FSU interaction under predicts the role of proton contributions while the ZBM2 and ZBM2 interactions appear to attribute sizable proton contributions to the 2^+ state.

We have used the ZBM2 and ZBM2m interactions to decompose the cross-shell excitations into percentage probabilities of proton (Δ_p) and neutron (Δ_n) cross-shell configurations in Table 4.7, as was done with ^{39}Ca. The table illustrates the importance of proton cross-shell contributions to the ^{38}Ca 2^+ state with nearly 30% of the state being composed of 2-proton excitations into the fp shell.

Table 4.7 The numbers of protons (Δ_p) and neutrons (Δ_n) excited from the ($2s_{1/2}$, $1d_{3/2}$) to ($1f_{7/2}$, $2p_{3/2}$) orbitals calculated with the ZBM2 [95] and ZBM2m [96] interactions. The percentages (%) for different configurations are given for the $11/2^-$ state of ^{39}Ca (top) and for the 2^+ state of ^{38}Ca (bottom). The percentage for each of the higher-order configurations is less than 6%, and only the sum of these configurations is listed as "other" in the table. This table has been adapted from Ref. [88].

	Δ_p	Δ_n	ZBM2 (%)	ZBM2m (%)
^{38}Ca (2^+)	0	0	36	39
	2	0	30	32
	1	1	11	10
	other		23	19

Finally, we note that, recent evaluation of the systematic error on the ^{38}K data point suggests that the error bars are larger than those provided in Fig. 1.6. The most recent evaluated uncertainties were used in Table 4.5 and more accurately represent the current state of the $A = 38$ system and particularly the ^{38}K data point. We should note that, given the current error, the linearity of the

M_p trend in the $A = 38$ system is not completely ruled out. However, the enhanced collectively in ^{38}Ca is still evident as indicated by $M_n/M_p = 1.1(1)$, which suggests sizable proton excitations contribute to the 2^+ state.

CHAPTER 5

CONCLUSION

Given isospin conservation in the strong force, protons and neutrons can be modeled as different states of a nucleon. Treating protons and neutrons as a single particle implies that mirror nuclei should have similar excitation energies with differences attributed to isospin non-conserving forces such as the Coulomb interaction, which acts only between protons. The similarity in spin assignment and level energies between the level diagrams of mirror nuclei is a testament to the utility of this model.

The concept of isospin formalism can be applied and tested using the information of the reduced transition strengths B(E2) obtained in mirror nuclei. The set of data can also allow for the isospin decomposition of the of the transition strengths, clarifying the relative contributions of proton and neutron excitations. Lifetime measurements of mirror states, determined by analysis of gamma-ray spectra of mirror transitions, provide model-independent determination of the reduced transition strengths B(E2). The proton matrix elements M_p are calculated from the B(E2) values and can be compared to matrix elements calculated with shell-model effective interactions which utilize effective charges.

Much progress has been made in determining the M_p values for the $2^+ \rightarrow 0^+$ transitions in even A isobars such as those presented in Fig. 1.6. The linear relation between M_p of isobaric triplets has been observed across a wide mass range, but an apparent enhancement of the M_p for ^{38}Ca deviates from the trend set by ^{38}K and ^{38}Ar, making this anomaly a point of interest. By studying a structurally similar $(11/2^-) \rightarrow 7/2^-$ quadrupole transition in the mirror nuclei ^{39}Ca and ^{39}K, and by comparing the ratios M_n/M_p, we observe that the apparent enhancement of M_p observed in ^{38}Ca is similarly observed in ^{39}Ca.

The lifetimes of the $11/2^-$ states in mirror nuclei ^{39}Ca and ^{39}K were determined by simultaneous RDM measurements. By constraining the direct populations for each of the states in the cascades, quantifying the target-to-degrader reaction ratios, and estimating the lifetimes of the higher-lying states from available data, the value $\tau_{11/2-} = 37(^{+2}_{-5})$ ps has been obtained from analysis of the

^{39}Ca gamma-ray spectra. While previous measurements were able to determine an upper bound on the lifetime of this state, this is the first work to provide a precise lifetime measurement with ample consideration given to feeding from higher states. Using the lifetime stated above, the gamma-ray energy, and the branching ratio we have determined a reduced transition strength $B(\mathrm{E2};(11/2^-) \rightarrow 7/2^-)$=9.8($^{+14}_{-6}$) e^{2}fm^4. Similarly for ^{39}K, a lifetime of $\tau_{11/2-}$ = 13(2) ps was determined utilizing the same analysis methods used for ^{39}Ca, which provides a reduced transition strength $B(\mathrm{E2}; 11/2^- \rightarrow 7/2^-)$ = 22.4(35) e^{2}fm^4. The lifetime values determined for the ^{39}K states agree with the adopted value [45] found by previous measurements and, therefore, strengthens confidence in the analysis method utilized for ^{39}Ca. Additionally, the lifetime of the $9/2^-$ state in ^{39}Ca was determined from the $9/2^- \rightarrow 7/2^-$ mixed M1+E2 transition in the same experiment and found to be $\tau_{9/2-}$ = 22($^{+6}_{-7}$) ps. This measurement agrees with the only previous measurement of this state while providing a nearly 50% reduction in the error.

The B(E2) for the $11/2^- \rightarrow 7/2^-$ transition in ^{39}Ca was used to extract the proton matrix element M_p(E2) = 10.8($^{+8}_{-4}$) efm^2 while the result from the mirror transition in ^{39}K was used to determine the neutron matrix element M_n = 16.4(13) efm^2 via the isospin decomposition for mirror transitions method developed by Bernstein *et al*. This work demonstrates the value of simultaneous lifetime measurements for mirror transitions by providing a self-consistent, model-independent determination of the reduced transition strengths and determination of both the proton and neutron matrix elements, providing a more detailed and robust picture of the transition. The present data were compared to shell-model calculations within different model spaces. Our results support calculations which allow a large percentage of cross-shell excitations, indicating that the magicity of ^{40}Ca is not robust in the transitions studied for ^{39}Ca and ^{39}K.

As an outlook for future studies, we can extend lifetime measurements in mirror nuclei in the vicinities of doubly magic nuclei in heavier mass regions. While the lower-lying states of the mirror pair ^{55}Ni and ^{55}Co near ^{56}Ni have been examined and found to display a mirror asymmetry in partial cross sections for the lowest two $3/2^-$ states and an additional asymmetry in the $1/2^+ \rightarrow 3/2^-_{1,2}$ E1 transitions [100], there remains an opportunity to examine similar mirror

E2 transitions from the $11/2^-$ states. Specifically, the lifetimes of the $(11/2^-)$ states in both ^{55}Ni and ^{55}Co remain undetermined, providing an opportunity to employ the methods developed in this work to understand neutron and proton cross-shell excitations near $N = Z = 28$. Given the proper experimental conditions, similar opportunities may arise near the doubly magic $N = Z = 50$ nucleus ^{100}Sn, where much remains unknown about excited states of the $A = 99$ isobars Sn and In.

This thesis work demonstrated the power and utility of precision lifetime measurements with rare isotope beams for determining transition strengths and matrix elements from mirror transitions. By using matrix element decomposition to determine matrix element ratios for analog transitions, such as the $11/2^- \rightarrow 7/2^-$ E2 transition in the $A = 39$ system, we can compare transition strengths of odd A nuclei to transitions in even-even and odd-odd nuclei where the $2^+ \rightarrow 0^+$ transition has been a staple measurement of nuclear structure studies. The data provided in this work have been used to test three effective interactions commonly used in the N=Z=20 region of the nuclear chart. Measurements of mirror transitions near $N = Z = 50$ may provide data useful for testing models near the proton dripline. Indeed, the methods developed in this work may be applied in any area of the nuclear chart where mirror transitions can be examined and provide alternate avenues of exploration for future structure studies.

BIBLIOGRAPHY

[1] The DOE/NSF Nuclear Science Advisory Committee. The frontiers of nuclear science, a long range plan, 2008. URL: https://arxiv.org/abs/0809.3137.

[2] Emmanuel Chang, Zohreh Davoudi, William Detmold, Arjun S. Gambhir, Kostas Orginos, Martin J. Savage, Phiala E. Shanahan, Michael L. Wagman, and Frank Winter. Scalar, Axial, and Tensor Interactions of Light Nuclei from Lattice QCD. *Phys. Rev. Lett.*, 120:152002, Apr 2018. URL: https://link.aps.org/doi/10.1103/PhysRevLett.120.152002.

[3] Takeshi Yamazaki, Ken-ichi Ishikawa, Yoshinobu Kuramashi, and Akira Ukawa. Helium nuclei, deuteron, and dineutron in 2+1 flavor lattice QCD. *Phys. Rev. D*, 86:074514, Oct 2012. URL: https://link.aps.org/doi/10.1103/PhysRevD.86.074514.

[4] M. H. Kalos. Monte carlo calculations of the ground state of three- and four-body nuclei. *Phys. Rev.*, 128:1791–1795, Nov 1962. URL: https://link.aps.org/doi/10.1103/PhysRev.128.1791.

[5] Steven C. Pieper and R. B. Wiringa. Quantum monte carlo calculations of light nuclei. *Annual Review of Nuclear and Particle Science*, 51(1):53–90, December 2001. URL: http://dx.doi.org/10.1146/annurev.nucl.51.101701.132506.

[6] Steven C. Pieper, K. Varga, and R. B. Wiringa. Quantum Monte Carlo calculations of $A = 9, 10$ nuclei. *Phys. Rev. C*, 66:044310, Oct 2002. URL: https://link.aps.org/doi/10.1103/PhysRevC.66.044310.

[7] Bruce R. Barrett, Petr Navrátil, and James P. Vary. Ab initio no core shell model. *Progress in Particle and Nuclear Physics*, 69:131–181, 2013. URL: https://www.sciencedirect.com/science/article/pii/S0146641012001184.

[8] E. Caurier, P. Navrátil, W. E. Ormand, and J. P. Vary. Ab initio shell model for $A = 10$ nuclei. *Phys. Rev. C*, 66:024314, Aug 2002. URL: https://link.aps.org/doi/10.1103/PhysRevC.66.024314.

[9] Petr Navrátil and W. Erich Ormand. Ab initio shell model with a genuine three-nucleon force for the p-shell nuclei. *Phys. Rev. C*, 68:034305, Sep 2003. URL: https://link.aps.org/doi/10.1103/PhysRevC.68.034305.

[10] W. M. C. Foulkes, L. Mitas, R. J. Needs, and G. Rajagopal. Quantum monte carlo simulations of solids. *Rev. Mod. Phys.*, 73:33–83, Jan 2001. URL: https://link.aps.org/doi/10.1103/RevModPhys.73.33.

[11] Robert Roth, Jeffrey R. Gour, and Piotr Piecuch. Ab initio coupled-cluster and configuration interaction calculations for ^{16}O using the V_{ucom} interaction. *Phys. Rev. C*, 79:054325, May 2009. URL: https://link.aps.org/doi/10.1103/PhysRevC.79.054325.

[12] G. Hagen, T. Papenbrock, A. Ekström, K. A. Wendt, G. Baardsen, S. Gandolfi, M. Hjorth-Jensen, and C. J. Horowitz. Coupled-cluster calculations of nucleonic matter. *Phys. Rev. C*, 89:014319, Jan 2014. URL: https://link.aps.org/doi/10.1103/PhysRevC.89.014319.

[13] D.M. Brink and E. Boeker. Effective interactions for Hartree-Fock calculations. *Nuclear Physics A*, 91(1):1–26, 1967. URL: https://www.sciencedirect.com/science/article/pii/0375947467904460.

[14] Alexandre Obertelli and Hiroyuki Sagawa. *Modern nuclear physics : from fundamentals to frontiers*. UNITEXT for Physics. Springer, Singapore, 2021.

[15] H.-W. Hammer, Sebastian König, and U. van Kolck. Nuclear effective field theory: Status and perspectives. *Rev. Mod. Phys.*, 92:025004, Jun 2020. URL: https://link.aps.org/doi/10.1103/RevModPhys.92.025004.

[16] N. Ishii, S. Aoki, and T. Hatsuda. Nuclear Force from Lattice QCD. *Phys. Rev. Lett.*, 99:022001, Jul 2007. URL: https://link.aps.org/doi/10.1103/PhysRevLett.99.022001.

[17] W. Heisenberg. Über den bau der atomkerne. i. *Zeitschrift für Physik*, 77:1, 1932. URL: https://doi.org/10.1007/BF01342433.

[18] J. Henderson and S. R. Stroberg. Examination of the inversion of isobaric analogue states in mirror nuclei. *Phys. Rev. C*, 102:031303(R), Sep 2020. URL: https://link.aps.org/doi/10.1103/PhysRevC.102.031303.

[19] K. Wimmer, W. Korten, P. Doornenbal, T. Arici, P. Aguilera, A. Algora, T. Ando, H. Baba, B. Blank, A. Boso, S. Chen, A. Corsi, P. Davies, G. de Angelis, G. de France, J.-P. Delaroche, D. T. Doherty, J. Gerl, R. Gernhäuser, M. Girod, D. Jenkins, S. Koyama, T. Motobayashi, S. Nagamine, M. Niikura, A. Obertelli, J. Libert, D. Lubos, T. R. Rodríguez, B. Rubio, E. Sahin, T. Y. Saito, H. Sakurai, L. Sinclair, D. Steppenbeck, R. Taniuchi, R. Wadsworth, and M. Zielinska. Shape changes in the mirror nuclei ^{70}Kr and ^{70}Se. *Phys. Rev. Lett.*, 126:072501, Feb 2021. URL: https://link.aps.org/doi/10.1103/PhysRevLett.126.072501.

[20] A. Boso, S.A. Milne, M.A. Bentley, F. Recchia, S.M. Lenzi, D. Rudolph, M. Labiche, X. Pereira-Lopez, S. Afara, F. Ameil, T. Arici, S. Aydin, M. Axiotis, D. Barrientos, G. Benzoni, B. Birkenbach, A.J. Boston, H.C. Boston, P. Boutachkov, A. Bracco, A.M. Bruce, B. Bruyneel, B. Cederwall, E. Clement, M.L. Cortes, D.M. Cullen, P. Désesquelles, Zs. Dombràdi, C. Domingo-Pardo, J. Eberth, C. Fahlander, M. Gelain, V. González, P.R. John, J. Gerl, P. Golubev, M. Górska, A. Gottardo, T. Grahn, L. Grassi, T. Habermann, L.J. Harkness-Brennan, T.W. Henry, H. Hess, I. Kojouharov, W. Korten, N. Lalović, M. Lettmann, C. Lizarazo, C. Louchart-Henning, R. Menegazzo, D. Mengoni, E. Merchan, C. Michelagnoli, B. Million, V. Modamio, T. Moeller, D.R. Napoli, J. Nyberg, B.S. Nara Singh, H. Pai, N. Pietralla, S. Pietri, Zs. Podolyak, R.M. Perez Vidal, A. Pullia, D. Ralet, G. Rainovski, M. Reese, P. Reiter, M.D. Salsac, E. Sanchis, L.G. Sarmiento, H. Schaffner, L.M. Scruton, P.P. Singh, C. Stahl, S. Uthayakumaar, J.J. Valiente-Dobón, and O. Wieland. Isospin dependence of electromagnetic transition strengths among an isobaric triplet. *Physics Letters B*, 797:134835, 2019. URL: https://www.sciencedirect.com/science/article/pii/S0370269319305490.

[21] J. P. Delaroche, M. Girod, J. Libert, H. Goutte, S. Hilaire, S. Péru, N. Pillet, and G. F. Bertsch. Structure of even-even nuclei using a mapped collective Hamiltonian and the D1S

Gogny interaction. *Phys. Rev. C*, 81:014303, Jan 2010. URL: https://link.aps.org/doi/10.1103/PhysRevC.81.014303.

[22] Kris Heyde and John L. Wood. Shape coexistence in atomic nuclei. *Rev. Mod. Phys.*, 83:1467–1521, Nov 2011. URL: https://link.aps.org/doi/10.1103/RevModPhys.83.1467.

[23] A Gade and S N Liddick. Shape coexistence in neutron-rich nuclei. *Journal of Physics G: Nuclear and Particle Physics*, 43(2):024001, jan 2016. URL: https://dx.doi.org/10.1088/0954-3899/43/2/024001.

[24] B.V Pritychenko, T Glasmacher, P.D Cottle, M Fauerbach, R.W Ibbotson, K.W Kemper, V Maddalena, A Navin, R Ronningen, A Sakharuk, H Scheit, and V.G Zelevinsky. Role of intruder configurations in 26,28Ne and 30,32Mg. *Physics Letters B*, 461(4):322–328, 1999. URL: https://www.sciencedirect.com/science/article/pii/S0370269399008503.

[25] O. Sorlin and M.-G. Porquet. Nuclear magic numbers: New features far from stability. *Progress in Particle and Nuclear Physics*, 61(2):602–673, 2008. URL: https://www.sciencedirect.com/science/article/pii/S0146641008000380.

[26] Takaharu Otsuka, Alexandra Gade, Olivier Sorlin, Toshio Suzuki, and Yutaka Utsuno. Evolution of shell structure in exotic nuclei. *Rev. Mod. Phys.*, 92:015002, Mar 2020. URL: https://link.aps.org/doi/10.1103/RevModPhys.92.015002.

[27] E. K. Warburton, J. A. Becker, and B. A. Brown. Mass systematics for A=29-44 nuclei: The deformed A∼32 region. *Phys. Rev. C*, 41:1147–1166, Mar 1990. URL: https://link.aps.org/doi/10.1103/PhysRevC.41.1147.

[28] G. Saxena and D. Singh. Study of neutron magic drip-line nuclei within relativistic mean-field plus BCS approach. *International Journal of Modern Physics E*, 22(05):1350025, 2013. URL: https://doi.org/10.1142/S0218301313500250.

[29] Maria G. Mayer. On closed shells in nuclei. *Phys. Rev.*, 74:235–239, Aug 1948. URL: https://link.aps.org/doi/10.1103/PhysRev.74.235.

[30] Maria Goeppert Mayer. On closed shells in nuclei. ii. *Phys. Rev.*, 75:1969–1970, Jun 1949. URL: https://link.aps.org/doi/10.1103/PhysRev.75.1969.

[31] Otto Haxel, J. Hans D. Jensen, and Hans E. Suess. On the "magic numbers" in nuclear structure. *Phys. Rev.*, 75:1766–1766, Jun 1949. URL: https://link.aps.org/doi/10.1103/PhysRev.75.1766.2.

[32] The nobel prize in physics 1963. https://www.nobelprize.org/prizes/physics/1963/summary/. Accessed: 2024-09-07.

[33] Brookhaven National Laboratory. National Nuclear Data Center. https://www.nndc.bnl.gov/. Accessed: 2024-07-07.

[34] A. Poves and J. Retamosa. The onset of deformation at the N = 20 neutron shell closure far from stability. *Physics Letters B*, 184(4):311–315, 1987. URL: https://www.sciencedirect.com/science/article/pii/0370269387901717.

[35] R. Elder, H. Iwasaki, J. Ash, D. Bazin, P. C. Bender, T. Braunroth, C. M. Campbell, H. L. Crawford, B. Elman, A. Gade, M. Grinder, N. Kobayashi, B. Longfellow, T. Mijatović, J. Pereira, A. Revel, D. Rhodes, and D. Weisshaar. Lifetime measurements probing collectivity in the ground-state band of ^{32}Mg. *Phys. Rev. C*, 104:024307, Aug 2021. URL: https://link.aps.org/doi/10.1103/PhysRevC.104.024307.

[36] A. Ozawa, T. Kobayashi, T. Suzuki, K. Yoshida, and I. Tanihata. New magic number, $N = 16$, near the neutron drip line. *Phys. Rev. Lett.*, 84:5493–5495, Jun 2000. URL: https://link.aps.org/doi/10.1103/PhysRevLett.84.5493.

[37] B. A. Brown. Lecture notes on nuclear structure, 2021.

[38] B. Alex Brown and W. A. Richter. New "USD" Hamiltonians for the *sd* shell. *Phys. Rev. C*, 74:034315, Sep 2006. URL: https://link.aps.org/doi/10.1103/PhysRevC.74.034315.

[39] W. A. Richter, S. Mkhize, and B. Alex Brown. *sd*-shell observables for the usda and usdb hamiltonians. *Phys. Rev. C*, 78:064302, Dec 2008. URL: https://link.aps.org/doi/10.1103/PhysRevC.78.064302.

[40] Aron M. Bernstein, V. R. Brown, and V. A. Madsen. Isospin decomposition of nuclear multipole matrix elements from γ decay rates of mirror transitions: Test of values obtained with hadronic probes. *Phys. Rev. Lett.*, 42:425–428, Feb 1979. URL: https://link.aps.org/doi/10.1103/PhysRevLett.42.425.

[41] M. Honma, T. Otsuka, B. A. Brown, and T. Mizusaki. New effective interaction for pf-shell nuclei and its implications for the stability of the N = Z = 28 closed core. *Phys. Rev. C*, 69:034335, Mar 2004. URL: https://link.aps.org/doi/10.1103/PhysRevC.69.034335.

[42] W. A. Richter, S. Mkhize, and B. Alex Brown. *sd*-shell observables for the USDA and USDB Hamiltonians. *Phys. Rev. C*, 78:064302, Dec 2008. URL: https://link.aps.org/doi/10.1103/PhysRevC.78.064302.

[43] P. D. Cottle, M. Fauerbach, T. Glasmacher, R. W. Ibbotson, K. W. Kemper, B. Pritychenko, H. Scheit, and M. Steiner. The $0^+_{\text{g.s.}} \rightarrow 2^+_1$ transition in ^{38}Ca and isospin symmetry in A = 38 nuclei. *Phys. Rev. C*, 60:031301(R), Aug 1999. URL: https://link.aps.org/doi/10.1103/PhysRevC.60.031301.

[44] F. M. Prados Estévez, A. M. Bruce, M. J. Taylor, H. Amro, C. W. Beausang, R. F. Casten, J. J. Ressler, C. J. Barton, C. Chandler, and G. Hammond. Isospin purity of T=1 states in the A = 38 nuclei studied via lifetime measurements in ^{38}K. *Phys. Rev. C*, 75:014309, Jan 2007. URL: https://link.aps.org/doi/10.1103/PhysRevC.75.014309.

[45] Jun Chen. Nuclear data sheets for A=39. *Nuclear Data Sheets*, 149:1–251, 2018. URL: https://www.sciencedirect.com/science/article/pii/S0090375218300437.

[46] A.M. Bernstein, V.R. Brown, and V.A. Madsen. Neutron and proton transition matrix elements and inelastic hadron scattering. *Physics Letters B*, 103(4):255–258, 1981. URL: https://www.sciencedirect.com/science/article/pii/0370269381902197.

[47] A. M. Bernstein, V. R. Brown, and V. A. Madsen. Neutron and Proton Matrix Elements for Low-Lying 2^+ Transitions and the Probe Dependence of the Nuclear Deformation Parameter. *Comments Nucl. Part. Phys.*, 11(5):203–215, 1983.

[48] J. J. Valiente-Dobón, A. Poves, A. Gadea, and B. Fernández-Domínguez. Broken mirror symmetry in ^{36}S and ^{36}Ca. *Phys. Rev. C*, 98:011302, Jul 2018. URL: https://link.aps.org/doi/10.1103/PhysRevC.98.011302.

[49] N. Dronchi, D. Weisshaar, B. A. Brown, A. Gade, R. J. Charity, L. G. Sobotka, K. W. Brown, W. Reviol, D. Bazin, P. J. Farris, A. M. Hill, J. Li, B. Longfellow, D. Rhodes, S. N. Paneru, S. A. Gillespie, A. Anthony, E. Rubino, and S. Biswas. Measurement of the B(E2 ↑) strengths of ^{36}Ca and ^{38}Ca. *Phys. Rev. C*, 107:034306, Mar 2023. URL: https://link.aps.org/doi/10.1103/PhysRevC.107.034306.

[50] T. Beck, A. Gade, B. A. Brown, J. A. Tostevin, D. Weisshaar, D. Bazin, K. W. Brown, R. J. Charity, P. J. Farris, S. A. Gillespie, A. M. Hill, J. Li, B. Longfellow, W. Reviol, and D. Rhodes. Probing proton cross-shell excitations through the two-neutron removal from ^{38}Ca. *Phys. Rev. C*, 108:L061301, Dec 2023. URL: https://link.aps.org/doi/10.1103/PhysRevC.108.L061301.

[51] C. Morse, H. Iwasaki, A. Lemasson, A. Dewald, T. Braunroth, V.M. Bader, T. Baugher, D. Bazin, J.S. Berryman, C.M. Campbell, A. Gade, C. Langer, I.Y. Lee, C. Loelius, E. Lunderberg, F. Recchia, D. Smalley, S.R. Stroberg, R. Wadsworth, C. Walz, D. Weisshaar, A. Westerberg, K. Whitmore, and K. Wimmer. Lifetime measurement of the 2_1^+ state in ^{74}Rb and isospin properties of quadrupole transition strengths at N = Z. *Physics Letters B*, 787:198–203, 2018. URL: https://www.sciencedirect.com/science/article/pii/S037026931830844X.

[52] A.O. Macchiavelli, P. Fallon, R.M. Clark, M. Cromaz, M.A. Deleplanque, R.M. Diamond, G.J. Lane, I.Y. Lee, F.S. Stephens, C.E. Svensson, K. Vetter, and D. Ward. Collective T=0 pairing in N=Z nuclei? Pairing vibrations around 56Ni revisited. *Physics Letters B*, 480(1):1–6, 2000. URL: https://www.sciencedirect.com/science/article/pii/S0370269300003816.

[53] W. Kessel, R. Bass, E.C. Hagen, N.R. Roberson, C.R. Gould, and D.R. Tilley. Study of excited states of ^{39}Ca and ^{39}K. *Nuclear Physics A*, 223(2):253–267, 1974. URL: https://www.sciencedirect.com/science/article/pii/0375947474904138.

[54] P.A. Zavodszky, B. Arend, D. Cole, J. DeKamp, G. Machicoane, F. Marti, P. Miller, J. Moskalik, J. Ottarson, J. Vincent, and A. Zeller. Design of SuSI – superconducting source for ions at NSCL/MSU – II. The conventional parts. *Nuclear Instruments and Methods in Physics Research Section B: Beam Interactions with Materials and Atoms*, 241(1):959–964, 2005. The Application of Accelerators in Research and Industry. URL: https://www.sciencedirect.com/science/article/pii/S0168583X05013601.

[55] R. C. York, H. G. Blosser, T. L. Grimm, F. Marti, J. Vincent, X. Y. Wu, and A. Zeller. The NSCL Coupled Cyclotron Project - Overview and Status. In *15th International Conference on Cyclotrons and Their Applications*, page K01, 9 1999.

[56] D.J. Morrissey, B.M. Sherrill, M. Steiner, A. Stolz, and I. Wiedenhoever. Commissioning the A1900 projectile fragment separator. *Nuclear Instruments and Methods in Physics Research Section B: Beam Interactions with Materials and Atoms*, 204:90–96, 2003. 14th International Conference on Electromagnetic Isotope Separators and Techniques Related to their Applications. URL: https://www.sciencedirect.com/science/article/pii/S0168583X02018955.

[57] H. Iwasaki, A. Dewald, T. Braunroth, C. Fransen, D. Smalley, A. Lemasson, C. Morse, K. Whitmore, and C. Loelius. The TRIple PLunger for EXotic beams TRIPLEX for excited-state lifetime measurement studies on rare isotopes. *Nuclear Instruments and Methods in Physics Research Section A: Accelerators, Spectrometers, Detectors and Associated Equipment*, 806:123–131, 2016. URL: https://www.sciencedirect.com/science/article/pii/S0168900215011626.

[58] S. Paschalis, I.Y. Lee, A.O. Macchiavelli, C.M. Campbell, M. Cromaz, S. Gros, J. Pavan, J. Qian, R.M. Clark, H.L. Crawford, D. Doering, P. Fallon, C. Lionberger, T. Loew, M. Petri, T. Stezelberger, S. Zimmermann, D.C. Radford, K. Lagergren, D. Weisshaar, R. Winkler, T. Glasmacher, J.T. Anderson, and C.W. Beausang. The performance of the gamma-ray energy tracking in-beam nuclear array GRETINA. *Nuclear Instruments and Methods in Physics Research Section A: Accelerators, Spectrometers, Detectors and Associated Equipment*, 709:44–55, 2013. URL: https://www.sciencedirect.com/science/article/pii/S0168900213000508.

[59] D. Weisshaar, D. Bazin, P.C. Bender, C.M. Campbell, F. Recchia, V. Bader, T. Baugher, J. Belarge, M.P. Carpenter, H.L. Crawford, M. Cromaz, B. Elman, P. Fallon, A. Forney, A. Gade, J. Harker, N. Kobayashi, C. Langer, T. Lauritsen, I.Y. Lee, A. Lemasson, B. Longfellow, E. Lunderberg, A.O. Macchiavelli, K. Miki, S. Momiyama, S. Noji, D.C. Radford, M. Scott, J. Sethi, S.R. Stroberg, C. Sullivan, R. Titus, A. Wiens, S. Williams, K. Wimmer, and S. Zhu. The performance of the γ-ray tracking array GRETINA for γ-ray spectroscopy with fast beams of rare isotopes. *Nuclear Instruments and Methods in Physics Research Section A: Accelerators, Spectrometers, Detectors and Associated Equipment*, 847:187–198, 2017. URL: https://www.sciencedirect.com/science/article/pii/S0168900216312402.

[60] D. Bazin, J.A. Caggiano, B.M. Sherrill, J. Yurkon, and A. Zeller. The S800 spectrograph. *Nuclear Instruments and Methods in Physics Research Section B: Beam Interactions with Materials and Atoms*, 204:629–633, 2003. 14th International Conference on Electromagnetic Isotope Separators and Techniques Related to their Applications. URL: https://www.sciencedirect.com/science/article/pii/S0168583X02021420.

[61] Virtual tour. https://nscl.msu.edu/public/virtual-tour.html. Accessed: 2024-09-16.

[62] Superconducting source for ions. https://www.flickr.com/photos/nsclmedia/2511375941/in/photostream/. Accessed: 2024-06-05.

[63] B.-M. Sherrill. Scientific Opportunities with the NSCL Coupled Cyclotron Facility. *Progress of Theoretical Physics Supplement*, 146:60–69, 03 2002. URL: https://doi.org/10.1143/PTPS.146.60.

[64] D.J. Morrissey. The coupled cyclotron project at the NSCL. *Nuclear Physics A*, 616(1):45–55, 1997. Radioactive Nuclear Beams. URL: https://www.sciencedirect.com/science/article/pii/S0375947497000730.

[65] S. M. Austin. The Michigan State University Cyclotron Laboratory: Its Early Years. *Physics in Perspective*, 17(4):298–333, 2016. URL: https://www.sciencedirect.com/science/article/pii/S0168583X05013601.

[66] Planning for a STANDARD in-Flight RNB Experiment. https://groups.frib.msu.edu/a1900/experimentplanning/a1900_flowCa.pdf. Accessed: 2024-09-22.

[67] Glenn F Knoll. *Radiation detection and measurement; 4th ed.* Wiley, New York, NY, 2010. URL: https://cds.cern.ch/record/1300754.

[68] William R Leo. *Techniques for nuclear and particle physics experiments: a how-to approach; 2nd ed.* Springer, Berlin, 1994. URL: https://cds.cern.ch/record/302344.

[69] J.P. Dufour, R. Del Moral, H. Emmermann, F. Hubert, D. Jean, C. Poinot, M.S. Pravikoff, A. Fleury, H. Delagrange, and K.-H. Schmidt. Projectile fragments isotopic separation: Application to the lise spectrometer at GANIL. *Nuclear Instruments and Methods in Physics Research Section A: Accelerators, Spectrometers, Detectors and Associated Equipment*, 248(2):267–281, 1986. URL: https://www.sciencedirect.com/science/article/pii/0168900286910089.

[70] J. Pereira. S800 spectrograph detector stations. https://wikihost.nscl.msu.edu/S800Doc/doku.php?id=stations. Accessed: 2024-06-14.

[71] J.A. Swartz. S800 focal plane detectors. https://wikihost.nscl.msu.edu/S800Doc/doku.php?id=detectors. Accessed: 2024-06-14.

[72] NSCLDAQ documentation. https://docs.frib.msu.edu/daq/newsite/index.php. Accessed: 2024-09-22.

[73] D. M. Cullen. DPUNS—A Differential Plunger For Lifetime Measurements Of Tagged Exotic/Unbound Nuclear States. *AIP Conference Proceedings*, 1377(1):316–320, 10 2011. URL: https://pubs.aip.org/aip/acp/article-pdf/1377/1/316/11670876/316_1_online.pdf.

[74] P. Voss, R. Henderson, C. Andreoiu, R. Ashley, R.A.E. Austin, G.C. Ball, P.C. Bender, A. Bey, A. Cheeseman, A. Chester, D.S. Cross, T.E. Drake, A.B. Garnsworthy, G. Hackman, R. Holland, S. Ketelhut, P. Kowalski, R. Krücken, A.T. Laffoley, K.G. Leach, D. Miller, W.J. Mills, M. Moukaddam, C.J. Pearson, J. Pore, E.T. Rand, M.M. Rajabali, U. Rizwan, J. Shoults, K. Starosta, C.E. Svensson, E. Tardiff, C. Unsworth, K. Van Wieren, Z.-M. Wang, and J. Williams. The TIGRESS Integrated Plunger ancillary systems for electromagnetic transition rate studies at TRIUMF. *Nuclear Instruments and Methods in Physics Research Section A: Accelerators, Spectrometers, Detectors and Associated Equipment*, 746:87–97, 2014. URL: https://www.sciencedirect.com/science/article/pii/S0168900214001429.

[75] R.E. Laxdal. Acceleration of radioactive ions. *Nuclear Instruments and Methods in Physics Research Section B: Beam Interactions with Materials and Atoms*, 204:400–409, 2003. 14th International Conference on Electromagnetic Isotope Separators and Techniques Related to their Applications. URL: https://www.sciencedirect.com/science/article/pii/S0168583X02021043.

[76] M.M. Giles, D.M. Cullen, L. Barber, B.S. Nara Singh, M.J. Taylor, A.J. Smith, A. McFarlane, C. Read, T. Grahn, H. Badran, P.T. Greenlees, R. Julin, J. Pakarinen, J. Partanen, P. Rahkila, P. Ruotsalainen, M. Sandzelius, J. Sarén, J. Sorri, S.V. Szwec, J. Uusitalo, J. Heery, E. Parr, P. Papadakis, and R.D. Herzberg. TPEN: A Triple-foil differential Plunger for lifetime measurements of excited states in Exotic Nuclei. *Nuclear Instruments and Methods in Physics Research Section A: Accelerators, Spectrometers, Detectors and Associated Equipment*, 923:139–146, 2019. URL: https://www.sciencedirect.com/science/article/pii/S0168900219301597.

[77] L. Barber, J. Heery, D.M. Cullen, B.S. Nara Singh, R.-D. Herzberg, C. Müller-Gatermann, G. Beeton, M. Bowry, A. Dewald, T. Grahn, P.T. Greenlees, A. Illana, R. Julin, S. Juutinen, J.M. Keatings, M. Luoma, D. O'Donnell, J. Ojala, J. Pakarinen, P. Rahkila, P. Ruotsalainen, M. Sandzelius, J. Sarén, J. Sinclair, J.F. Smith, J. Sorri, P. Spagnoletti, H. Tann, J. Uusitalo, J. Vilhena, and G. Zimba. A charge plunger device to measure the lifetimes of excited nuclear states where transitions are dominated by internal conversion. *Nuclear Instruments and Methods in Physics Research Section A: Accelerators, Spectrometers, Detectors and Associated Equipment*, 979:164454, 2020. URL: https://www.sciencedirect.com/science/article/pii/S0168900220308512.

[78] Jan Sarén, Juha Uusitalo, and Henna Joukainen. In-flight recoil separators RITU and MARA and the standard detector setups. *Nuclear Instruments and Methods in Physics Research Section B: Beam Interactions with Materials and Atoms*, 541:33–36, 2023. URL: https://www.sciencedirect.com/science/article/pii/S0168583X23001787.

[79] M. Beckers, A. Dewald, C. Fransen, K. Arnswald, C. Müller-Gatermann, and F. von Spee. Development of the multi-purpose Cologne Compact Differential Plunger (CoCoDiff) for the measurement of nuclear level lifetimes with the Recoil Distance Doppler-shift method. *Nuclear Instruments and Methods in Physics Research Section A: Accelerators, Spectrometers, Detectors and Associated Equipment*, 1042:167418, 2022. URL: https://www.sciencedirect.com/science/article/pii/S0168900222007100.

[80] W.F. Mueller, J.A. Church, T. Glasmacher, D. Gutknecht, G. Hackman, P.G. Hansen, Z. Hu, K.L. Miller, and P. Quirin. Thirty-two-fold segmented germanium detectors to identify γ-rays from intermediate-energy exotic beams. *Nuclear Instruments and Methods in Physics Research Section A: Accelerators, Spectrometers, Detectors and Associated Equipment*, 466(3):492–498, 2001. URL: https://www.sciencedirect.com/science/article/pii/S0168900201002571.

[81] TESA Technology. https://tesatechnology.com/en-us/home/. Accessed: 2024-09-22.

[82] A. Dewald, S. Harissopulos, and P. von Brentano. The differential plunger and the differential decay curve method for the analysis of recoil distance doppler-shift data. *Zeitschrift für*

Physik A Atomic Nuclei, 334:163–175, 1989. URL: https://link.springer.com/article/10.1007/BF01294217.

[83] P. Adrich, D. Enderich, D. Miller, V. Moeller, R.P. Norris, K. Starosta, C. Vaman, P. Voss, and A. Dewald. A simulation tool for recoil distance method lifetime measurements at NSCL. *Nuclear Instruments and Methods in Physics Research Section A: Accelerators, Spectrometers, Detectors and Associated Equipment*, 598(2):454–464, 2009. URL: https://www.sciencedirect.com/science/article/pii/S0168900208014708.

[84] S. Agostinelli, J. Allison, K. Amako, J. Apostolakis, H. Araujo, P. Arce, M. Asai, D. Axen, S. Banerjee, G. Barrand, F. Behner, L. Bellagamba, J. Boudreau, L. Broglia, A. Brunengo, H. Burkhardt, S. Chauvie, J. Chuma, R. Chytracek, G. Cooperman, G. Cosmo, P. Degtyarenko, A. Dell'Acqua, G. Depaola, D. Dietrich, R. Enami, A. Feliciello, C. Ferguson, H. Fesefeldt, G. Folger, F. Foppiano, A. Forti, S. Garelli, S. Giani, R. Giannitrapani, D. Gibin, J.J. Gómez Cadenas, I. González, G. Gracia Abril, G. Greeniaus, W. Greiner, V. Grichine, A. Grossheim, S. Guatelli, P. Gumplinger, R. Hamatsu, K. Hashimoto, H. Hasui, A. Heikkinen, A. Howard, V. Ivanchenko, A. Johnson, F.W. Jones, J. Kallenbach, N. Kanaya, M. Kawabata, Y. Kawabata, M. Kawaguti, S. Kelner, P. Kent, A. Kimura, T. Kodama, R. Kokoulin, M. Kossov, H. Kurashige, E. Lamanna, T. Lampén, V. Lara, V. Lefebure, F. Lei, M. Liendl, W. Lockman, F. Longo, S. Magni, M. Maire, E. Medernach, K. Minamimoto, P. Mora de Freitas, Y. Morita, K. Murakami, M. Nagamatu, R. Nartallo, P. Nieminen, T. Nishimura, K. Ohtsubo, M. Okamura, S. O'Neale, Y. Oohata, K. Paech, J. Perl, A. Pfeiffer, M.G. Pia, F. Ranjard, A. Rybin, S. Sadilov, E. Di Salvo, G. Santin, T. Sasaki, N. Savvas, Y. Sawada, S. Scherer, S. Sei, V. Sirotenko, D. Smith, N. Starkov, H. Stoecker, J. Sulkimo, M. Takahata, S. Tanaka, E. Tcherniaev, E. Safai Tehrani, M. Tropeano, P. Truscott, H. Uno, L. Urban, P. Urban, M. Verderi, A. Walkden, W. Wander, H. Weber, J.P. Wellisch, T. Wenaus, D.C. Williams, D. Wright, T. Yamada, H. Yoshida, and D. Zschiesche. Geant4—a simulation toolkit. *Nuclear Instruments and Methods in Physics Research Section A: Accelerators, Spectrometers, Detectors and Associated Equipment*, 506(3):250–303, 2003. URL: https://www.sciencedirect.com/science/article/pii/S0168900203013688.

[85] R. Fox. SpecTcl home page. http://docs.nscl.msu.edu/daq/spectcl/, 2003. Accessed: 2024-06-27.

[86] Lawrence Berkeley National Laboratory. GRETINA Tools. https://greta.lbl.gov/tools-etc. Accessed: 2024-08-25.

[87] Rene Brun, Fons Rademakers, Philippe Canal, Axel Naumann, Olivier Couet, Lorenzo Moneta, Vassil Vassilev, Sergey Linev, Danilo Piparo, Gerardo GANIS, Bertrand Bellenot, Enrico Guiraud, Guilherme Amadio, wverkerke, Pere Mato, TimurP, Matevž Tadel, wlav, Enric Tejedor, Jakob Blomer, Andrei Gheata, Stephan Hageboeck, Stefan Roiser, marsupial, Stefan Wunsch, Oksana Shadura, Anirudha Bose, Cristina Cristescu, Xavier Valls, and Raphael Isemann. root-project/root: v6.18/02, jun 2020. URL: https://doi.org/10.5281/zenodo.3895860.

[88] A. Sanchez, H. Iwasaki, A. Revel, B. A. Brown, J. Ash, D. Bazin, J. Chen, R. Elder, A. Gade, A. Goldkuhle, M. Grinder, D. Lempke, J. Li, B. Longfellow, C. Müller-Gatermann, J. Pereira,

D. Rhodes, R. Salinas, and D. Weisshaar. Proton and neutron contributions to the quadrupole transition strengths in ^{39}Ca and ^{39}K studied by lifetime measurements of mirror transitions. *Phys. Rev. C*, 110:024322, Aug 2024. URL: https://link.aps.org/doi/10.1103/PhysRevC.110.024322.

[89] C. Loelius, H. Iwasaki, B. A. Brown, M. Honma, V. M. Bader, T. Baugher, D. Bazin, J. S. Berryman, T. Braunroth, C. M. Campbell, A. Dewald, A. Gade, N. Kobayashi, C. Langer, I. Y. Lee, A. Lemasson, E. Lunderberg, C. Morse, F. Recchia, D. Smalley, S. R. Stroberg, R. Wadsworth, C. Walz, D. Weisshaar, A. Westerberg, K. Whitmore, and K. Wimmer. Lifetime measurement of the 4_1^+ state of ^{58}Ni with the recoil distance method. *Phys. Rev. C*, 94:024340, Aug 2016. URL: https://link.aps.org/doi/10.1103/PhysRevC.94.024340.

[90] H. Iwasaki, A. Lemasson, C. Morse, A. Dewald, T. Braunroth, V. M. Bader, T. Baugher, D. Bazin, J. S. Berryman, C. M. Campbell, A. Gade, C. Langer, I. Y. Lee, C. Loelius, E. Lunderberg, F. Recchia, D. Smalley, S. R. Stroberg, R. Wadsworth, C. Walz, D. Weisshaar, A. Westerberg, K. Whitmore, and K. Wimmer. Evolution of collectivity in ^{72}Kr: Evidence for rapid shape transition. *Phys. Rev. Lett.*, 112:142502, Apr 2014. URL: https://link.aps.org/doi/10.1103/PhysRevLett.112.142502.

[91] C. Loelius, N. Kobayashi, H. Iwasaki, D. Bazin, J. Belarge, P. C. Bender, B. A. Brown, R. Elder, B. Elman, A. Gade, M. Grinder, S. Heil, A. Hufnagel, B. Longfellow, E. Lunderberg, M. Mathy, T. Otsuka, M. Petri, I. Syndikus, N. Tsunoda, D. Weisshaar, and K. Whitmore. Enhanced electric dipole strength for the weakly bound states in ^{27}Ne. *Phys. Rev. Lett.*, 121:262501, Dec 2018. URL: https://link.aps.org/doi/10.1103/PhysRevLett.121.262501.

[92] A. Gade, D. Weisshaar, B. A. Brown, D. Bazin, K. W. Brown, R. J. Charity, P. Farris, A. M. Hill, J. Li, B. Longfellow, D. Rhodes, W. Reviol, and J. A. Tostevin. Exploiting dissipative reactions to perform in-beam γ-ray spectroscopy of the neutron-deficient isotopes ^{38,39}Ca. *Phys. Rev. C*, 106:064303, Dec 2022. URL: https://link.aps.org/doi/10.1103/PhysRevC.106.064303.

[93] A. Dewald, O. Möller, and P. Petkov. Developing the recoil distance doppler-shift technique towards a versatile tool for lifetime measurements of excited nuclear states. *Progress in Particle and Nuclear Physics*, 67(3):786–839, 2012. URL: https://www.sciencedirect.com/science/article/pii/S0146641012000713.

[94] R. S. Lubna, K. Kravvaris, S. L. Tabor, Vandana Tripathi, E. Rubino, and A. Volya. Evolution of the N = 20 and 28 shell gaps and two-particle-two-hole states in the FSU interaction. *Phys. Rev. Res.*, 2:043342, Dec 2020. URL: https://link.aps.org/doi/10.1103/PhysRevResearch.2.043342.

[95] E Caurier, K Langanke, G Martínez-Pinedo, F Nowacki, and P Vogel. Shell model description of isotope shifts in calcium. *Physics Letters B*, 522(3):240–244, 2001. URL: https://www.sciencedirect.com/science/article/pii/S0370269301012461.

[96] M. L. Bissell, J. Papuga, H. Naïdja, K. Kreim, K. Blaum, M. De Rydt, R. F. Garcia Ruiz, H. Heylen, M. Kowalska, R. Neugart, G. Neyens, W. Nörtershäuser, F. Nowacki, M. M.

Rajabali, R. Sanchez, K. Sieja, and D. T. Yordanov. Proton-neutron pairing correlations in the self-conjugate nucleus ^{38}K probed via a direct measurement of the isomer shift. *Phys. Rev. Lett.*, 113:052502, Jul 2014. URL: https://link.aps.org/doi/10.1103/PhysRevLett.113.052502.

[97] E. K. Warburton and B. A. Brown. Effective interactions for the 0p1s0d nuclear shell-model space. *Phys. Rev. C*, 46:923–944, Sep 1992. URL: https://link.aps.org/doi/10.1103/PhysRevC.46.923.

[98] M. Honma, T. Otsuka, B. A. Brown, and T. Mizusaki. Shell-model description of neutron-rich pf-shell nuclei with a new effective interaction GXPF1. *Eur. Phys. J. A*, 25:499–502, Sep 2005. URL: https://link.springer.com/article/10.1140/epjad/i2005-06-032-2.

[99] J. Retamosa, E. Caurier, F. Nowacki, and A. Poves. Shell model study of the neutron-rich nuclei around $N = 28$. *Phys. Rev. C*, 55:1266–1274, Mar 1997. URL: https://link.aps.org/doi/10.1103/PhysRevC.55.1266.

[100] M. Spieker, A. Gade, D. Weisshaar, B. A. Brown, J. A. Tostevin, B. Longfellow, P. Adrich, D. Bazin, M. A. Bentley, J. R. Brown, C. M. Campbell, C. Aa. Diget, B. Elman, T. Glasmacher, M. Hill, B. Pritychenko, A. Ratkiewicz, and D. Rhodes. One-proton and one-neutron knockout reactions from N = Z = 28 ^{56}Ni to the A = 55 mirror pair ^{55}Co and ^{55}Ni. *Phys. Rev. C*, 99:051304, May 2019. URL: https://link.aps.org/doi/10.1103/PhysRevC.99.051304.